Optical properties of thin film solar cell structures on imprinted microstructures

Master's thesis, Aalborg University, 2013

Patrick Rebsdorf Whelan

Optical properties of thin film solar cell structures on imprinted microstructures

Thesis by
Patrick Rebsdorf Whelan
Aalborg University, Skjernvej 4A, DK-9220 Aalborg Øst

Supervised by
Professor Thomas Garm Pedersen
Aalborg University, Skjernvej 4A, DK-9220 Aalborg Øst

Abstract

Thin film solar cells based on amorphous silicon require efficient light trapping due to the reduced thickness of the cell. Antireflective coatings may reduce the reflectance, but microstructuring the surface has been shown to be more efficient for a broader wavelength range. In this project, structured PMMA substrates were prepared by a micro-imprinting process. Using PMMA in the solar cell design adds strength to a thin film solar cell and provides easy handling. The process presented here is deemed viable for larger scale production.

Five different masters were used for obtaining microstructured PMMA substrates. Four masters were synthesized by anodic anodization of aluminum and the fifth master was prepared by anisotropic etching in crystalline silicon. Indium tin oxide, amorphous silicon and aluminum layers were deposited on the imprinted surfaces in order to imitate a solar cell structure. Reflection and transmission measurements were conducted and the surfaces were examined by AFM and SEM in order to model the surfaces. The surface models were used for simulating the optical properties with *Lumerical FDTD Solutions*.

Based on the reflection measurements, it was shown that the reflection of the AM1.5 solar spectrum could be lowered to 13.1% for imprints with 300 nm a-Si and Al compared to a planar surface with similar layers that reflect 46.7% of the incident solar spectrum. The reflection could be lowered further to ∼9% by adding an antireflective ITO layer.

Printed on June 7th, 2013
Number of pages: 88 (98)

Optiske egenskaber af tyndfilmssolceller på imprintede mikrostrukturer

Speciale af
Patrick Rebsdorf Whelan
Aalborg Universitet, Skjernvej 4A, DK-9220 Aalborg Øst

Vejleder
Professor Thomas Garm Pedersen
Aalborg Universitet, Skjernvej 4A, DK-9220 Aalborg Øst

Synopsis

Effektive metoder til at indfange lys er påkrævet for tyndfilmssolceller baseret på amorft silicium grundet solcellens reducerede tykkelse. Antireflektive coatinger kan reducere reflektionen fra overfladen, men det har vist sig mere effektivt for et større bølgelængdeinterval at mikrostrukturere solcellens overflade. Dette projekt beskriver, hvordan mikrostrukturer kan imprintes i plexiglass. Anvendelsen af plexiglass i designet af en tyndfilmssolcelle tilfører styrke og lettere håndtering. Processen, der præsenteres i dette projekt, vurderes at kunne anvendes til produktion i større skala.

Fem forskellige grundlæggende strukturer var fremstillet til at imprinte i plexiglass. Fire af strukturerne blev fremstillet ved anodisering af aluminum i forskellige syrer, mens den femte struktur blev lavet ved hjælp af anisotropisk ætsning i krystallinsk silicium. Lag af indium-tin-oxid, amorft silicium og aluminium blev tilført de imprintede overfalder for at efterligne en solcelle. Reflektionen og transmissionen fra overfladerne blev målt, og overfladerne blev kortlagt ved AFM og SEM for at kunne modellere overfladerne. Modellerne af overfladerne blev brugt til at simulere de optiske egenskaber ved hjælp af *Lumerical FDTD Solutions*.

Det blev vist ud fra reflektionsmålingerne, at reflektionen af det indfaldende solspektrum kunne reduceres til 13.1% for imprint med 300 nm a-Si og Al i forhold til en reflektion på 46.7% for en flad overflade med de samme lag. Ved at tilføre et lag af antireflektiv coating kunne reflektionen reduceres yderligere til ∼9%.

Printet d. 7. juni, 2013
Antal sider: 88 (98)
Antal appendiks: 5
Sprog: Engelsk

Foreword

The current work is the Master's thesis composed by the author as the final step of completing the Master's degree programme in Nanophysics and -materials at the Department of Physics and Nanotechnology at Aalborg University.
The main focus of the thesis is the *Optical properties of thin film solar cell structures on imprinted microstructures*. The topic follows the authors general focus on and interest in optimization of solar cells, which has included semester projects on *Microstructured solar cell substrates* and *Synthesis, characterization and modeling of silicon solar cells* during the Master's degree programme.

The author would like to thank PhD fellow Eddy Tsao Yao-Chung for providing the anodized masters for the imprinting process. Eddy Tsao Yao-Chung, who is currently working on anodized aluminum solar cell backside reflectors, has also provided helpful inputs during the synthesis of the imprinted substrates. The author would further like to thank research assistant Peter Kjær Kristensen for providing the etched c-Si master and for his great assistance with most of the equipment used in the laboratory.

Aalborg University, June 7th, 2013.

Patrick Rebsdorf Whelan

Contents

Chapter 1

Introduction

The global capacity of installed photovoltaic devices reached 70 GW at the end of 2011[1], which only amounts to 0.43 % of the global energy consumption in that same year[2]. Considering the current interest in the use of renewable energy there is surely a potential for huge growth in the solar cell industry in the years to come. The oil, coal, and gas resources that are currently accounting for more than 87 % of the global energy consumption are not infinite[2]. Adding the air pollution arising from the use of fossil fuels, the motivation for increasing the use of renewable energy sources like sun and wind seems obvious.

The primary production of photovoltaic modules is from wafer-based crystalline silicon technology, which accounts for ∼85 % of the market[1]. These modules have been studied and developed for decades and have achieved efficiencies up to ∼25 % for the UNSW PERL cells[3]. The production of mono-crystalline silicon (c-Si) wafers is however an expensive and quality demanding process and almost half the cost of c-Si solar cells is from the production of silicon wafers[4,5]. The development of efficient thin film solar cells may greatly reduce the production expenses due to less strict requirements for the composition of silicon and the reduced amount of silicon required in a thin film photovoltaic device[1,4,6].

Hydrogenated amorphous silicon (a-Si) is often used for thin film solar cells[4,7,8]. Even though the optical absorption coefficient is generally higher in a-Si compared to c-Si because of the structural disorder, efficient light trapping is still required due to the decreased thickness of the cell and the fact that the penetration depth of especially red and infrared radiation is rather large[7]. The bandgap of a-Si is ∼1.7 eV[7], which means that it will not really absorb light in the infrared part of the spectrum. The incident solar photon flux and the corresponding bandgap of a-Si is shown in Fig. 1.1.

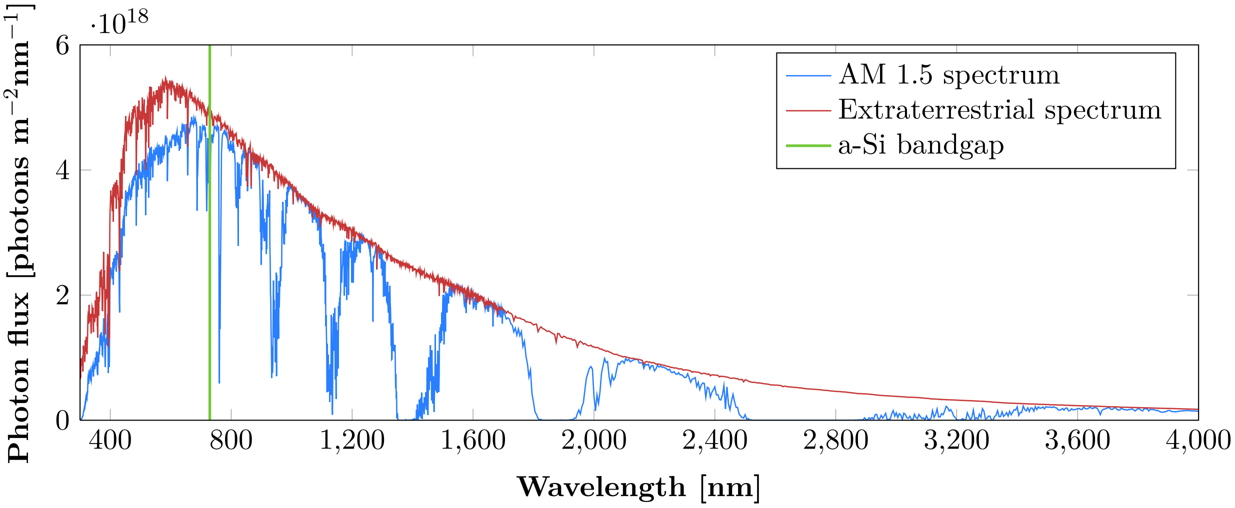

Figure 1.1. The extraterrestrial and AM1.5 solar photon flux[9]. The bandgap of a-Si is also shown.

Light trapping in a solar cell may be carried out in numerous ways. This may for instance be achieved by lowering the reflection by microstructuring/texturing the front surface, by adding plasmonic structures at the back surface to couple incident light into surface plasmon polaritons which force the light to propagate along the back surface, or by increasing the optical path length inside the solar cell by microstructuring the back surface.[5,6,10–14]
Microstructuring the back surface may be done by anodic anodization of aluminum which leads to hexagonally ordered microstructures that can be used as Al back surface reflectors (BSRs) with diffractive and scattering properties that decrease the specular reflection from an Al surface[13,14]. Microstructuring based on imprinting techniques is another way to obtain textured surfaces with anti-reflective properties. Recently, ZnO pyramidal and crater structures have been used for making replicas in borosilicate glass which served as substrates for thin film silicon solar cells[15]. Imprinting of pyramidal structures in thin film solar cells after cell manufacturing to decrease reflection has also been shown[16]. Poly(methyl methacrylate) (PMMA) is a low cost plastic which has shown promising results regarding precise transfer of structures by imprinting[17] and adds strength and deformability to thin film solar cells.

The aim of this project is to imprint Al BSRs prepared by anodic anodization into PMMA in order to transfer the microstructures from the BSRs to the front surface of a solar cell. The anodic anodization of Al was carried out using three different acids, which results in microstructured masters with different periods and indentation depths. The three acids used for anodization were oxalic acid (OA), phosphoric acid (PA), and citric acid (CA). Additional imprints based on an anisotropically etched c-Si master were also prepared.

Thin film solar cell layers, namely indium tin oxide, a-Si, and Al, were deposited on the imprinted substrates. Indium tin oxide (ITO) is a transparent conducting oxide[18,19], which functions as front contact and as an anti-reflective layer with a refractive index ∼2[20], while the Al layer functions as a reflective back contact for the solar cell. The a-Si layer is the absorbing layer. Throughout the report, a-Si will be referred to as Si. Fig. 1.2 shows the structure of the imprints with ITO, a-Si, and Al. The optical properties of the imprinted microstructures were measured by UV/VIS/NIR spectroscopy.

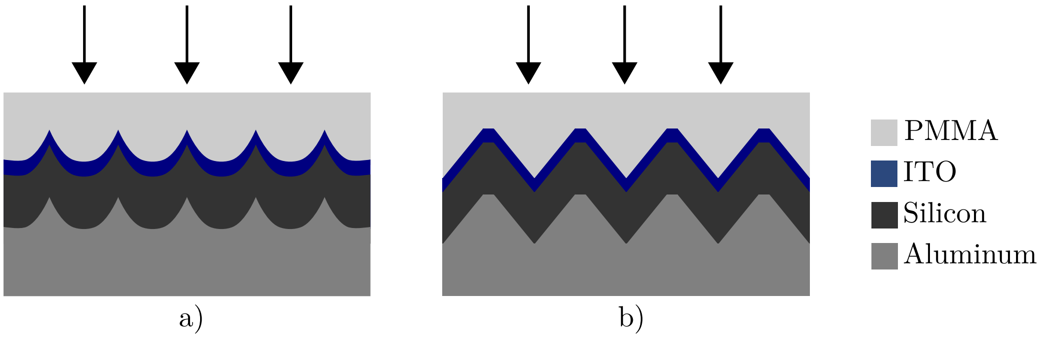

Figure 1.2. Imprints with ITO, a-Si, and Al based on a) anodized masters and, b) etched c-Si master.

The optical properties of the solar cells structures shown in Fig. 1.2 were simulated with *Lumerical FDTD Solutions*. An ideal structure was used for simulations of the imprints based on the etched c-Si master. The topography of some of the imprints based on the anodized master was acquired by AFM measurements and a model describing how the surface changes with varying ITO layers was made. This model was used for running simulations of the imprints based on the anodized masters.

Chapter 2

Experiments

Imprints in PMMA were made with 5 different masters. ITO, Si, and Al layers were deposited on the imprinted substrates. The deposited layers were characterized by ellipsometry, four point probing, and UV/VIS/NIR spectroscopy.

2.1 Synthesis of masters

Two different types of samples were used as masters for producing PMMA molds by imprinting. The first set of masters were synthesized by anodic anodization of Al, while the second set were synthesized by anisotropic etching in c-Si.

2.1.1 Anodic anodization of aluminum

Al BSRs were prepared by PhD fellow Yao-Chung Tsao as described by Tsao et al.[13] Anodic anodization of Al with acidic electrolytes was carried out in order to obtain porous alumina films. Removing the alumina film by selective etching in a mixture of phosphoric and chromic acid[21] leaves a periodically microstructured Al surface as shown in Fig. 2.1c. The microstructure is a hexagonal pattern as shown in Fig. 2.2 with hemispherical indentations.

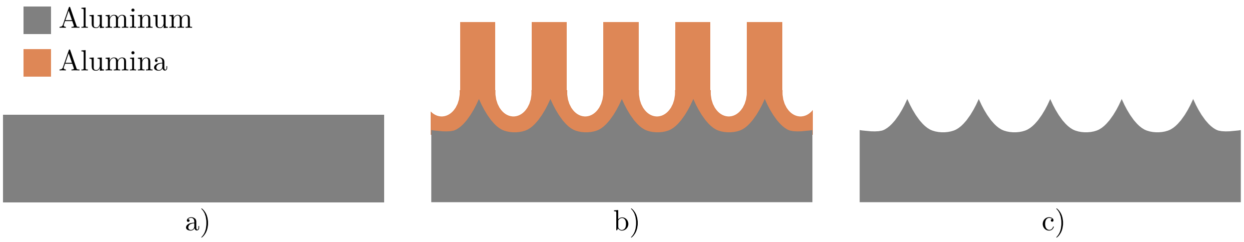

Figure 2.1. Synthesis of BSRs by anodization of Al, where a → b is the anodization step and b → c is the selective etching.

Electrolyte	**Sample name**	**Period**	**Indentation depth**[13]
Oxalic acid	OA	~295 nm	~150 nm
Phosphoric acid	PA	~425 nm	~200 nm
Citric acid	CA1	~600 nm	~350 nm
Citric acid	CA2	~655 nm	~150 nm

Table 2.1. Electrolytes used for anodization with corresponding period and indentation depth.

The period of the microstructures and the depth of the indentations primarily depend on the electrolyte pH and the anodic potential applied during anodization[6,22,23]. The anodized areas were circular with a diameter of 2 cm. Tab. 2.1 shows the period and indentation depth for the different electrolytes used. Samples CA1 and CA2 were prepared using different concentrations of citric acid and with different anodization time and voltages. The anodized samples will be mentioned by the sample names shown in Tab. 2.1 throughout the rest of this report.

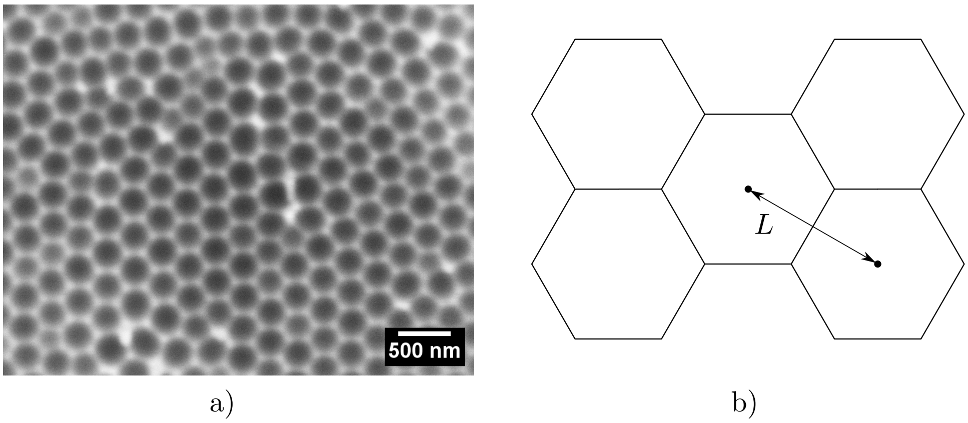

Figure 2.2. a) SEM image of OA master. b) Hexagonal pattern of anodized microstructures with period L.

2.1.2 Anisotropic etching in crystalline silicon

One master was prepared by anisotropic etching in c-Si. The master was prepared by research technician Peter Kjær Kristensen at AAU. Wet etching of a silicon (100) surface in a KOH solution results in V-shaped indentations with a characteristic angle of 54.7° to the surface normal[24]. Chromium was used as an etching mask, where the desired pattern was prepared by e-beam lithography in a PMMA layer, followed by chromium deposition and a lift-off process. The main steps of synthesizing the Si master are shown in Fig. 2.3.

The patterning process carried out by e-beam lithography made a large area pattern by running over areas that were 100 by 100 μm^2 and exposing such areas next to each other. The prepared master was a 2D microstructure that was periodic in one dimension. The period was 700 nm and the lines exposed by the e-beam had a width of 50 nm. A circular area with a diameter of ~1.5 mm was patterned.

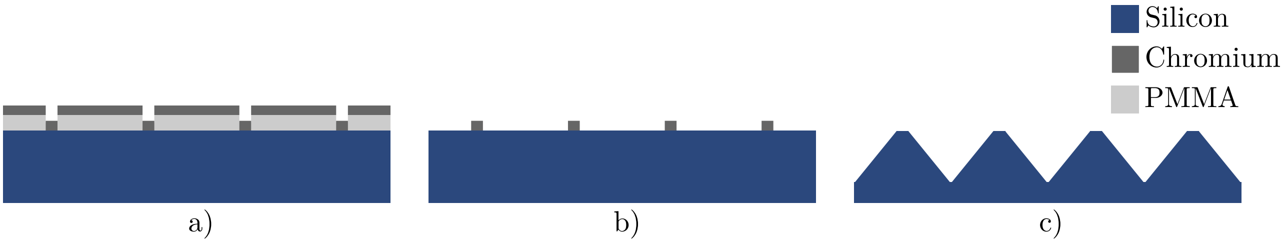

Figure 2.3. Anisotropic etching in c-Si. a) PMMA was patterned by e-beam lithography and chromium was deposited. b) The PMMA was removed and c) Si was etched in a KOH solution and Cr was removed.

2.2 Imprinting

Imprinting of molds was carried out using an EVG520HE semi-automated hot embossing system. Rectangular pieces of PMMA with a thickness of 5 mm were used as molds for the masters. The process was carried out by heating the PMMA and master to 140°C which is above the glass transition temperature of PMMA and then pressing the master ~0.1 mm into the PMMA with an imprinting pressure of 1.25 bar followed by cooling. Figs. 2.4 and 2.5 illustrate the imprinting process with the anodized Al masters and the etched c-Si master, respectively.

The anodized Al masters were glued on to cylindrical pieces of Al with Permabond ES550 epoxy paste in order to avoid bending the anodized masters by easing the separation of master and mold after imprinting.

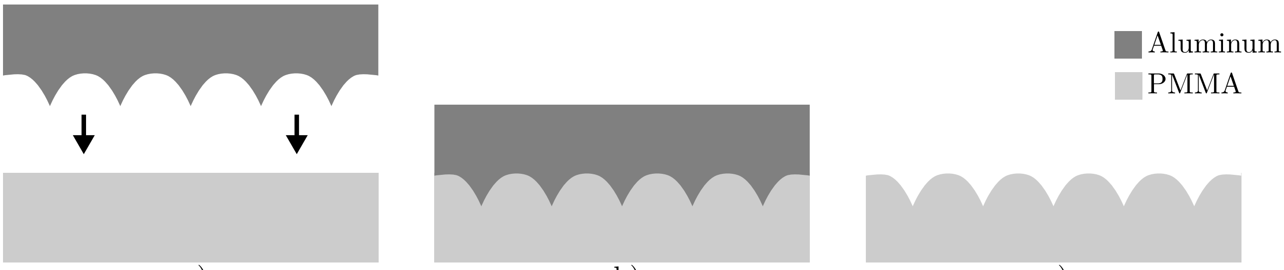

a) b) c)

Figure 2.4. Imprinting with anodized Al master. Steps a and b were carried out at 140°C.

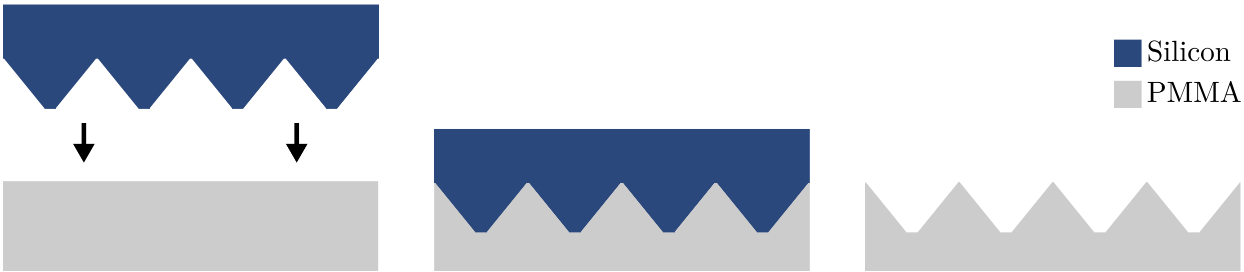

a) b) c)

Figure 2.5. Imprinting with etched c-Si master. Steps a and b are carried out at 140°C.

2.3 Deposition of indium tin oxide

ITO deposition was carried out using a Cryofox Explorer 600 equipped with an RF sputtering system with a 2 inch target consisting of 90 % In_2O_3 and 10 % Sn_2. The depositions were carried out at a sputtering pressure of $4{\cdot}10^{-3}$ mbar with a rate of 0.3 Å/s. The optimization process for obtaining ITO films with low sheet resistance and high transparency is described in App. A.

The thickness of the deposited ITO layer was measured during deposition by a quartz crystal microbalance. The quartz crystal microbalance was calibrated by depositing ITO on a small Si wafer concurrently with the deposition on the PMMA mold and then measuring the thickness by ellipsometry after deposition using a Sentech SE850 ellipsometer. Ellipsometric measurements were also used to determine the refractive index of the ITO layer. Three different models were tested for obtaining the refractive index from the measured data. The Sentech 850SE ellipsometer software calculates the refractive index for ITO by a Cauchy model, where the refractive index is approximated by[25]

$$n(\lambda) = n_0 + 10^2 \cdot \frac{n_1}{\lambda^2} + 10^7 \cdot \frac{n_2}{\lambda^4} \tag{2.1}$$

$$k(\lambda) = k_0 + 10^2 \cdot \frac{k_1}{\lambda^2} + 10^7 \cdot \frac{k_2}{\lambda^4} \tag{2.2}$$

where n_0, n_1, n_2, k_0, k_1 and k_2 are the parameters to fit. A Cauchy-Urbach model[26] and a Tauc-Lorentz model[27] were also tested, but the Cauchy model generally gave the best fit determined from the coefficient of determination. The refractive index of ITO determined from the Cauchy model is shown in Fig. E.1 in App. E and was obtained by averaging over the refractive indices from several samples.

The sheet resistance of the deposited ITO layers on flat PMMA surfaces was obtained by measuring the voltage drop with respect to current in a SUSS MicroTec four point probing setup and then applying the van der Pauw method. In the van der Pauw method, the sheet resistance R_s is found by solving the formula[28]

$$\exp\left(\frac{-\pi R_{AB,CD}}{R_s}\right) + \exp\left(\frac{-\pi R_{BC,DA}}{R_s}\right) = 1, \tag{2.3}$$

where $R_{AB,CD} = V_{CD}/I_{AB}$ and $R_{BC,DA} = V_{DA}/I_{BC}$ for a four point probing setup as shown in Fig. 2.6. The method requires that the sample is homogeneous in thickness[28], which means that the sheet resistance cannot be determined directly from the microstructured samples.

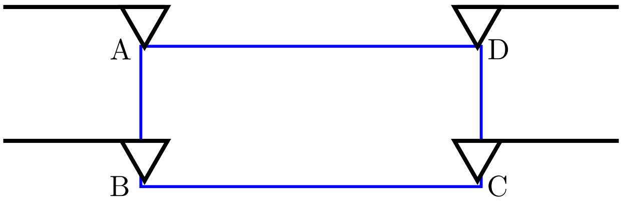

Figure 2.6. Four point probing setup for the van der Pauw method.

Eq. 2.3 is solved by the Newton-Raphson method using the iterative formula[29]

$$(R_s)_{i+1} = (R_s)_i - f((R_s)_i)/f'((R_s)_i), \tag{2.4}$$

where

$$f(R_s) = \exp\left(\frac{-\pi R_{AB,CD}}{R_s}\right) + \exp\left(\frac{-\pi R_{BC,DA}}{R_s}\right) - 1. \tag{2.5}$$

Eq. 2.4 is solved until the difference between $(R_s)_{i+1}$ and $(R_s)_i$ is less than $1{\cdot}10^{-5}$ Ω/□. The sheet resistance with respect to ITO thickness is shown in Fig. 2.7.

2.4 Deposition of silicon

Amorphous silicon was deposited with an STS PECVD system using silane as gas source. A low temperature recipe for Si deposition was made in order to comply with the low melting point of PMMA. The optimization of the Si deposition is described in App. A. The PECVD settings used for deposition are shown in Tab. 2.2.

The thickness of the deposited layers was measured by depositing Si on glass concurrently with the Si deposition on PMMA molds and then measuring the thickness by ellipsometry after deposition.

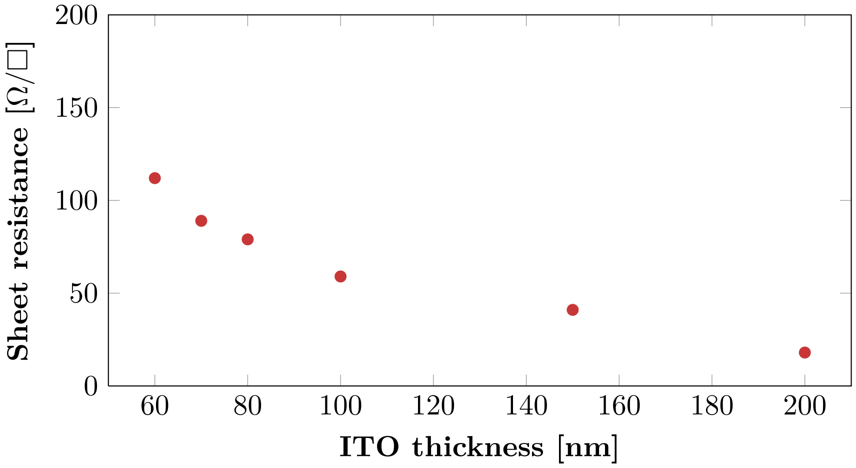

Figure 2.7. Sheet resistance of ITO with varying film thickness.

Parameter	Setting
Substrate temperature	50°C
Showerhead temperature	170°C
Process pressure	100 mtorr
Silane flow	50 sccm
Power	50 W

Table 2.2. PECVD settings for deposition of Si on PMMA.

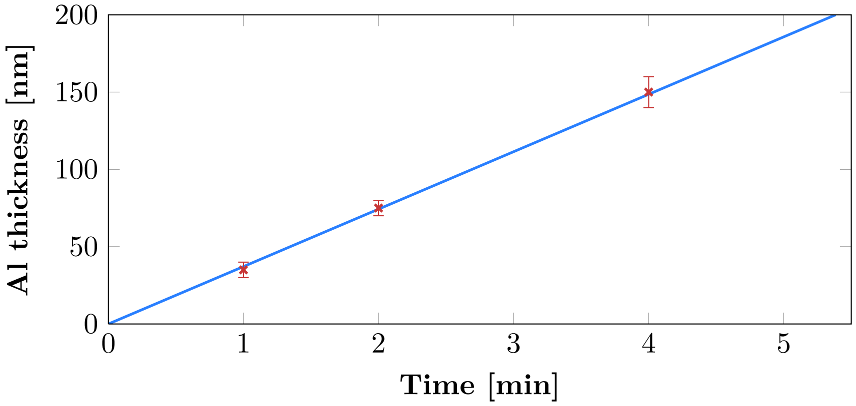

Figure 2.8. Al thickness with respect to deposition time. The red marks show the data points and variations in measurements, while the solid line is a linear fit where $f(t) = t \cdot 37.14$ nm/min.

The ellipsometric measurements were used to determine the refractive index of the Si layer following a Tauc-Lorentz model[27,30] which is described in App. A. The refractive index obtained for the Si is shown in Fig. E.2 in App. E. It is seen that the extinction coefficient for the Si deposited by the low temperature process is lower than for the refractive index used for simulations. The extinction coefficient drops to zero between 700-800 nm and the Si layer was therefore not expected to absorb light above that wavelength. It should be noted that there were some issues with obtaining uniform layers of Si when depositing Si on more than one sample at the same time.

2.5 Deposition of aluminum

The Al layers were deposited with an SVS 2400 sputtering system. Fig. 2.8 shows how the Al thickness varies with respect to deposition time t with the sputtering power set to 400 W. The Al thickness was measured with an Ambios XP-2 surface profiler. An Al layer with a thickness of 150 nm was deposited on all samples as there is no transmission through such a layer. The transmission through Al layers with varying thickness is shown in Fig. A.12 in App. A.

Chapter 3

Experimental results

Imprints were made of five different masters. Four anodized Al masters and one etched c-Si master were used. The imprints and the deposited layers were characterized by SEM, AFM, and UV/VIS/NIR spectroscopy. The anodized masters are compared to the imprints and the reflection and transmission of imprinted samples will be presented.

3.1 SEM characterization of imprints

SEM (Zeiss EVO 60) images of imprints from the etched c-Si master are shown in Figs. 3.1 and 3.2. Fig. 3.1a shows how the master was made by patterning areas of 100 by 100 μm^2 next to each other, while Fig. 3.1b highlights an area where four patterned areas overlap.

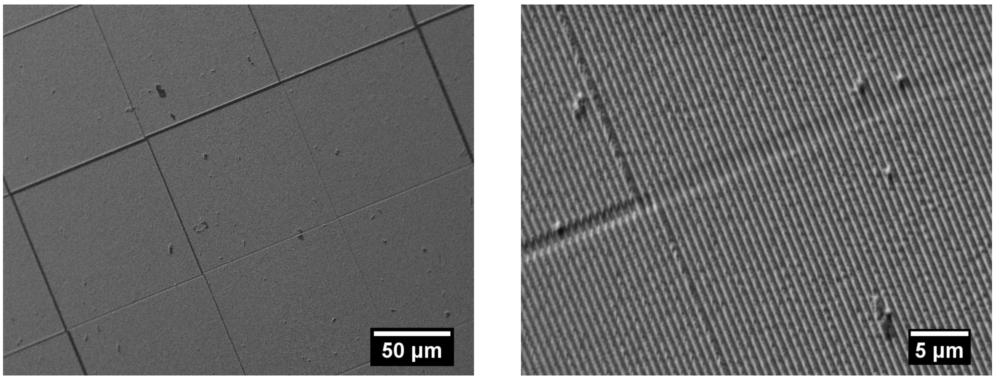

a) b)

Figure 3.1. SEM images of imprints from etched c-Si sample. a) Patterned areas next to each other and b) zoom on a spot where four patterned areas meet.

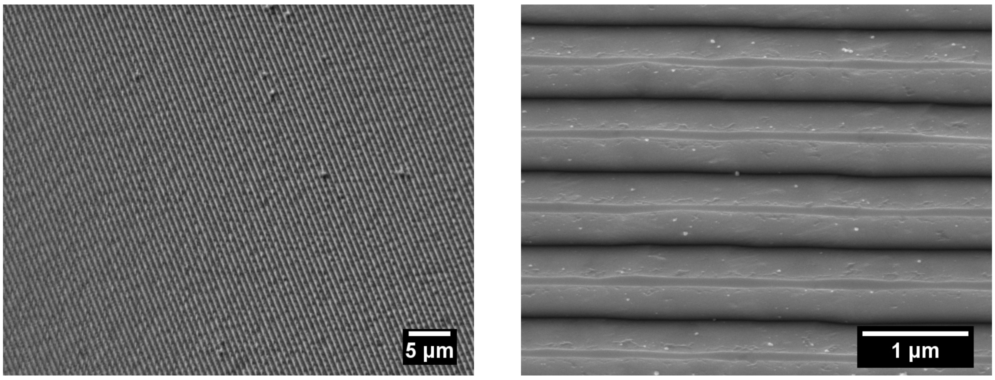

a) b)

Figure 3.2. SEM images of imprints from etched c-Si sample. a) The patterned areas seem uniform and b) the period is ~700 nm. b) was acquired with a Zeiss 1540 XB SEM by research assistant Peter Kjær Kristensen.

In Fig. 3.2 it is easy to see that the imprinted structure from the etched c-Si master is a 2D structure that is uniform along the third direction.

Figs. 3.3, 3.4, 3.5, and 3.6 show SEM images of the four anodized Al masters and the corresponding imprints in PMMA. The microstructures from the masters were obviously transferred to the PMMA and the results shown here were easy to reproduce.

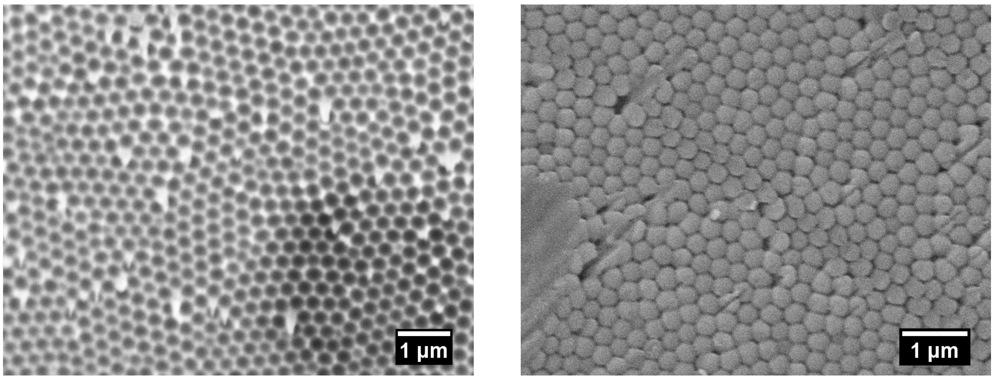

a) b)

Figure 3.3. SEM images of OA samples. a) Master and b) imprint in PMMA.

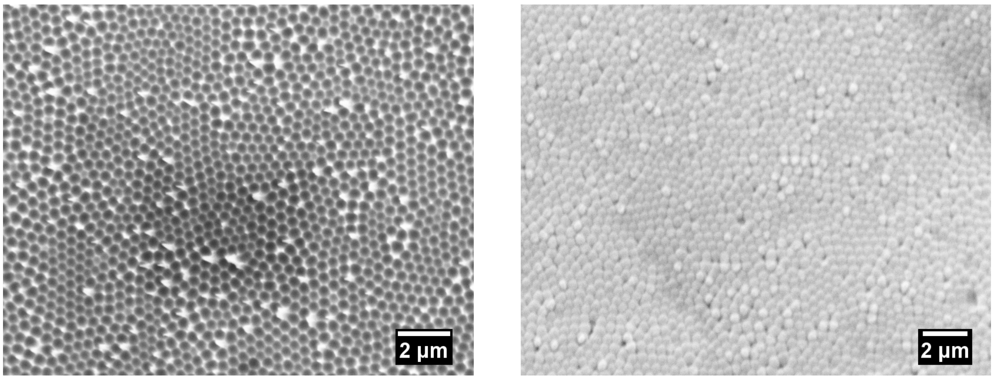

a) b)

Figure 3.4. SEM images of PA samples. a) Master and b) imprint in PMMA.

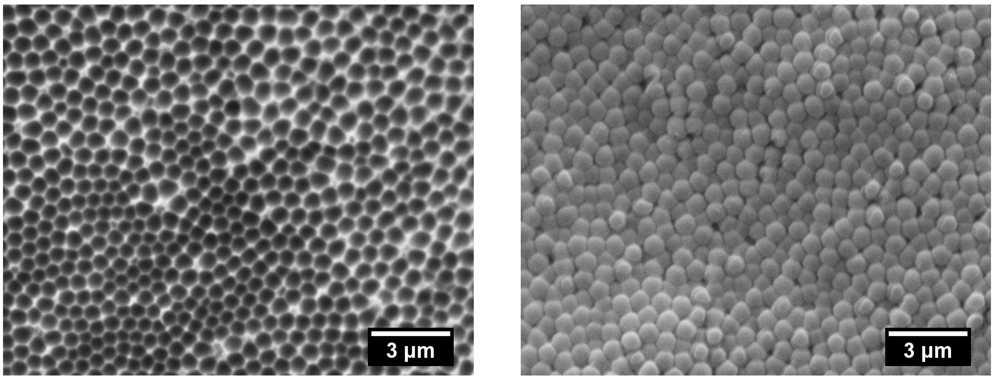

a) b)

Figure 3.5. SEM images of CA1 samples. a) Master and b) imprint in PMMA.

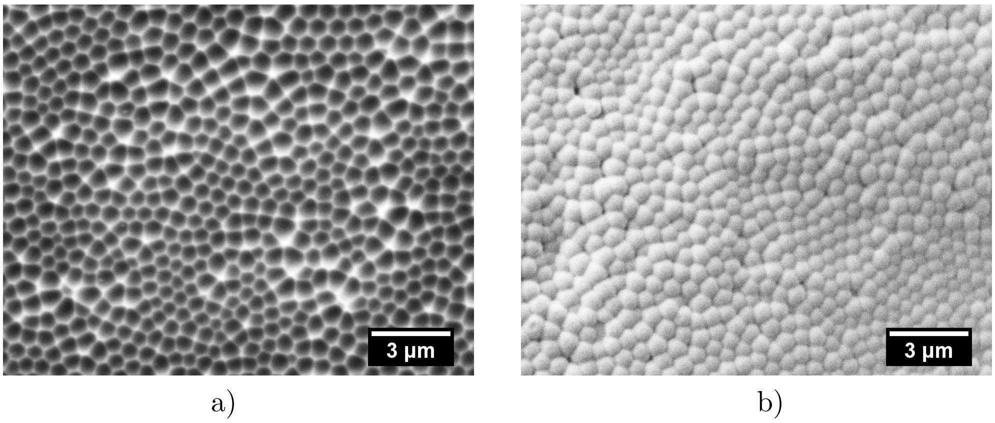

a) b)

Figure 3.6. SEM images of CA2 samples. a) Master and b) imprint in PMMA.

It is seen that the OA samples in Fig. 3.3 have the highest degree of ordering followed by PA, CA1, and CA2 samples, respectively. The OA master has a relatively high degree of ordering with many grains were there is the desired hexagonal ordering. The PA sample has some areas where there the hexagonal ordering is present. The CA1 sample has a smaller extent of hexagonal ordering, while CA2 is quite disordered.

3.2 AFM characterization of imprints

The imprints from the anodized samples were characterized by AFM in order to examine the surface such that a model could be made for simulations. Figs. 3.7, 3.8, 3.9, and 3.10 show AFM images of the imprints from the anodized masters. The images that are shown here highlight areas with a high degree of hexagonal ordering, but the ordering found from the AFM analysis does generally follow what was seen in the SEM images in Sec. 3.1. It should be noted that the height of the imprinted structures does not completely match the indentation depths in Tab. 2.1. This could be because the microstructures from the masters are not transferred 1:1, but it is assumed that it is due to the resolution of the AFM tip.

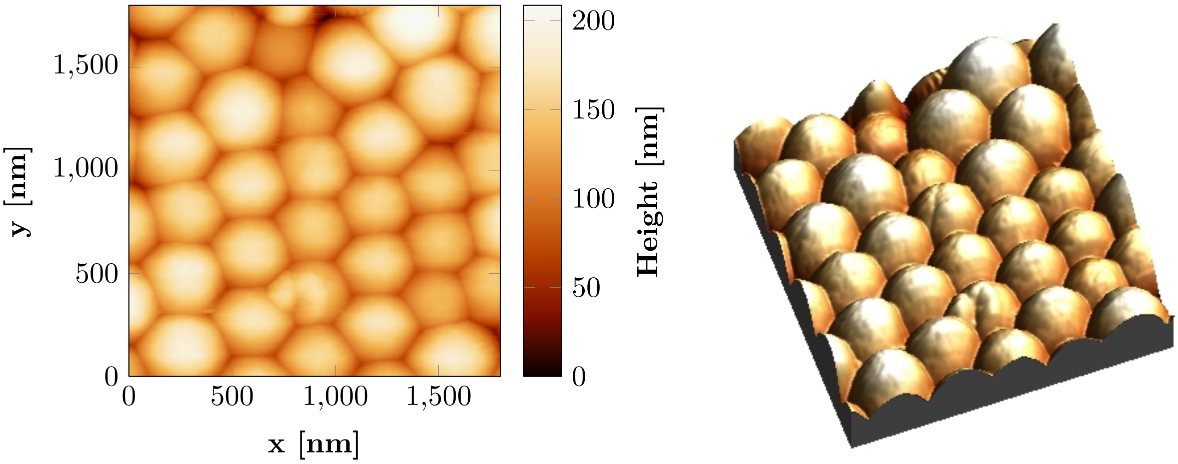

Figure 3.7. AFM images of OA imprint.

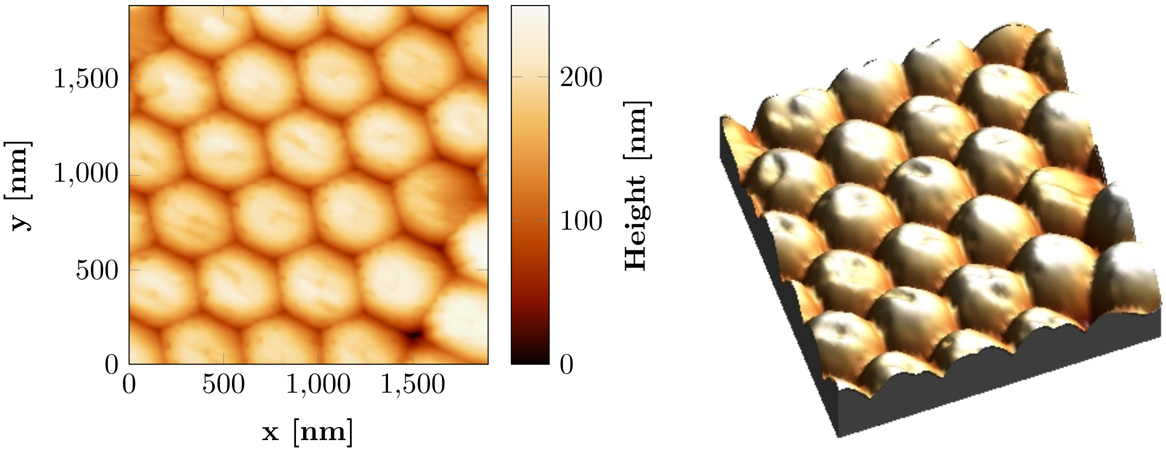

Figure 3.8. AFM images of PA imprint.

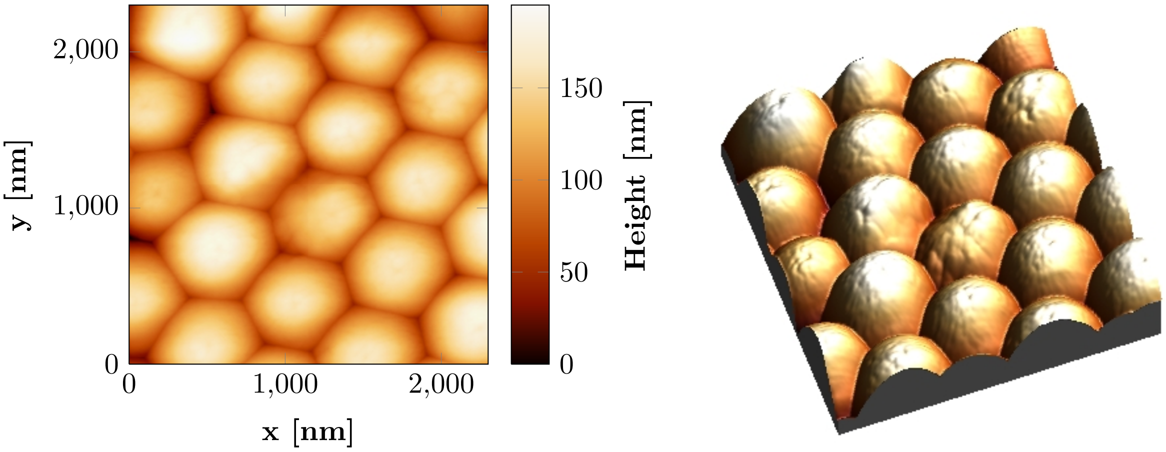

Figure 3.9. AFM images of CA1 imprint.

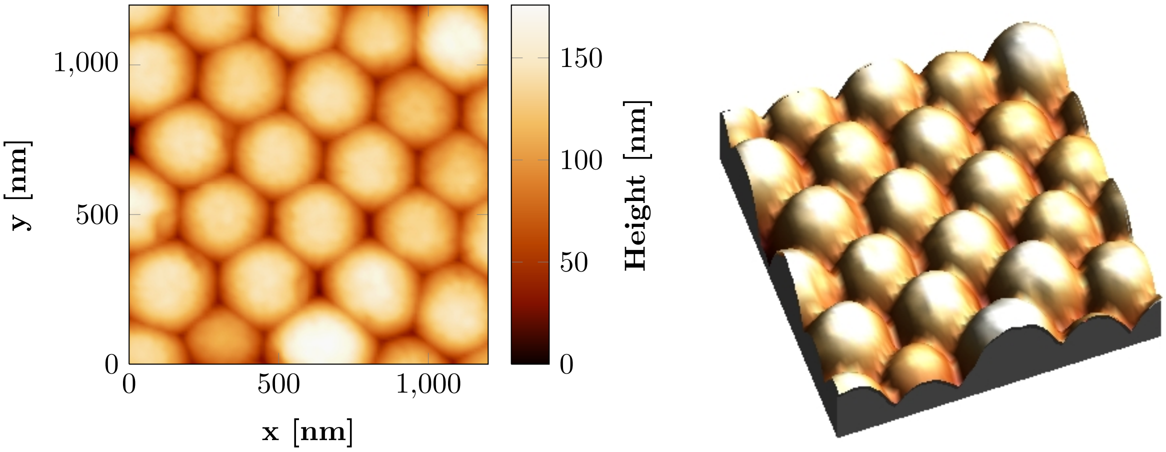

Figure 3.10. AFM images of CA2 imprint. The axes seems to be to small compared to the period of the CA2 samples.

AFM images of an imprint from the etched c-Si master are shown in Fig. 3.11. The structure resembles what was seen in the SEM images in Sec. 3.1.

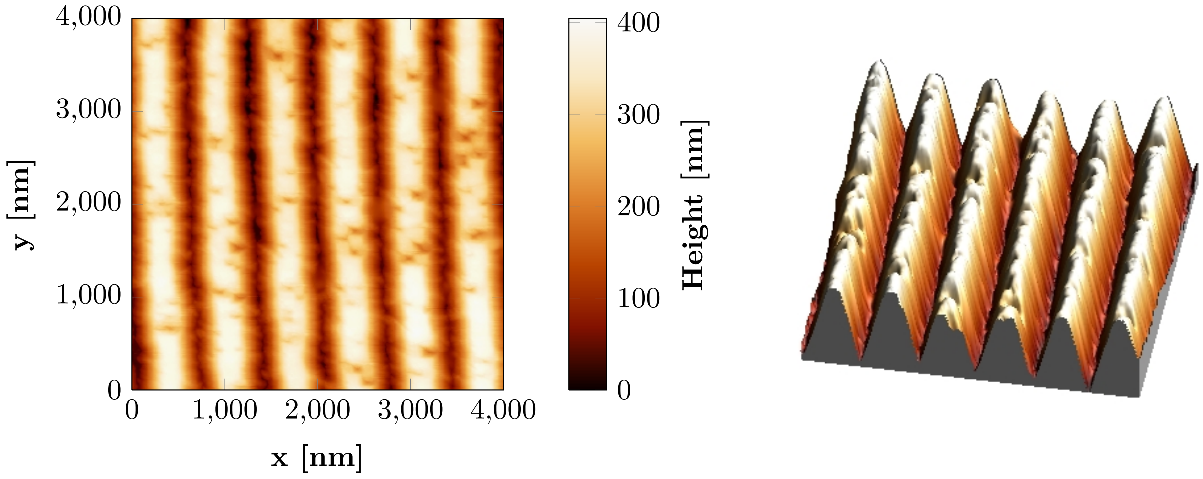

Figure 3.11. AFM images of imprint from etched c-Si master.

3.3 Characterization of deposited layers

ITO was deposited as the first layer on the imprinted substrates. Fig. 3.12 shows SEM images of PA imprints with varying ITO thickness. There is no big visual difference between the imprints with varying ITO thickness and the imprint with no ITO shown in Fig. 3.4b.

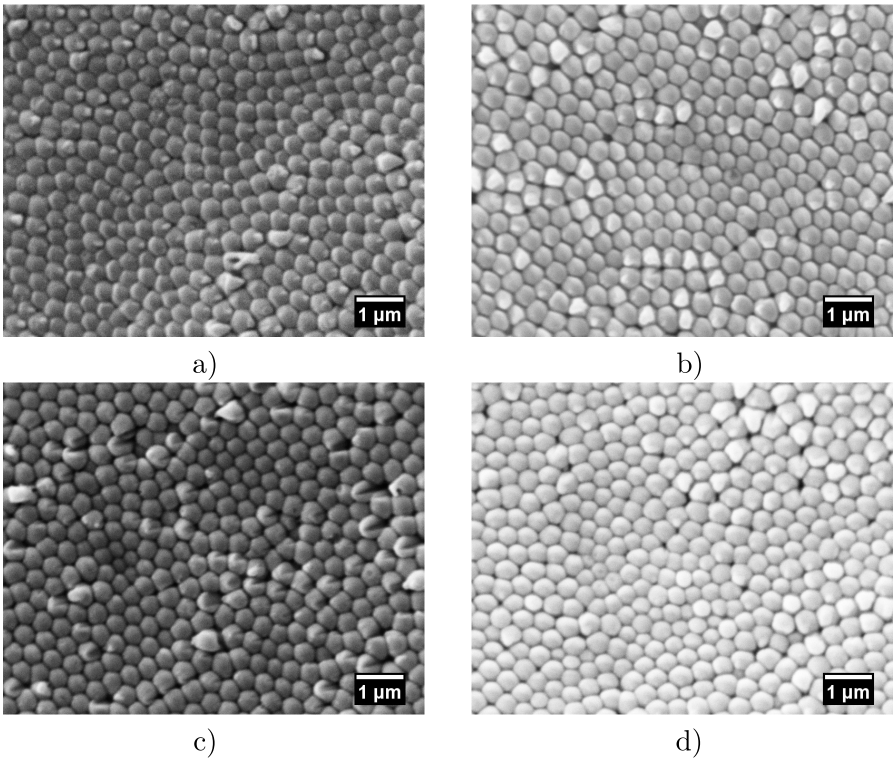

a) b)

c) d)

Figure 3.12. SEM images of PA imprints with a) 60 nm ITO, b) 80 nm ITO, c) 100 nm ITO, and d) 150 nm ITO.

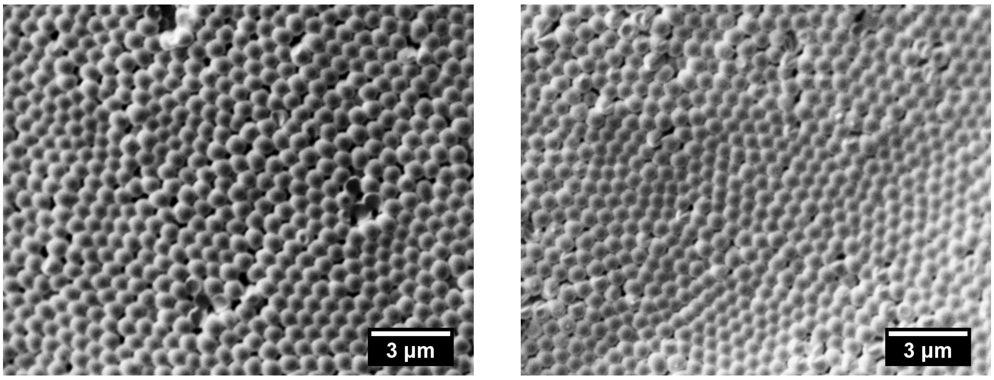

a) b)

Figure 3.13. SEM images of CA1 imprints with a) 70 nm ITO and b) 100 nm ITO.

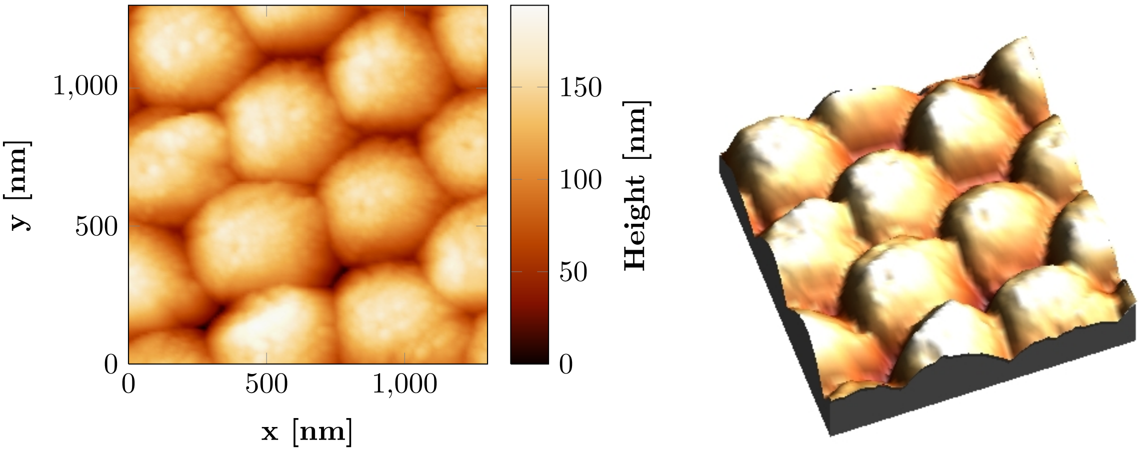

Figure 3.14. AFM images of PA imprint with 60 nm ITO.

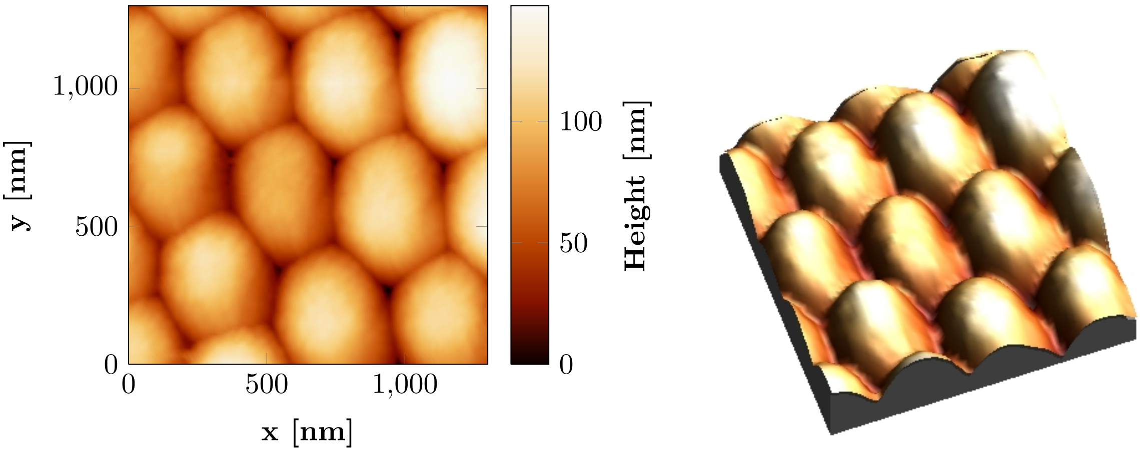

Figure 3.15. AFM images of PA imprint with 150 nm ITO.

Fig. 3.13 shows SEM images of CA imprints with 70 and 100 nm ITO deposited. There is again no apparent difference in the appearance of the imprints with ITO and the imprint without ITO shown in Fig. 3.5b.

AFM measurements were made on samples with ITO and Si deposited. Figs. 3.14, 3.15, and 3.16 show imprinted PA surfaces with 60, 150, and 200 nm ITO deposited, respectively. It is seen from the AFM images that the surface becomes more flat when ITO is deposited.

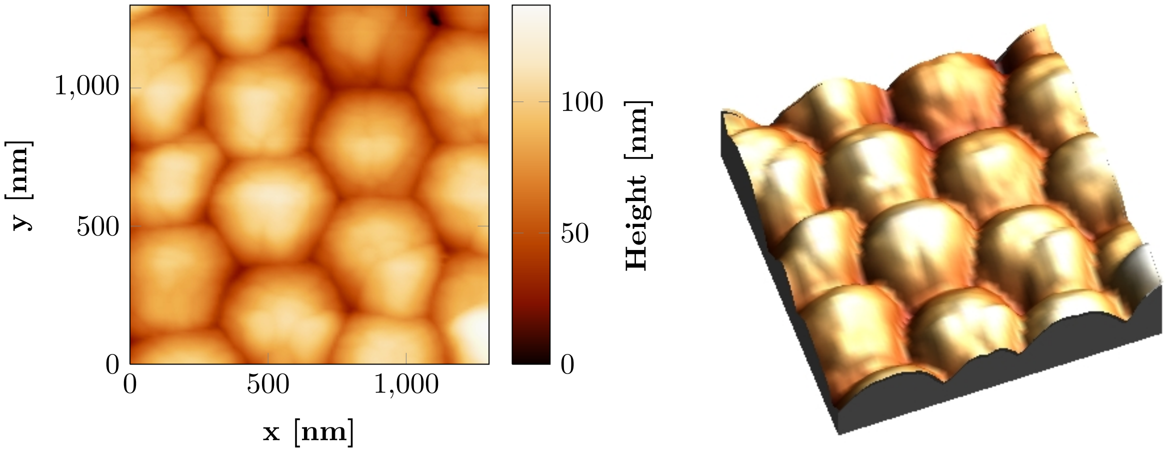

Figure 3.16. AFM images of PA imprint with 200 nm ITO.

PA surfaces with 300 nm Si deposited on an ITO layer are shown in Figs. 3.17, 3.18, and 3.19, which also show that a thicker deposited layer results in a more flat surface compared to the imprints with only ITO deposited. AFM images of PA and CA1 surfaces with varying Si thickness are shown in App. B. AFM topographies with deposited layers were mainly acquired for PA and CA1 samples.

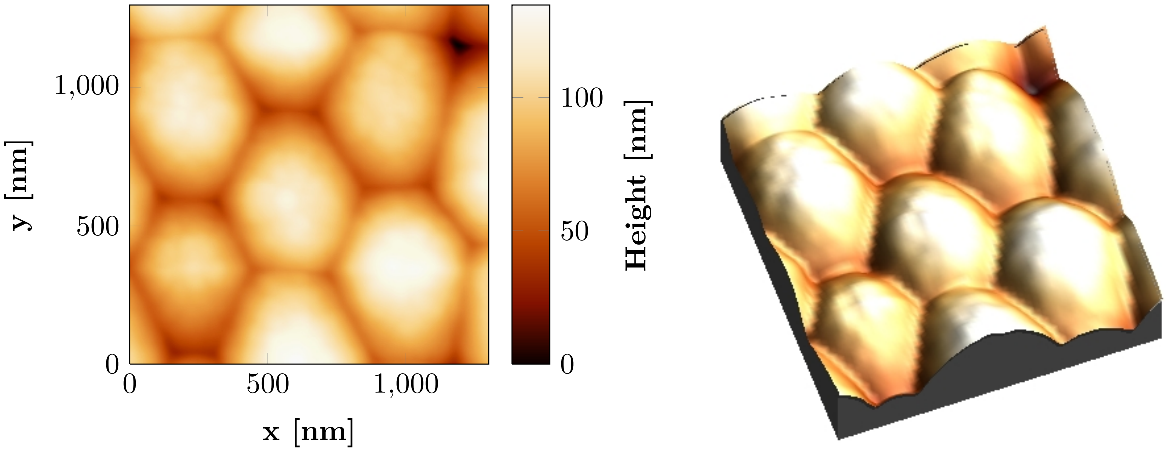

Figure 3.17. AFM images of PA imprint with 60 nm ITO and 300 nm Si.

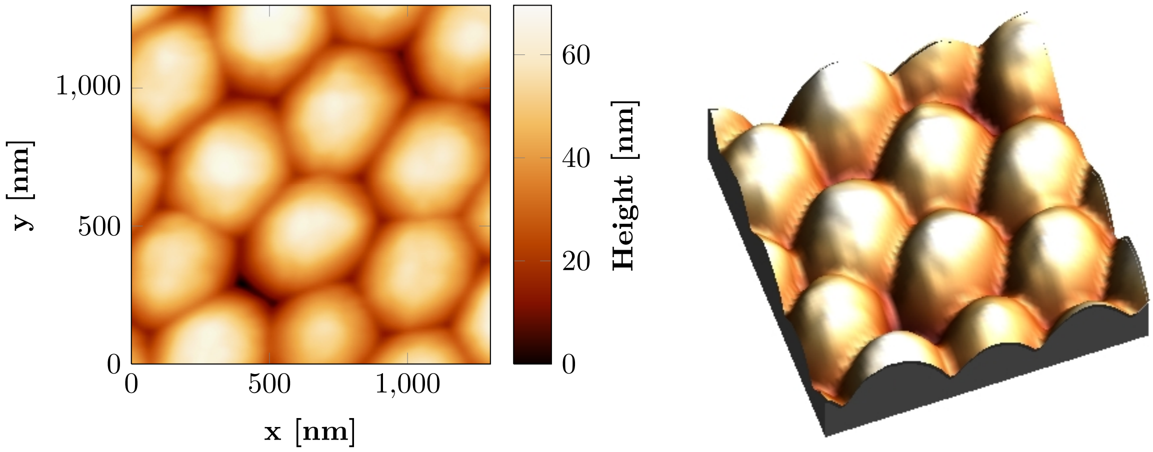

Figure 3.18. AFM images of PA imprint with 90 nm ITO and 300 nm Si.

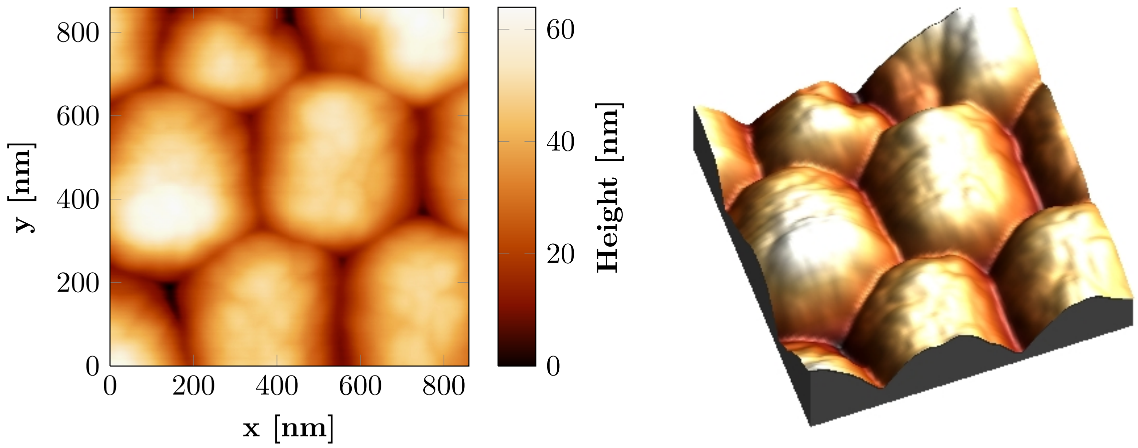

Figure 3.19. AFM images of PA imprint with 165 nm ITO and 300 nm Si.

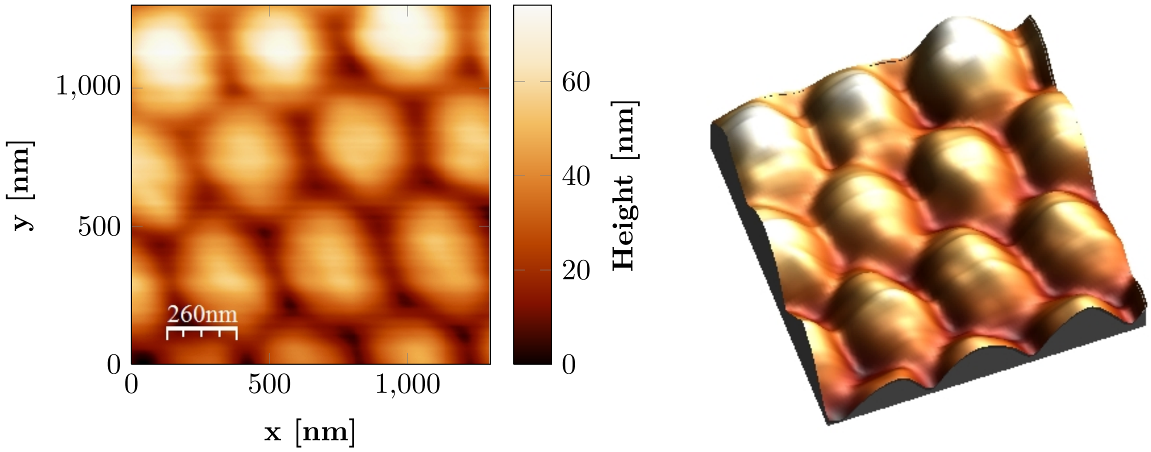

Figure 3.20. AFM images of PA imprint with 90 nm ITO, 300 nm Si, and Al.

A PA imprint with ITO, Si and Al is shown in Fig. 3.20. The surface appears flatter than the corresponding surface seen in Fig. 3.18 without an Al layer deposited.
Fig. 3.21 shows an imprint from the etched c-Si master with Si and Al deposited. The top surface is more rounded compared to Fig. 3.11, which indicates that the deposited layers are not uniformly deposited across the surface.

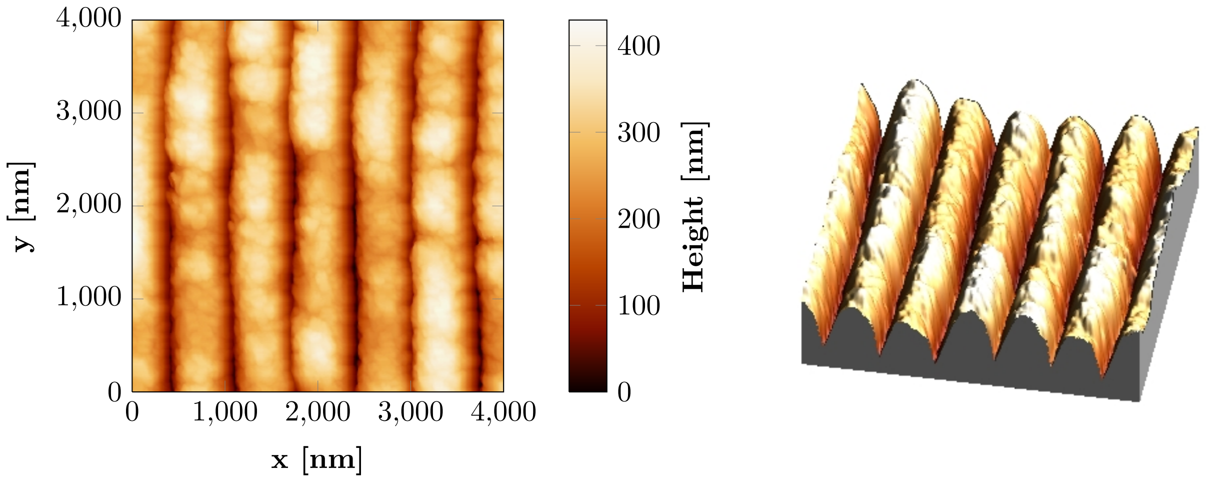

Figure 3.21. AFM images of imprint from etched c-Si master with 300 nm Si and Al.

3.4 Transmission and reflection measurements

Transmission and reflection measurements were carried out on imprints with varying ITO, Si and Al layers with a PerkinElmer LAMBDA 1050 UV/VIS/NIR spectrometer equipped with an integrating sphere. The light from the spectrometer is incident on the surface at an 8° angle. The measurements are shown for wavelengths ranging from 340–800 nm as the a-Si layer does not absorb light with a wavelength above 800 nm and the PMMA layer begins to absorb light for wavelengths below 400 nm. Measurements of the transmission, scattered transmission, and reflection were obtained for different samples according to the configurations shown in Fig. 3.22.

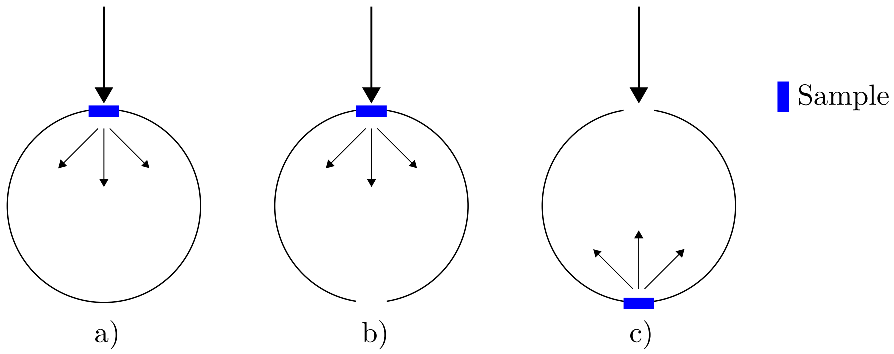

Figure 3.22. Measurement types carried out with a spectrometer equipped with an integrating sphere seen from above. a) Transmission, b) scattered transmission, and c) reflection.

The measurements are presented together with a figure as shown in Fig. 3.23 to give a quick overview about the measurement type being presented. The presented results are averages of measurements on different spots on the surfaces. Some additional transmission and reflection measurements are presented in App. C. The reflectance and transmittance for wavelengths from 400–800 nm with respect to the AM1.5 spectrum were calculated for the measured data and are presented as the solar reflectance R_s and solar transmittance T_s.

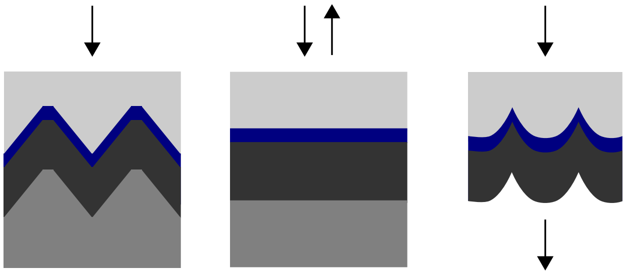

a) b) c)

Figure 3.23. Figures for explaining measurement types. a) Absorption, b) reflection, and c) transmission

Fig. 3.24 shows the reflection from flat PMMA surfaces with various layers of ITO, Si and Al deposited. It is noted that the reflection from a flat PMMA surface with 300 nm Si and Al deposited reflects ∼ 80% of the light from 700–750 nm. This was lowered by adding an ITO layer which has antireflective properties and the reflection went below the reflection from bare PMMA for wavelengths between 440–570 nm when the ITO layer had a thickness of 70 nm. It is seen in Tab. 3.1 that adding 70 nm ITO between PMMA and the Si layer more than halved the solar reflection.

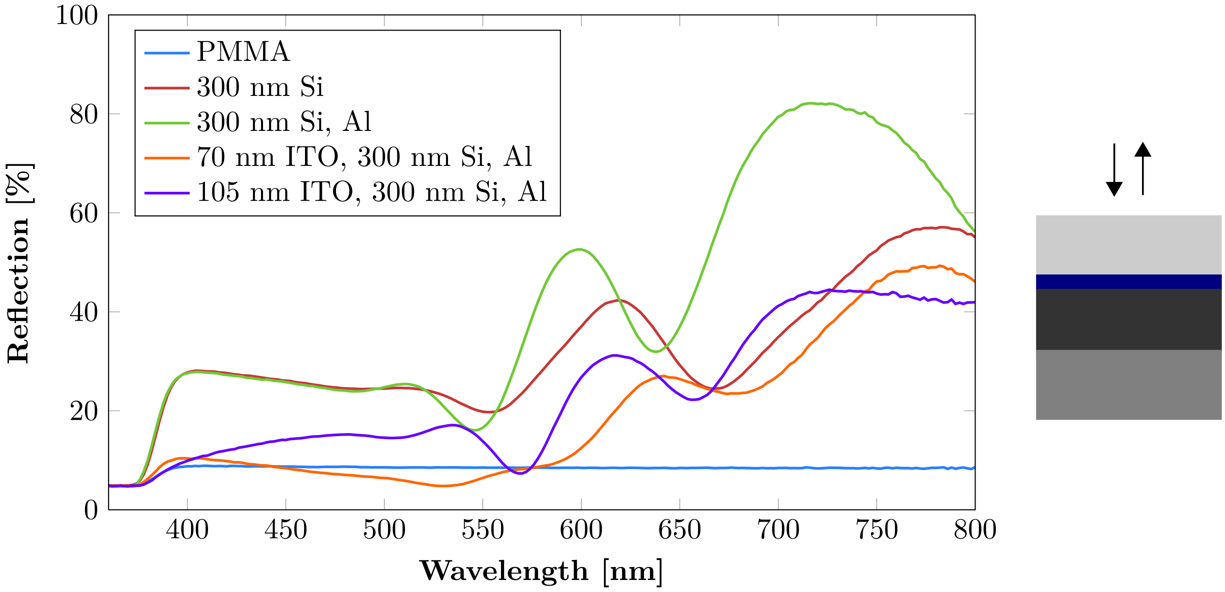

Figure 3.24. Reflection from flat PMMA samples with varying ITO, Si and Al layers.

ITO	$\boldsymbol{R_s}$
0 nm	0.467
70 nm	0.212
105 nm	0.261

Table 3.1. Solar reflectance for flat PMMA samples with varying ITO thickness, 300 nm Si and Al.

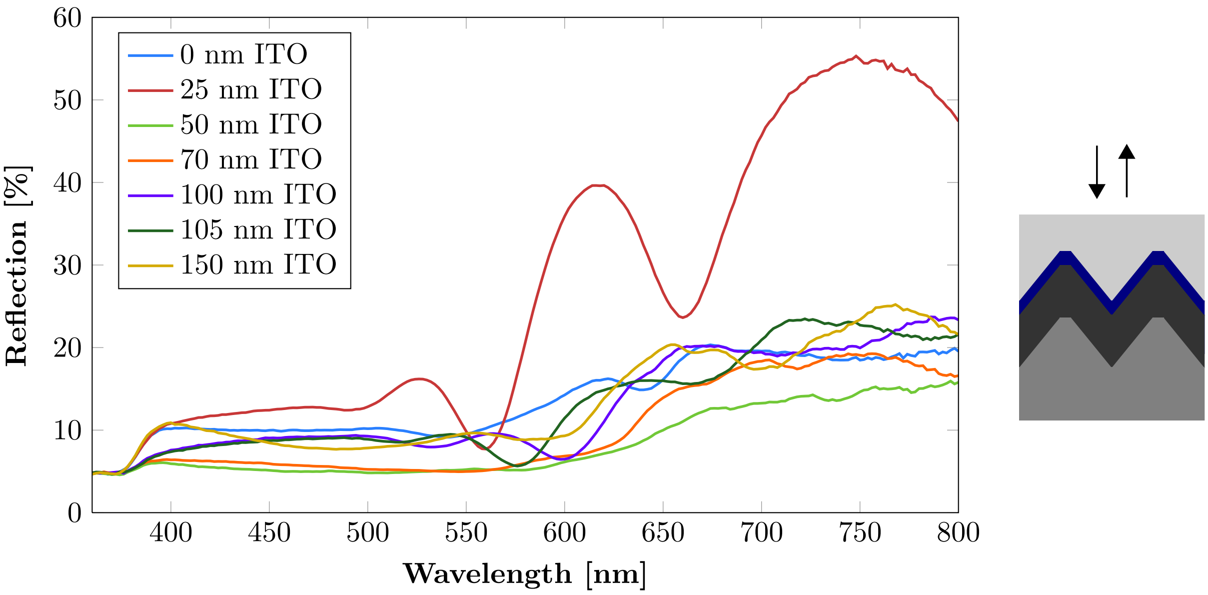

Figure 3.25. Reflection from imprints from etched c-Si master with varying ITO thickness, 300 nm Si, and Al.

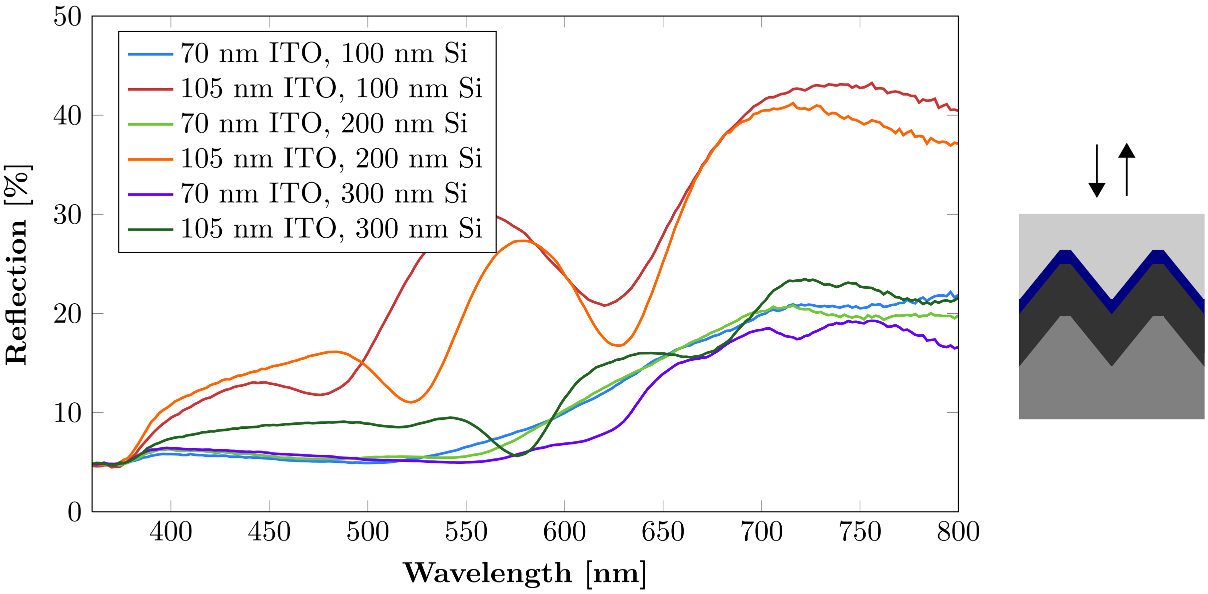

Figure 3.26. Reflection from imprints from etched c-Si master with varying ITO and Si thickness and Al.

The transmission was not measured for the imprints made from the etched c-Si master as the spot size for transmission measurements was larger than the imprinted area. The reflection from imprints based on the etched c-Si master is shown in Figs. 3.25 and 3.26. In Fig. 3.25 it is seen that the microstructuring itself lowers the reflection when comparing the reflection from the microstructure with no ITO to the flat PMMA surface without ITO in Fig. 3.24. The reflection from a microstructured area without ITO has a lower reflection than a flat surface with 70 nm ITO when comparing Tabs. 3.1 and 3.2. The reflection is generally lowered further by adding ITO and it is seen that a 50 nm layer of ITO results in the lowest reflection for this structure. When varying the Si thickness as shown in Fig. 3.26 it is seen that the reflection is lowest for an ITO layer of 70 nm compared to 105 nm for all the Si thicknesses shown which is confirmed in Tab. 3.3. Fig. C.2 in App. C shows that the 105 nm ITO layer is better than a 25 nm ITO layer for 200 and 300 nm Si, while the 25 nm ITO layer has the lowest reflection for 100 nm Si.

ITO	R_s
0 nm	0.147
25 nm	0.300
50 nm	0.090
70 nm	0.111
100 nm	0.140
105 nm	0.142
150 nm	0.146

Table 3.2. Solar reflectance for imprints from etched c-Si master with varying ITO thickness, 300 nm Si and Al.

ITO	**Si**	R_s
70 nm	100 nm	0.126
70 nm	200 nm	0.124
70 nm	300 nm	0.111
105 nm	100 nm	0.286
105 nm	200 nm	0.261
105 nm	300 nm	0.142

Table 3.3. Solar reflectance for imprints from etched c-Si master with varying ITO and Si thickness and Al.

The transmission through imprints from the anodized masters is shown in Fig. 3.27. It is seen that the transmission through bare PMMA and the OA imprint is almost the same, while the transmission is lower for the PA, CA1, and CA2 imprints. It also shows that the CA1 and CA2 samples scatter the light significantly more than the OA and PA imprints. The solar transmittance for the samples shown in Fig. 3.27 is seen in Tab. 3.4.

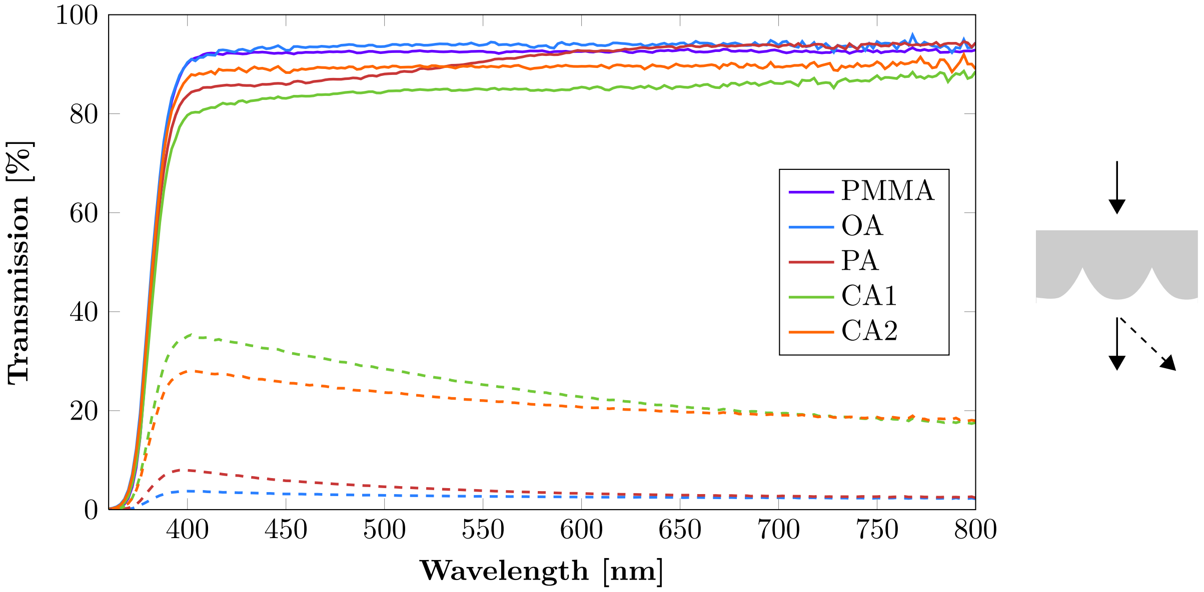

Figure 3.27. Transmission for imprints. Solid lines show transmission, while the dashed lines represent scattered transmission.

Sample	PMMA	OA	PA	CA1	CA2
T_s	0.925	0.938	0.914	0.853	0.895

Table 3.4. Solar transmittance for PMMA and imprinted samples.

Fig. 3.28 shows the transmission for OA imprints before Al deposition. There is not much difference between the transmission for different ITO thicknesses. It is noted that the imprints with ITO deposited seems to scatter the light less than the imprint without ITO. The reflection from OA imprints before and after Al deposition is shown in Fig. 3.29. The reflection seems to fluctuate more after Al deposition, but the overall reflection does not seem to change a lot.

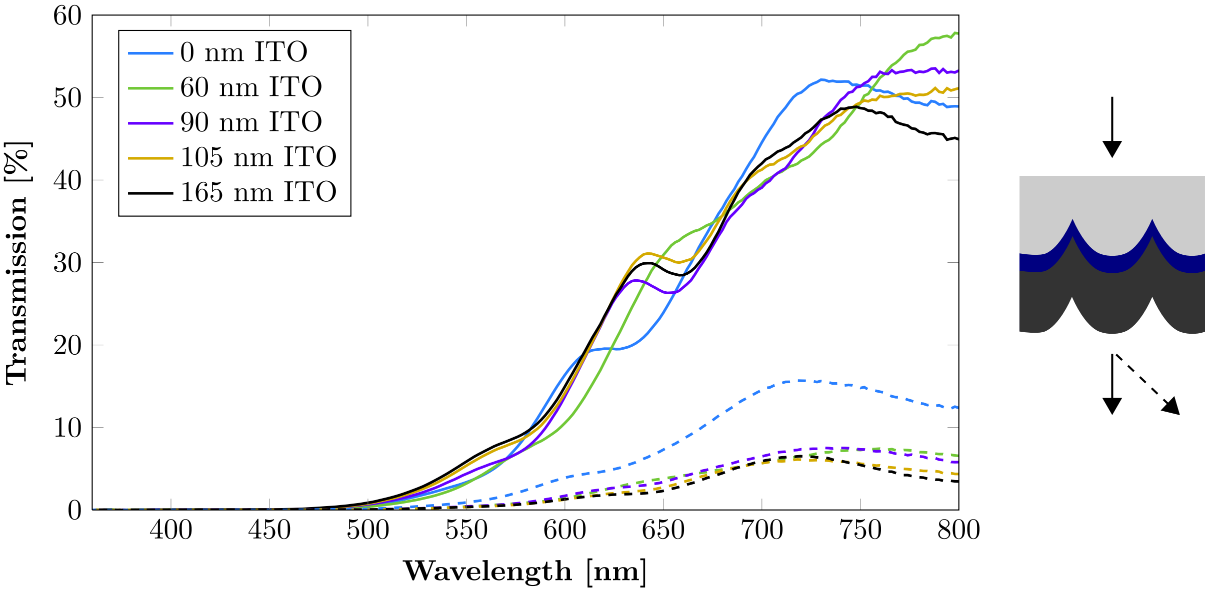

Figure 3.28. Transmission for OA imprints with varying ITO thickness and 300 nm Si. Solid lines show transmission, while the dashed lines represent scattered transmission.

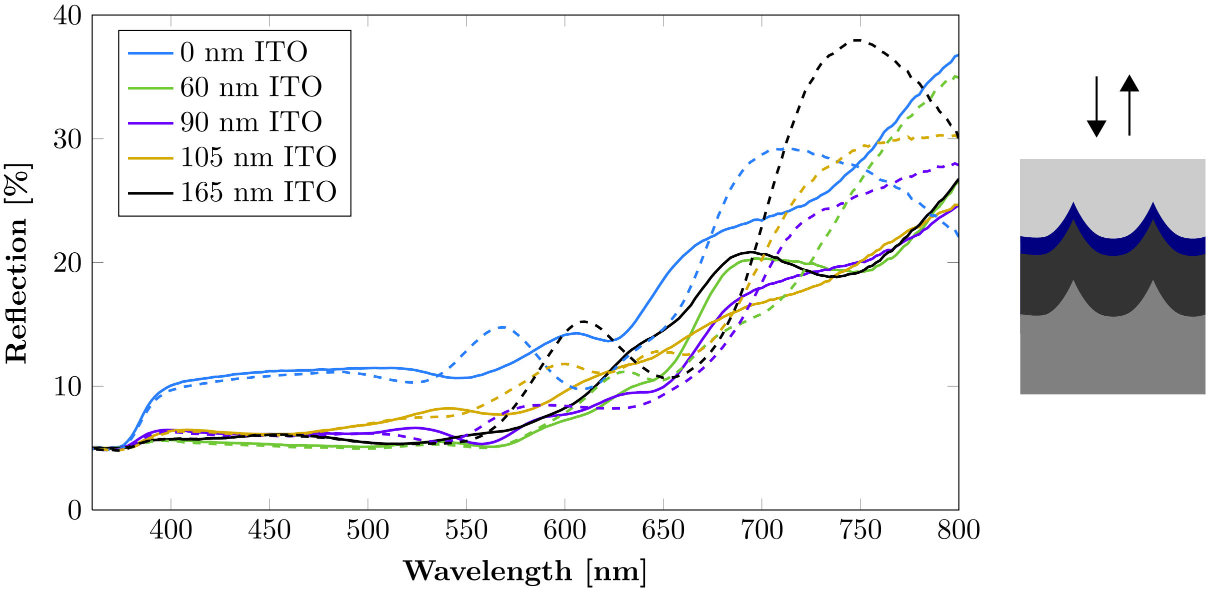

Figure 3.29. Reflection from OA imprints with varying ITO thickness and 300 nm Si. Solid lines show reflection before Al deposition, while dashed lines represent reflection after Al deposition.

The transmission for PA imprints before Al deposition is shown in Fig. 3.30. The transmission generally seems to increase with increasing ITO thickness, while the scattered transmission decreases with ITO thickness. Fig. 3.31 shows the reflection before and after Al deposition for

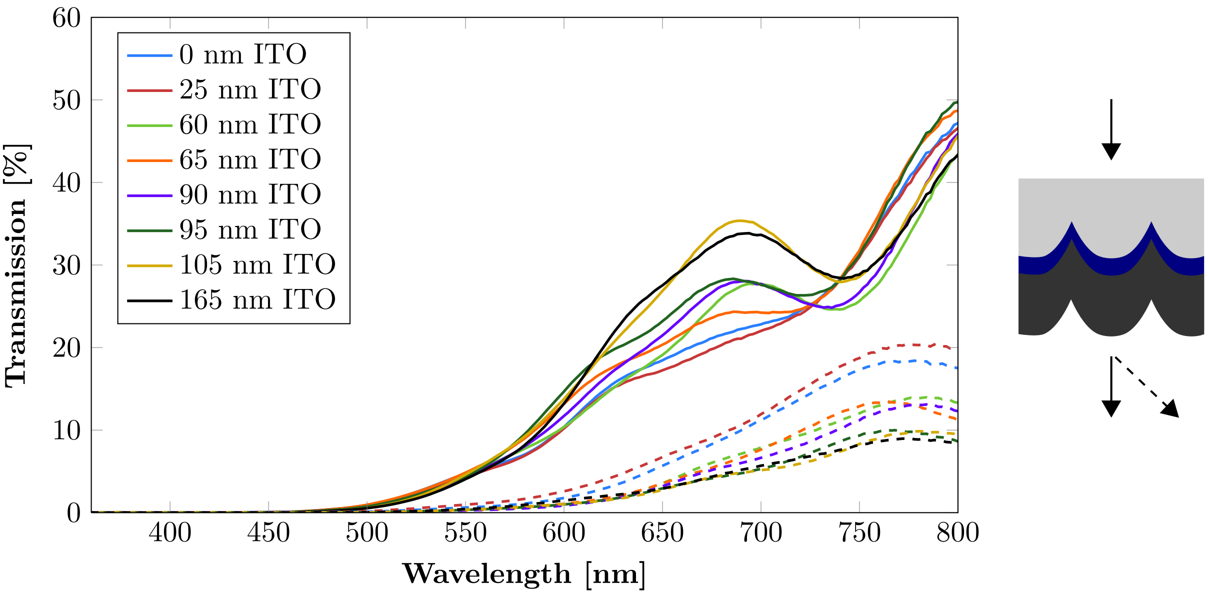

Figure 3.30. Transmission for PA imprints with varying ITO thickness and 300 nm Si. Solid lines show transmission, while the dashed lines represent scattered transmission.

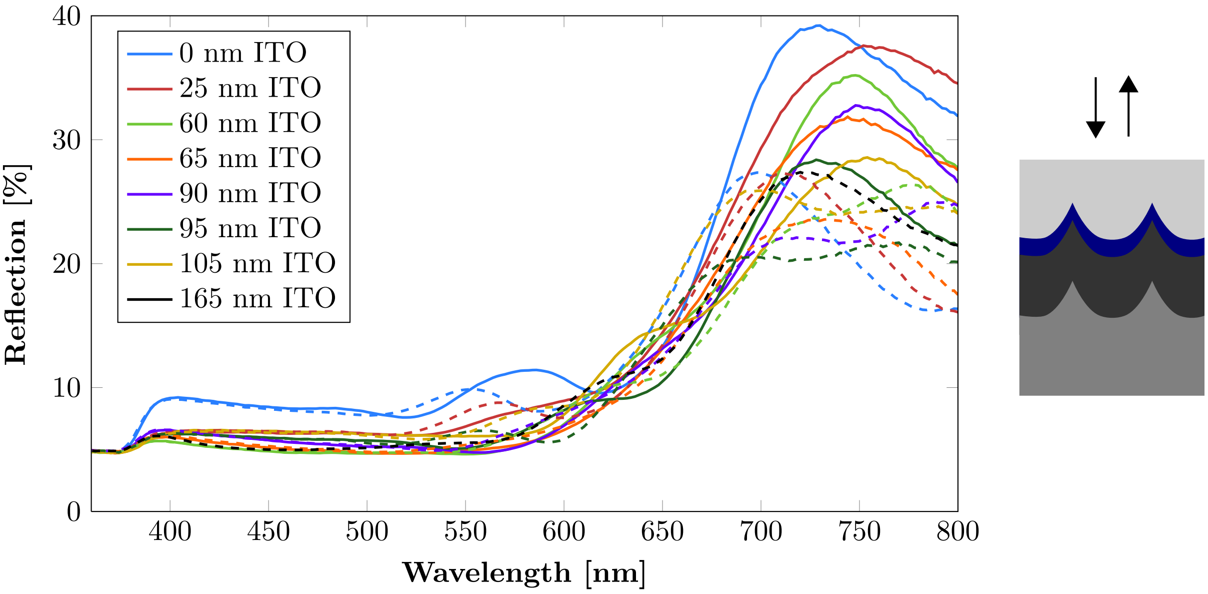

Figure 3.31. Reflection from PA imprintswith varying ITO thickness and 300 nm Si. Solid lines show reflection before Al deposition, while dashed lines represent reflection after Al deposition. There is no data for 165 nm ITO before Al deposition.

PA imprints, where the reflection is highest for the imprint with no ITO. It is seen that the reflection decreases after deposition of the Al layer, which means that the light absorbance in the cell increases substantially after Al deposition. Fig. C.3 in App. C show how the transmission for PA imprints changes with varying ITO and Si thicknesses, where it is seen that the transmission decreases with increasing Si thickness as expected.

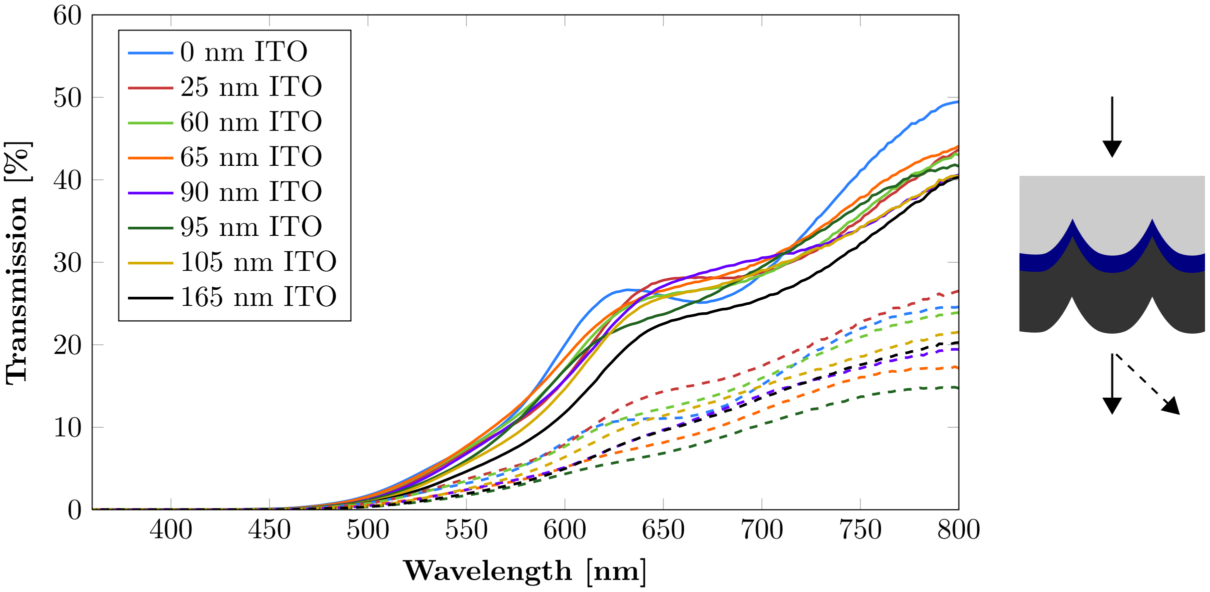

Figure 3.32. Transmission for CA1 imprints with varying ITO thickness and 300 nm Si. Solid lines show transmission, while the dashed lines represent scattered transmission.

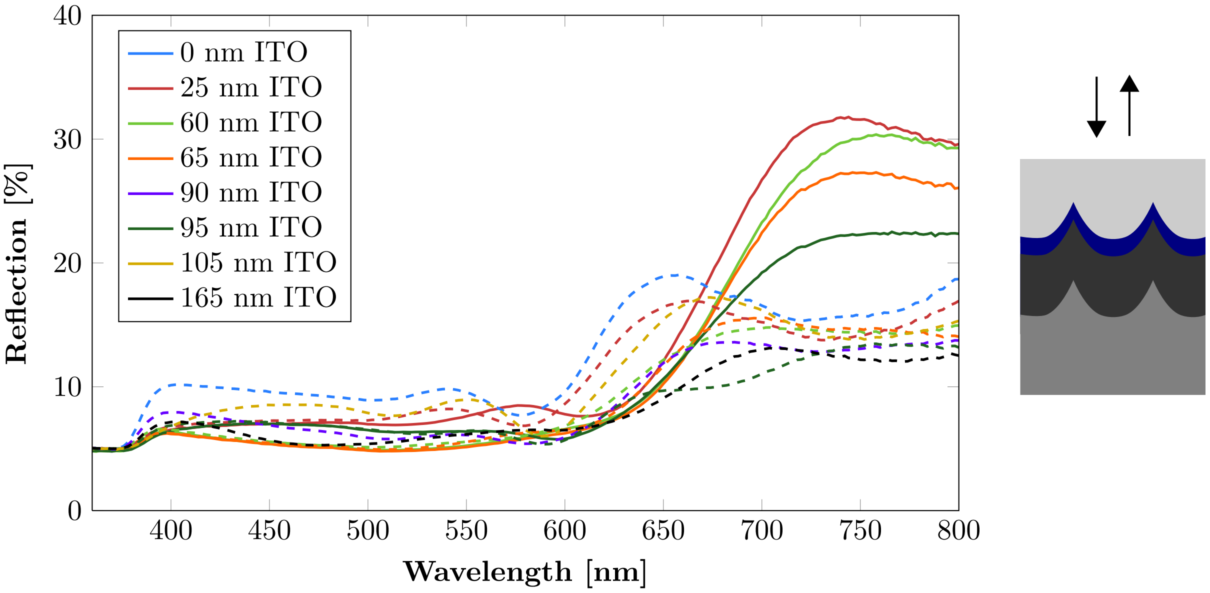

Figure 3.33. Reflection from CA1 imprints with varying ITO thickness and 300 nm Si. Solid lines show reflection before Al deposition, while dashed lines represent reflection after Al deposition. There are only plots of the reflection after Al deposition for 0, 90, 105, and 165 nm ITO.

Fig. 3.32 shows the transmission for CA1 imprints before Al deposition. There is not a big difference in the transmission for most of the samples except for the sample with no ITO which seems to transmit more light and the sample with 165 nm ITO which seems to transmit less light than the average. Fig. 3.33 shows the reflection before and after Al deposition for CA1 imprints. There is some data missing for the reflection before Al deposition, but it is seen that the reflection decreases after Al deposition as it did for the PA imprints. The transmission for CA1 imprints with varying ITO and Si thickness is shown in Fig. C.5 in App. C. The 95 nm ITO layers seem to result in the lowest transmission for the CA1 imprints, which is opposite to the PA imprints shown in Fig. C.3 where 65 nm ITO results in the lowest transmission. The advantage of using 95 nm ITO over 65 nm ITO is also seen in Fig. C.6 in App. C, which shows the reflection from CA1 imprints with varying ITO and Si thickness.

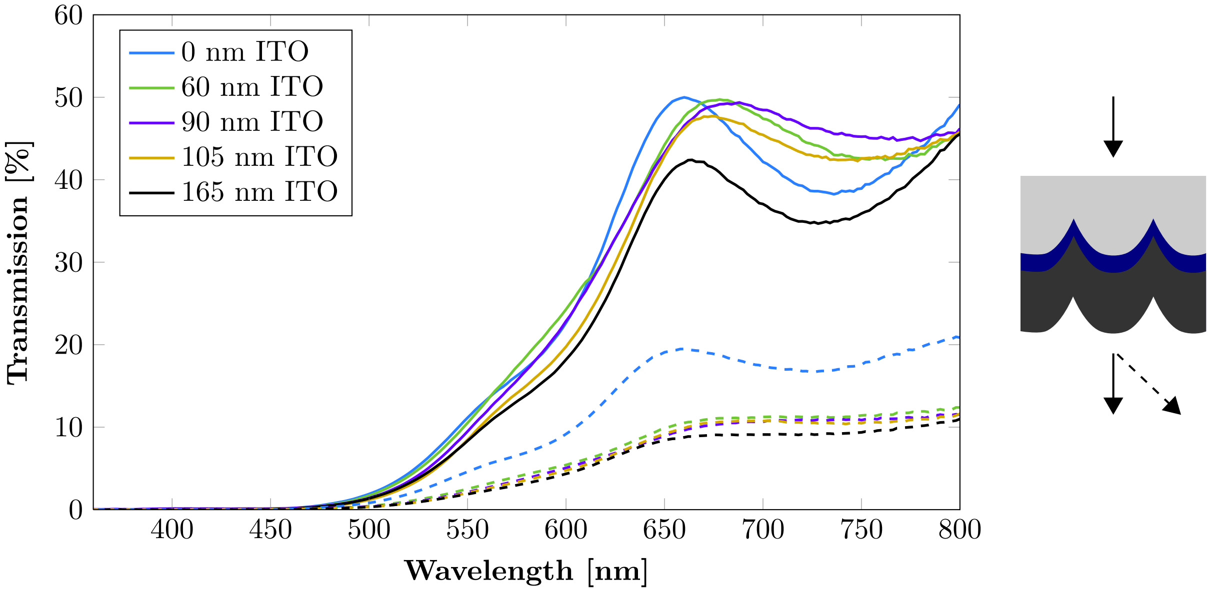

Figure 3.34. Transmission for CA2 imprints with varying ITO thickness and 300 nm Si. Solid lines show transmission, while the dashed lines represent scattered transmission.

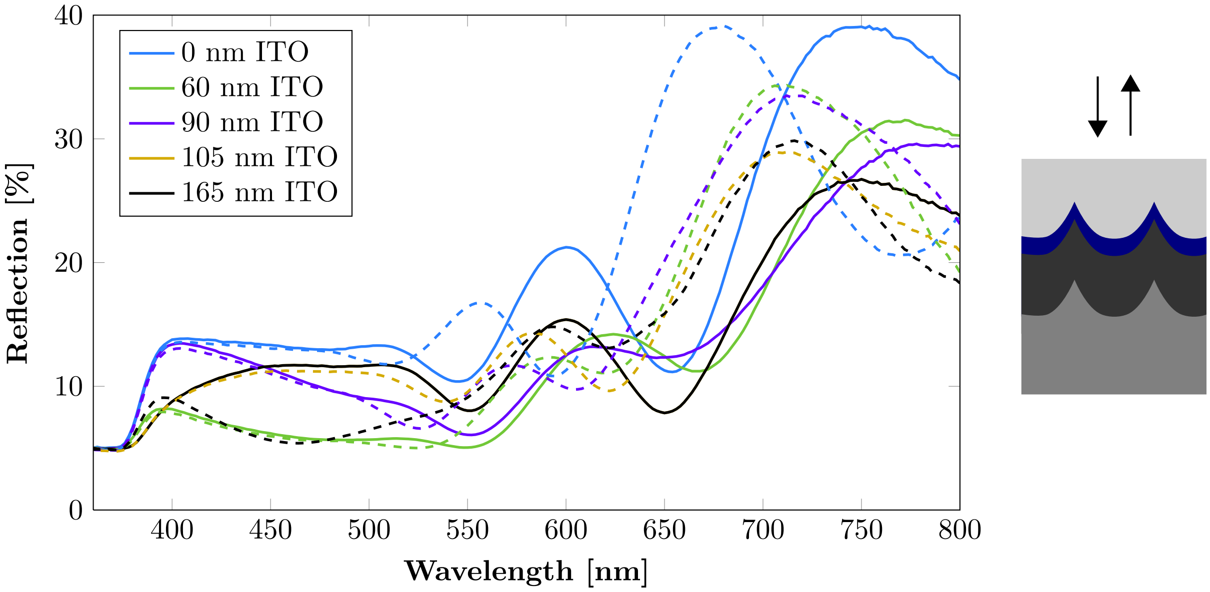

Figure 3.35. Reflection from CA2 imprints with varying ITO thickness and 300 nm Si. Solid lines show reflection before Al deposition, while dashed lines represent reflection after Al deposition.

The transmission for CA2 imprints before Al deposition is shown in Fig. 3.34, while Fig. 3.35 shows the reflection before and after Al deposition. The measurements from the CA2 sample follow the same tendencies as for the OA imprints, where the transmission is relatively unaffected by the

ITO thickness and where the sample with no ITO scatters the light more than the samples with ITO. The reflection from the samples is also seen not to decrease after deposition of Al.

The solar reflectance for some of the imprints based on the anodized masters with ITO, Si and Al is shown in Tab. 3.5. It is seen that the CA1 imprints had the lowest reflection for all the ITO thicknesses shown followed by the PA imprints. The reflection is generally lowest with 60 and 90 nm ITO, but it decreases again for an ITO thickness of 165 nm for the PA, CA1, and CA2 imprints.

ITO	$\boldsymbol{R_s}$	$\boldsymbol{R_s}$	$\boldsymbol{R_s}$	$\boldsymbol{R_s}$
	OA	**PA**	**CA1**	**CA2**
0 nm	0.180	0.142	0.131	0.208
60 nm	0.126	0.124	0.097	0.164
90 nm	0.125	0.125	0.094	0.182
105 nm	0.146	0.143	0.114	0.166
165 nm	0.158	0.132	0.087	0.155

Table 3.5. Solar reflectance for imprints from anodized master with varying ITO thickness, 300 nm Si and Al.

From the transmission and reflection measurements for the imprints based on the anodized samples it was seen that the PA and CA1 imprints and the OA and CA2 samples showed similar behavior. This could indicate that the indentation depth in the anodized master shown in Tab. 2.1 has more influence on the behavior than the period of the microstructures.

Chapter 4

Simulations

Models were made for running simulations of the optical properties of imprints based on the etched c-Si, the PA and the CA1 masters. An ideal structure was simulated for the imprints from the etched c-Si master, while a model based on the topography of the samples acquired by AFM was made for the PA and CA1 imprints. The structure of the imprints based on the etched c-Si master will be referred to as the triangular structure.

Simulations were carried out using *Lumerical FDTD Solutions*. The convergence of the models that were set up was tested in order to obtain reliable results and the process of convergence testing is described in App. D. All simulations were carried out for a wavelength span from 400–800 nm with the settings described in App. D and the refractive index for PMMA from Kasarova et al.[31], for ITO and a-Si from the experiments, and for Al from Palik[32]. The refractive indices are shown in App. E.

The simulations were used to find the absorption in the Si layer where the photo current should be generated. The external quantum efficiency (EQE) for an Si layer is determined as the ratio $\text{EQE}(\lambda) = P_{abs,Si}(\lambda)/P_{tot}(\lambda)$, where $P_{abs,Si}$ is the power of the light absorbed in the Si layer and P_{tot} is the total power of the incident light. The EQE was used to determine the internal quantum efficiency (IQE), which correspond to the EQE weighted with respect to the AM1.5 solar photon flux N_{ph} shown in Fig. 1.1. The IQE is therefore calculated as[33]

$$\text{IQE} = \frac{\int N_{ph}\text{EQE}(\lambda)d\lambda}{\int N_{ph}d\lambda}. \tag{4.1}$$

The IQE is used as a figure of merit for comparing simulated results for different structures.

4.1 Triangular structure

The simulations in *Lumerical* for the triangular structure were set up as a 2D model with the modeling parameters and boundary conditions shown in Fig. 4.1. Simulations were only carried out for normally incident light for which reason periodic boundaries were used to include the periodicity of the structure. The PML boundaries are perfectly matched layers that absorb incident light with minimum reflection.

The boundary above the structure and the light source were placed inside the PMMA layer in order to keep the simulation cell as small as possible. The intensity of light inside a PMMA layer for a light source positioned in air was simulated in another simulation and was multiplied with the light intensities obtained by different monitors in the simulation cell. A reflection monitor was placed between the light source and the top boundary to obtain the reflection from the surface, while a transmission monitor was placed in the air between the Al layer and the bottom boundary to obtain the transmission.

Lumerical contains an advanced absorption monitor that can obtain the spatial absorption in a simulation cell[34]. This monitor is used to find the absorption in the Si layer, which is used to

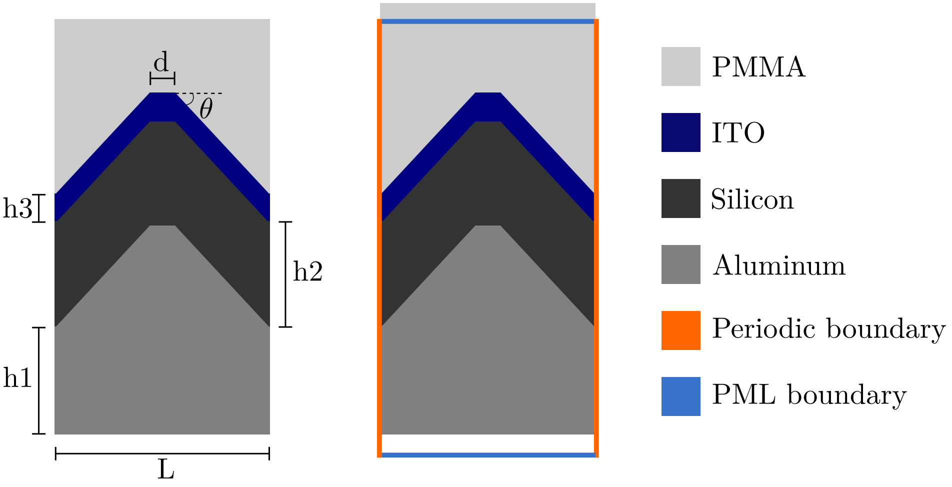

Figure 4.1. Modeling parameters and boundary conditions for the triangular structure.

calculate the IQE of the cell. Simulations were carried out in order to find the absorption in the Si layer and thereby determine the IQE of the cell for varying ITO ($h3$) and Si ($h2$) thickness and for varying period (L) and plateau width (d). The simulations were carried out for both s- and p-polarized light. For some simulations the results for s- and p-polarized light are compared, while an average of the two polarizations is shown in other cases.

The simulations for the triangular structures were based on the structure shown in Fig. 4.1 where the added layers are deposited ideally. Comparing Figs. 3.11 and 3.21 indicates that the depositions are not ideal as the surface appears more rounded after depositing 300 nm Si and 150 nm Al. Fig. 4.2 shows profiles from the AFM measurements for the imprints before and after deposition of Si and Al. It is seen that the profile after deposition becomes much wider as suspected from the AFM images. The structure without any layers also appears more rounded than the model used for simulations. Overall, the simulated model does not fit the actual imprinted samples and is therefore not expected to give exact fits if simulated and experimental results are compared.

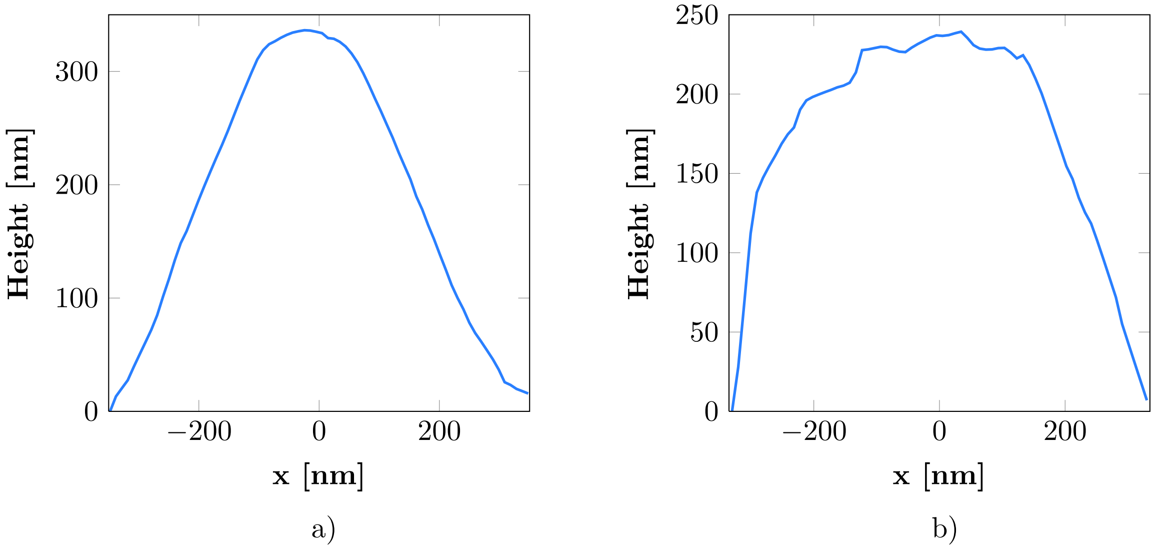

a)

b)

Figure 4.2. Profiles for imprints from etched c-Si master. a) Imprint with no layers deposited and b) imprint with 300 nm Si and Al.

4.2 Anodized structures

The anodized structures are arranged in a hexagonal pattern. *Lumerical* does however only support rectangular unit cells, which means that a larger unit cell is chosen in order to obtain a rectangular unit cell. The rectangular unit cell is shown in Fig. 4.3a.

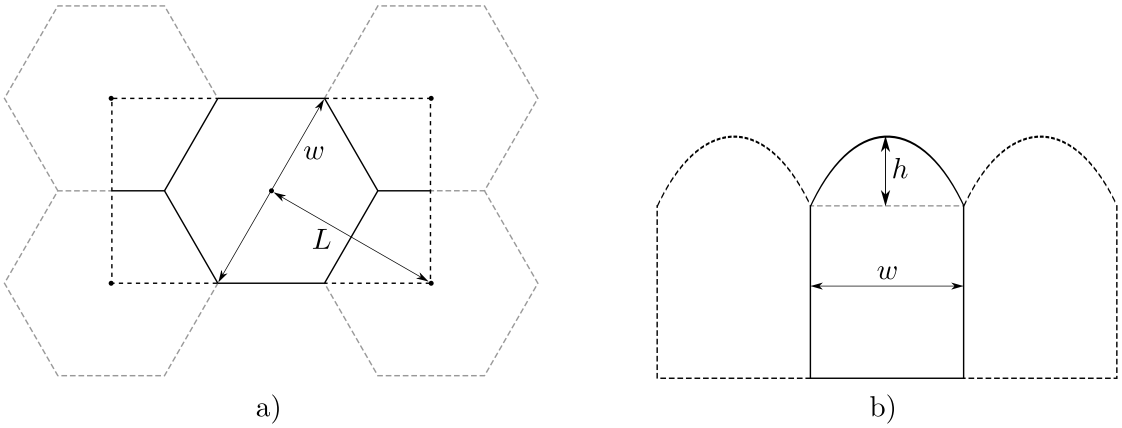

Figure 4.3. a) Hexagonal unit cell transformed into rectangular unit cell illustrated by black dashed lines. b) Side view of the structure. The figure is taken from an earlier project[14].

The AFM images shown in Chap. 3 and App. B reveal that the imprinted surfaces are rounded as shown in Fig. 4.3b and become flatter when ITO and Si layers are deposited. A model for mapping the surfaces of PA and CA1 imprints was made by making profiles across the hexagonal unit cells as shown in Fig. 4.4a. The profiles were obtained with the WSxM software for processing of SPM images[35] and resulted in profiles as illustrated in Fig. 4.4b.

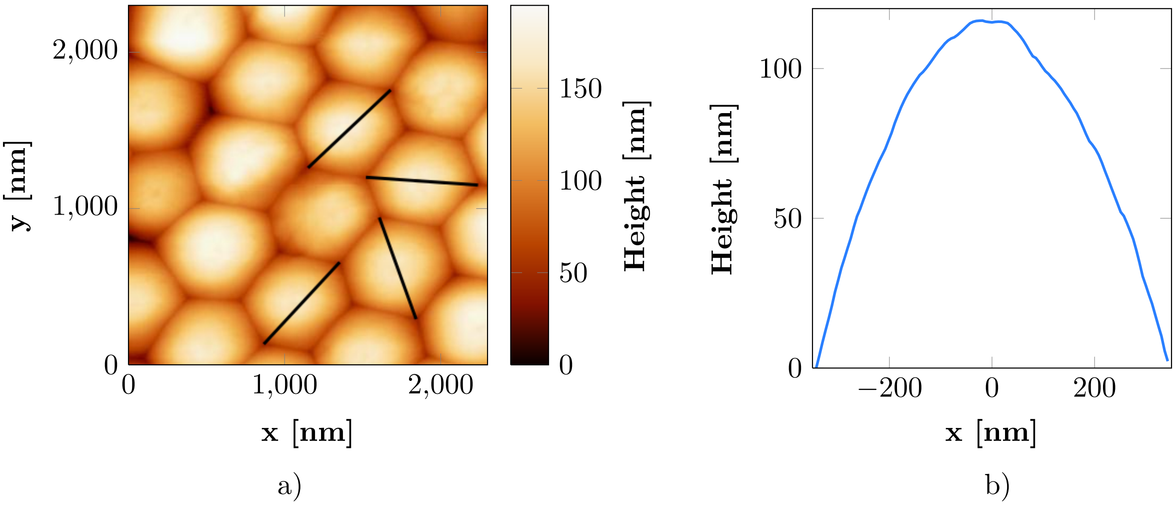

Figure 4.4. a) AFM image of CA1 imprint where black lines indicate the profiling method. b) Example of a profile from a CA1 surface.

Several profiles were acquired for the different surfaces and an average was taken for the profiles from a given surface in order to obtain models for how the surfaces change with varying ITO and Si thickness. The initial idea was to fit the profiles to third degree polynomials, but it was not possible to find a general model for the surface from these fits. Parabolic fits were instead chosen as they made it possible to find linear correlations between the surface profiles and the

ITO thickness. Fig. 4.5 shows the profile from Fig. 4.4 fitted to both a third degree polynomial and a parabola, where it is seen that the third degree polynomial fit describes the curvature of the profile best, while the parabola fits the height of the profile more accurately.

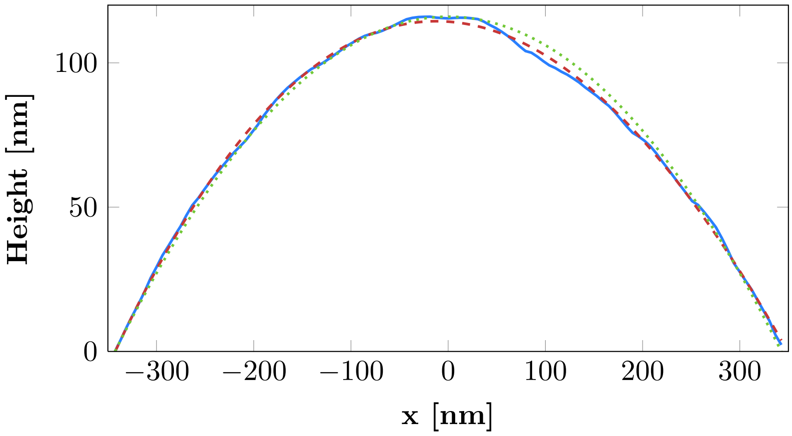

Figure 4.5. Fitting of profile from CA1 imprint. The solid line is the profile shown in Fig. 4.4b, the dashed line shows the profile fitted to a third degree polynomial, while the dotted line shows the profile fitted to a parabola.

Using a parabolic approximation to the profiles means that it is actually only the width and the height of the profile that is of interest. The height and width of the profiles is used to make paraboloids following

$$z(x,y) = -\frac{x^2+y^2}{a^2} \cdot h + h, \tag{4.2}$$

where h is the height of the profile and $a = w/2$ according to the notation used in Fig. 4.3. The fits for PA and CA1 imprints with no layers deposited are shown in Fig. 4.6, where the height is found to be 141 nm for PA imprints with no layers deposited and 233 nm for CA1 imprints. For PA samples a was found to be 243 nm on average, while it was 335 nm for CA1 samples, which corresponds to periods of ∼420 and ∼580 nm, respectively. Compared to the data shown in Tab. 2.1 the periods seems to be similar, while the height measured on the imprints is smaller than the indentation depth measured on the masters.

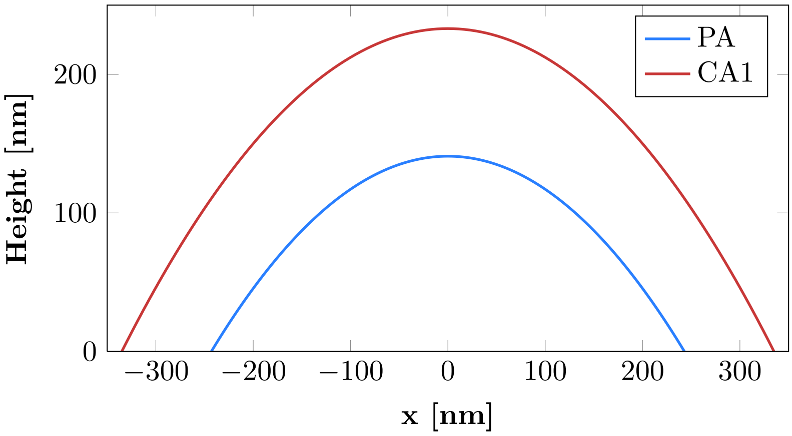

Figure 4.6. Parabolic fits to PA and CA1 imprints

The variation in height with respect to ITO thickness t was found for imprints before and after Si deposition. For PA imprints with ITO the height was found to vary as

$$h = -0.3489t + 143.95 \text{ nm}, \tag{4.3}$$

while it varied as

$$h = -0.2942t + 86.74 \text{ nm} \tag{4.4}$$

after deposition of 300 nm Si. For CA1 imprints the corresponding linear fits before and after Si deposition are

$$\begin{aligned} h &= -0.8384t + 241.12 \text{ nm}, && (4.5) \\ h &= -0.0268t + 106.66 \text{ nm}. && (4.6) \end{aligned}$$

The linear fits for height as function of ITO thickness are shown in Fig. 4.7, where it should be noted that the fit for PA imprints after deposition of Si is not a very good fit. AFM images of PA and CA1 imprints with varying Si thickness are shown in App. B. It was however not possible to obtain reasonable fits for making models of the change in height with respect to Si thickness from the AFM images that were acquired.

It was chosen not make a model for the surface after deposition of Al as there was no difference for the simulated absorption in the Si layer when using a flat Al back surface compared to using a microstructured Al back surface as shown in Fig. 4.8, which means that a flat Al back surface was used for the simulations.

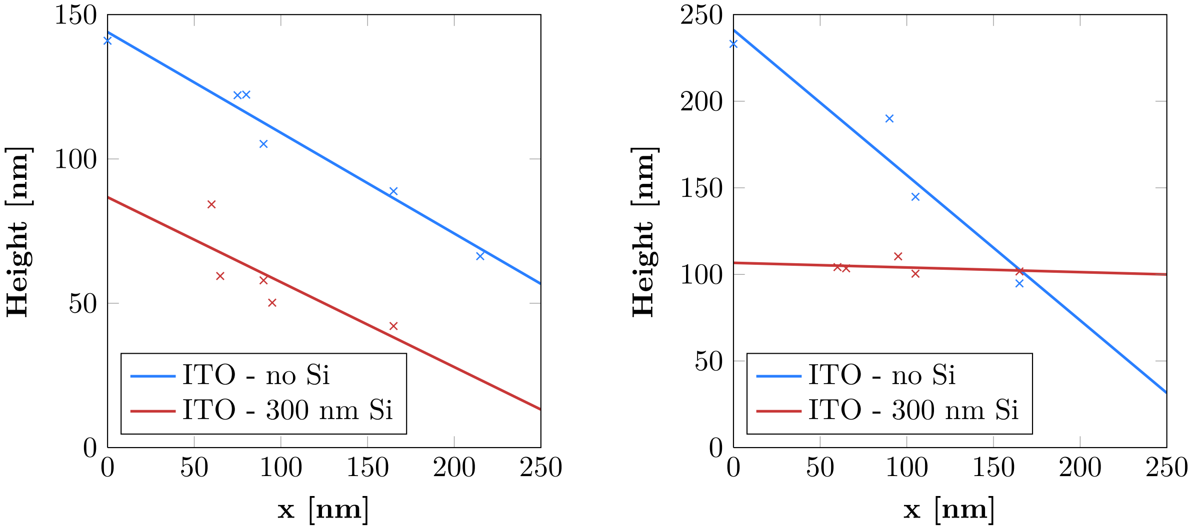

a) b)

Figure 4.7. Linear fits to the profile height with respect to ITO thickness when there is no Si deposited and with 300 nm Si. a) PA imprints and b) CA1 imprints. The crosses show the data points used for the fits.

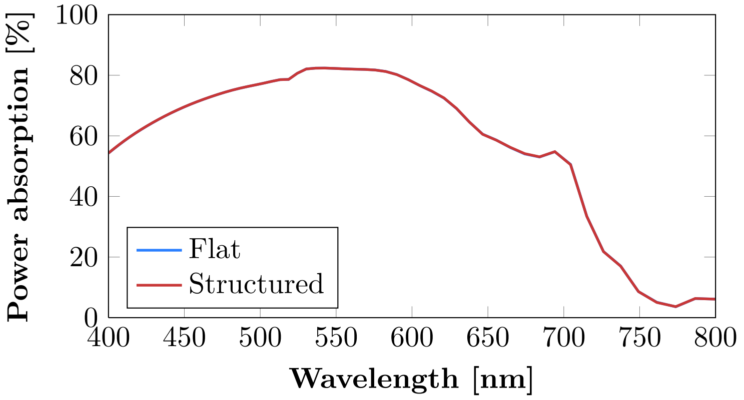

# **Back surface**	**IQE**
Flat	0.5744
Structured	0.5744

Figure 4.8. Absorption in Si with respect to wavelength and the corresponding IQE for a flat and a structured Al back surface with the Al thickness set to 100 nm. The two plots are on top of each other.

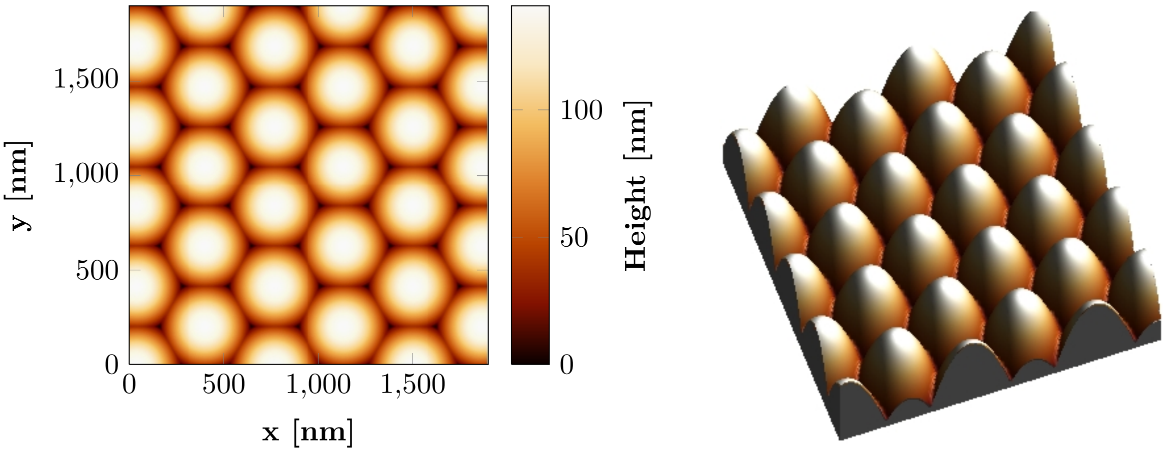

Figure 4.9. Fitted PA imprint.

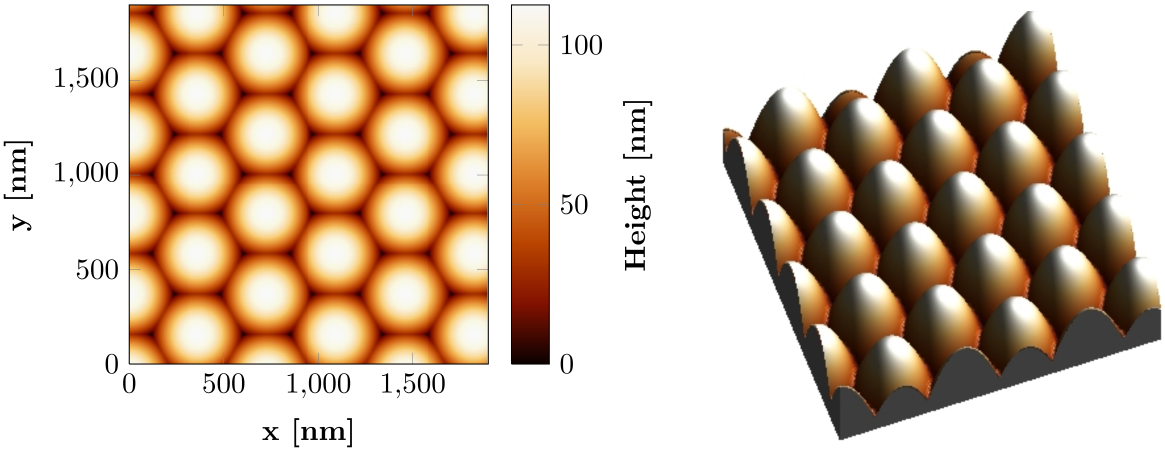

Figure 4.10. Fitted PA imprint with 90 nm ITO.

Figs. 4.9–4.14 show some fitted PA and CA1 surfaces. When loading the surfaces in *Lumerical* the surfaces were displaced such that the volume between two microstructured surfaces corresponds to the volume of depositing a flat layer on a planar surface.

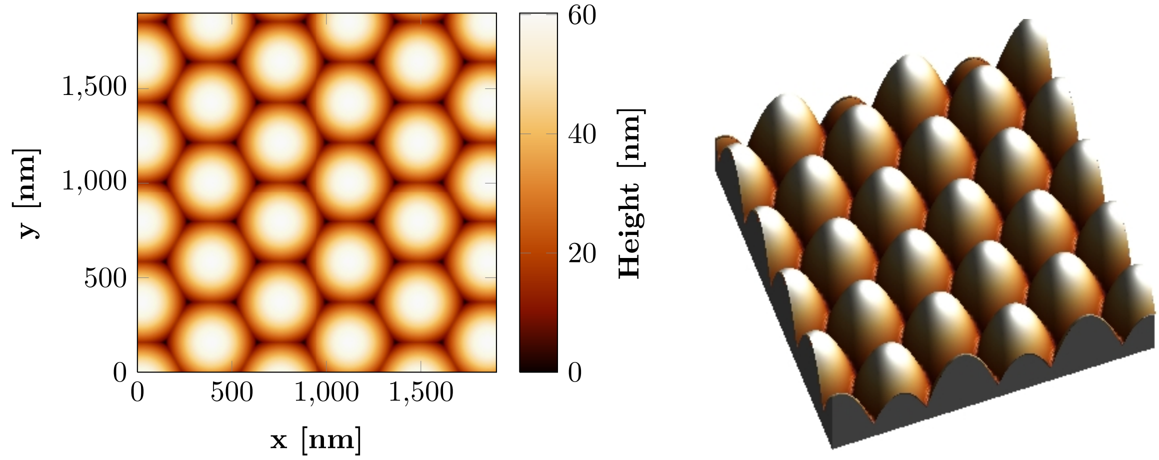

Figure 4.11. Fitted PA imprint with 90 nm ITO and 300 nm ITO.

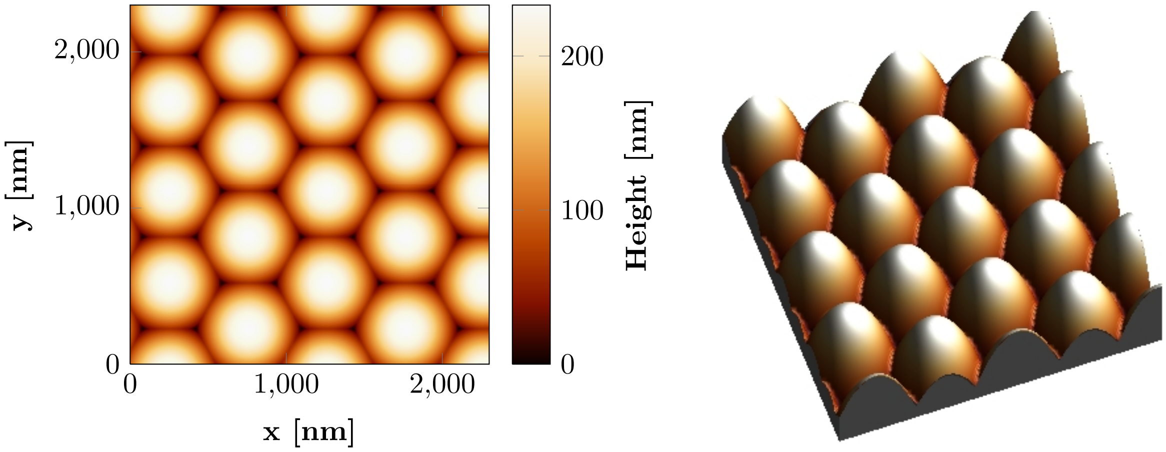

Figure 4.12. Fitted CA1 imprint.

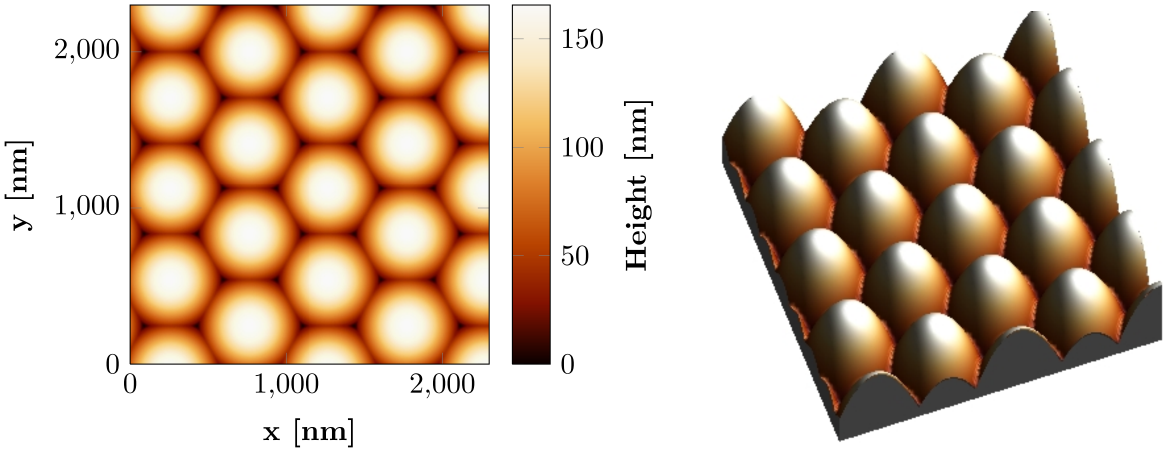

Figure 4.13. Fitted CA1 imprint with 90 nm ITO.

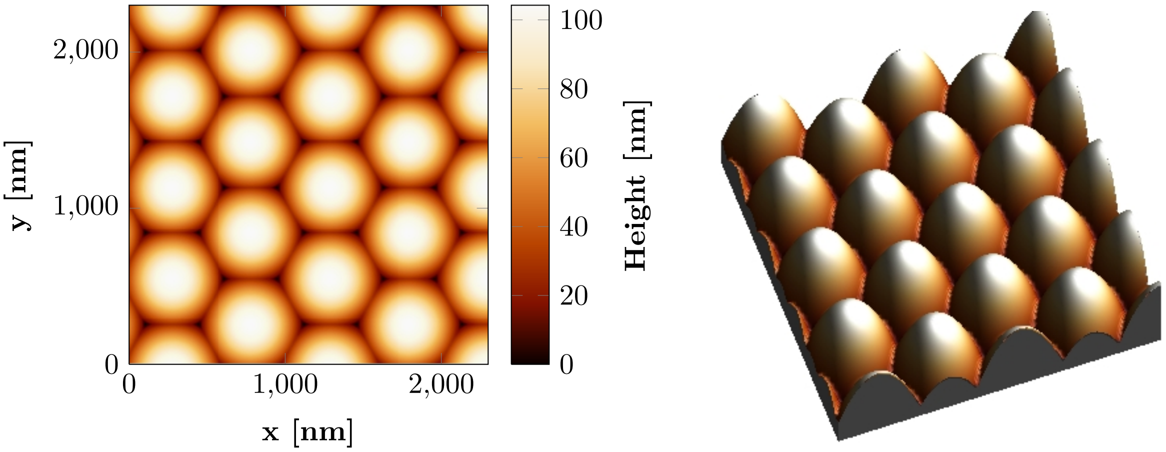

Figure 4.14. Fitted CA1 imprint with 90 nm ITO and 300 nm ITO.

The simulations for the anodized structures requires a 3D simulation cell in *Lumerical*, which was set up with the boundary conditions shown in Fig. 4.15. The bottom boundary was generally set as a metal boundary as described in App. D. However, some simulations were run without the Al layer in order to simulate reflection and transmission for such a structure for comparison with experimental results. In such cases, the bottom boundary was set up as a PML boundary in order not to reflect the transmitted light back through the transmission monitor and into the structure.

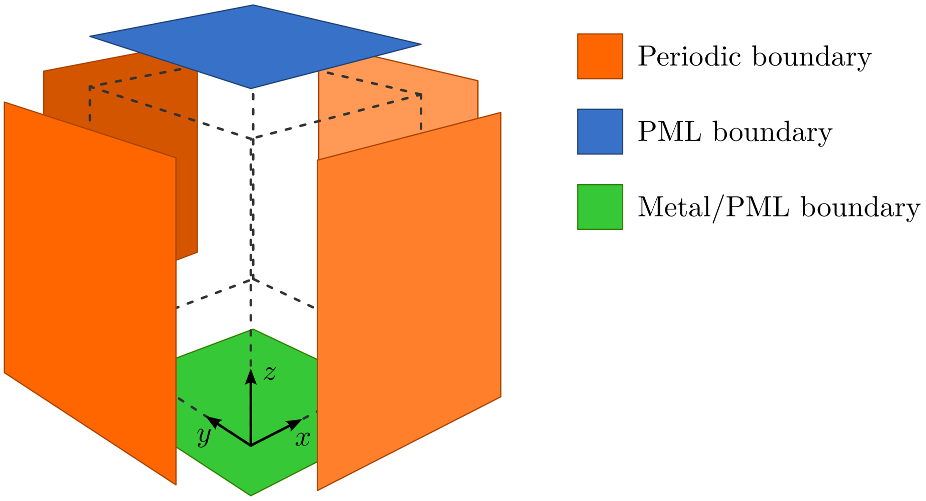

Figure 4.15. Boundary conditions for the anodized structure. The figure is taken from an earlier project[14].

The boundary above the structure and the light source were again positioned inside the PMMA layer and simulations were again only carried out for normally incident light. For a periodic structure as the anodized structure there is no difference between using *s*- or *p*-polarized light for normal incidence. All simulation were therefore only run for *p*-polarized light.

Chapter 5

Simulated results

Simulations of the optical properties of imprints with ITO, Si and Al layers were simulated using *Lumerical FDTD Solutions*. The simulated results obtained for the absorption, reflection and transmission of such structures will be presented here.

The simulations were carried out with the light source and reflection monitor placed inside the PMMA layer, which means that the simulated reflection does not correspond to the reflection measured in the experiments. This error is decreased by considering the reflection and transmission at an air/PMMA interface and the interface between PMMA and the following layers as shown in Fig. 5.1, where ρ_0 and τ_0 are the reflection and transmission coefficients for the air/PMMA interface and ρ_1 is the reflection coefficient for the interface between PMMA and the following layers. If internal reflections in the PMMA layer are considered and all internal reflections deeper inside the structure are ignored, the reflection in the air based on ρ_0 and ρ_1 is

$$R = \frac{\rho_0 + \rho_1 - 2\rho_0\rho_1}{1 - \rho_0\rho_1}, \tag{5.1}$$

where ρ_1 is the reflection obtained by the simulations and ρ_0 is found from the intensity of light inside a PMMA layer for a light source positioned in air that was used initially in the simulations. The reflection shown in all simulated reflection plots is the reflection R from Eq. 5.1. The simulated reflection measurements shown for the imprints for the etched c-Si samples are averages of the *s*- and *p*-polarization.

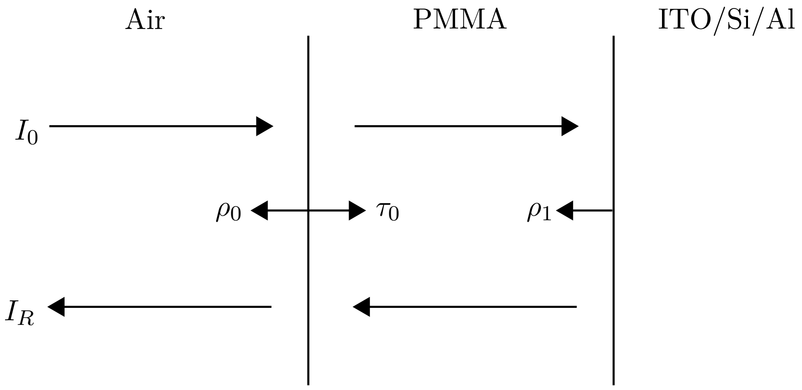

Figure 5.1. Reflection and transmission at the air/PMMA interface and reflection at the PMMA/ITO interface.

The measured reflection from flat PMMA samples with varying ITO thickness, 300 nm Si and Al was shown in Fig. 3.24. The simulated reflection from planar surfaces with similar layers is shown in Fig. 5.2 together with the measured data. The shape of the simulated reflection is somewhat similar to the measured data, but the peaks and valleys are shifted to higher wavelengths for the sample with no ITO, while the simulated reflection is higher than the measured reflection for the samples with ITO.

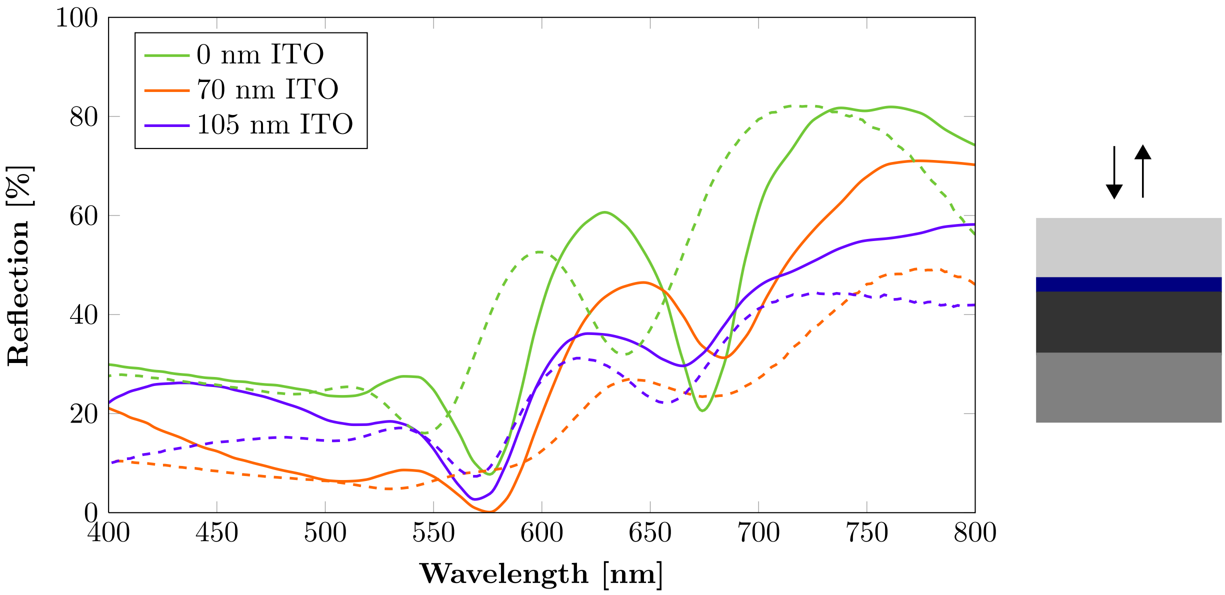

Figure 5.2. Reflection from flat PMMA samples with varying ITO thickness, 300 nm Si and Al. Solid lines show simulated reflection and dashed lines are measured data.

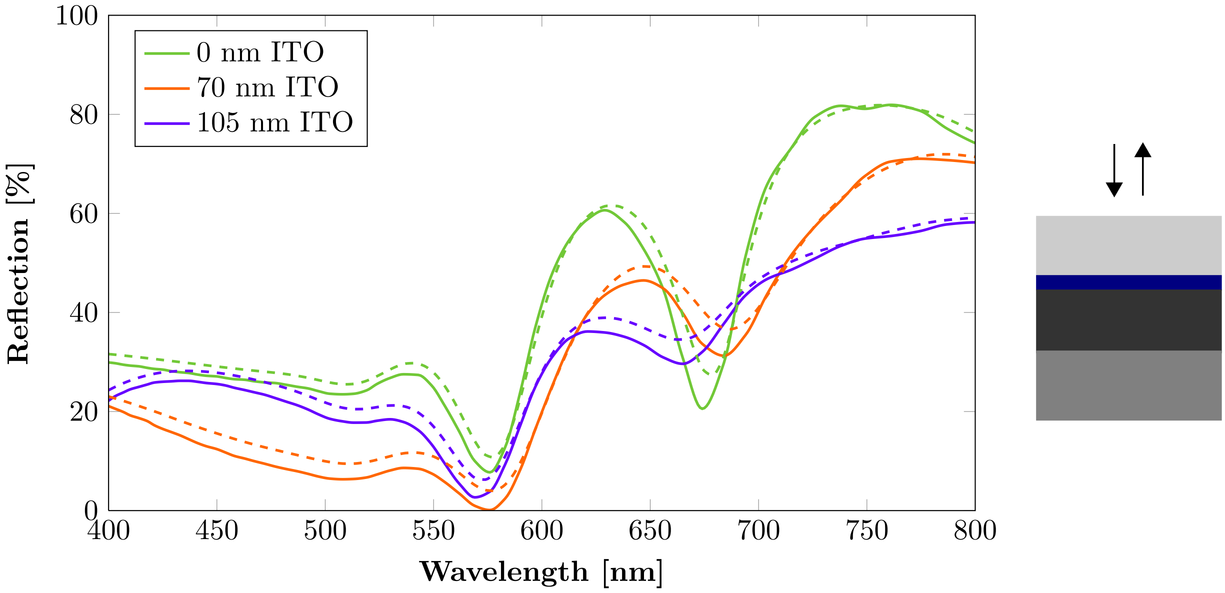

Figure 5.3. Reflection from flat PMMA samples with varying ITO thickness, 300 nm Si and Al. Solid lines show reflection simulated with *Lumerical* and dashed lines show the reflection calculated with the stack matrix method.

The reflection shown in Fig. 5.2 from planar PMMA samples with varying ITO thickness, 300 nm Si and Al simulated with *Lumerical* is compared to the reflection calculated using the stack matrix method[36] in Fig. 5.3. The results from the simulations and calculations follow each other, but the reflection found with the stack matrix method is generally slightly larger. The valleys from the simulations carried out with *Lumerical* are also deeper compared to the calculated reflection, which shows that the results from *Lumerical* may not be completely accurate, but they will still show realistic results.

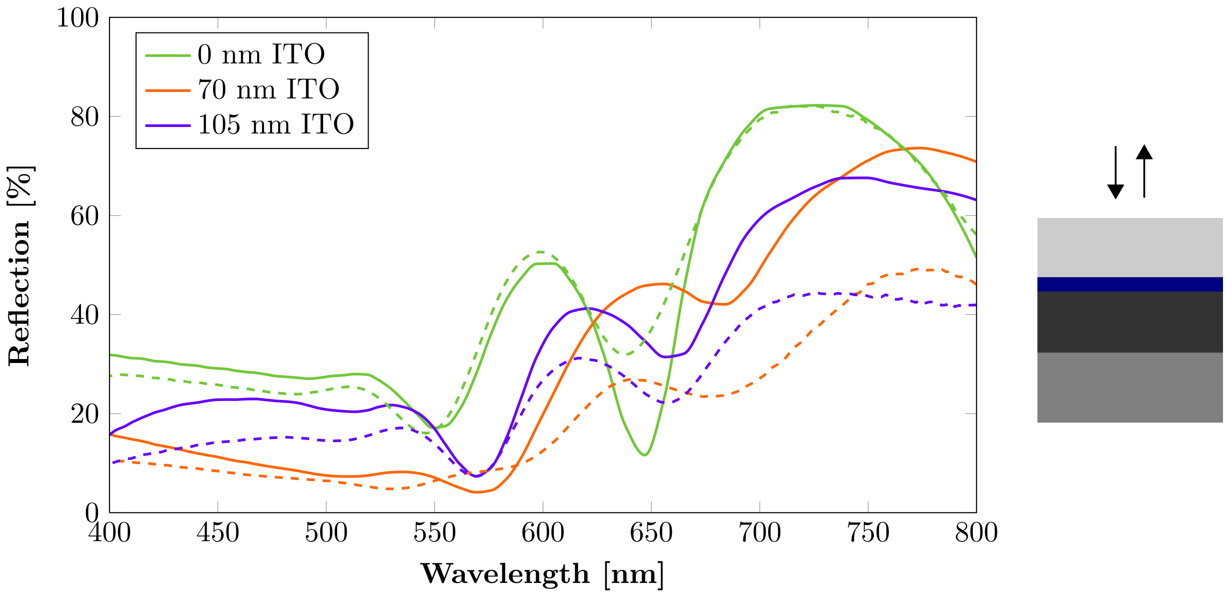

Figure 5.4. Reflection from flat PMMA samples with varying ITO thickness, 300 nm Si and Al. Solid lines show simulated reflection and dashed lines are measured data. The Si thickness is only 280 nm for the simulation with no ITO, while the refractive index for ITO has been changed for the simulations with ITO.

Fig. 5.4 also compares the measured reflection from flat PMMA samples shown in Fig. 3.24 with simulated results. However, the simulations has been changed such that a 280 nm Si layer is used for the simulation with no ITO, while the refractive index index for ITO has been changed for the simulations with ITO that are still carried out with 300 nm Si. The simulation for a planar PMMA surface without ITO is close to the measured data except for the larger drop in reflection for the simulation at ~640 nm. This indicates that the refractive index obtained for the Si layer is a valid fit and that the Si deposition was not completely uniform as mentioned in Sec. 2.4.
For the simulations with ITO, the refractive index for ITO was changed. The refractive index for ITO used for simulating the reflection in Fig. 5.2 was an average of refractive indices obtained from many different ITO samples. In Fig. 5.4 the refractive index used for the simulation with 70 nm ITO was acquired from a deposition of 70 nm ITO on a c-Si wafer, while the simulation with 105 nm ITO used a refractive index for ITO acquired from a deposition of 105 nm ITO on a c-Si wafer. In both cases it is seen that the peaks and valleys fits better in Fig. 5.4 than in Fig. 5.2 and that the simulated and measured reflections are more similar at wavelengths from 400–600 nm. However, the simulated reflection is increased for larger wavelengths when doing the same comparison, which indicates that there are some issues with the refractive index obtained for ITO.

It was seen in Chap. 4 that the surface of the imprints based on the etched c-Si master were not close to being ideal as the triangular structure used for simulations. The model made for the PA and CA1 imprints was based on measured data, but the model is still very ideal compared to the SEM images shown in Chap. 3 where it is seen that there is no long range ordering of the surfaces. This means that the simulated results are not expected to exactly fit the measured reflection and transmission. The simulated results being presented do therefore not represent the measurements, but they should still give some indications about how light interacts with the different structures.

5.1 Triangular structure

The simulated reflection for a triangular structure with a period of 700 nm and a plateau width of 50 nm with varying ITO thickness, 300 nm Si, and Al is shown in Fig. 5.5. It is seen that the simulated reflection increases significantly when the wavelength is ∼600 nm, where the extinction coefficient for Si almost reaches zero. The measured data is shown for comparison and it is seen that the simulations for the ideal structure fit the measured data reasonably for wavelengths below 600 nm, while the difference is rather big above 600 nm.

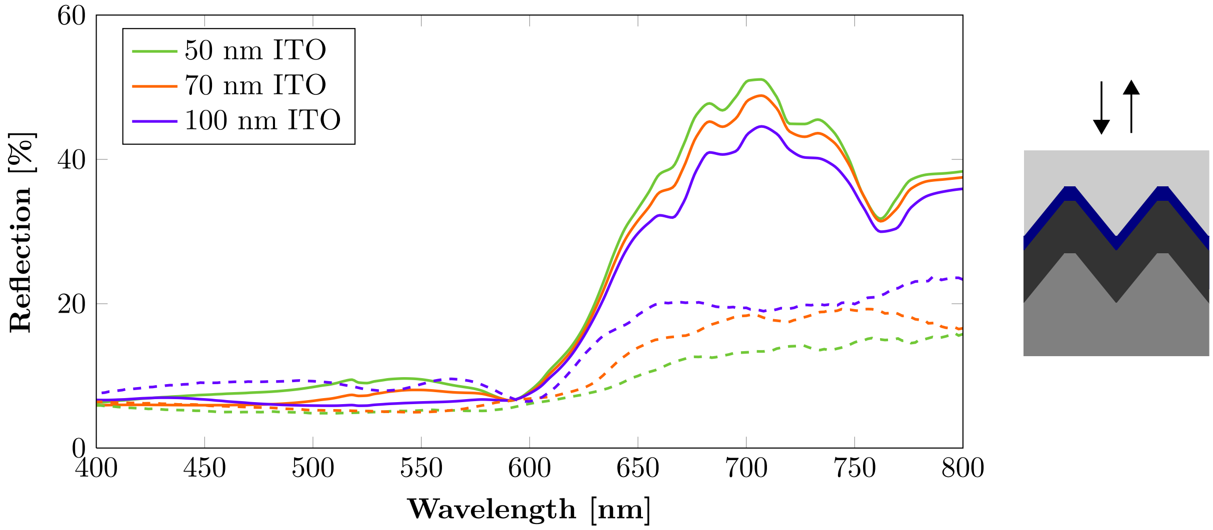

Figure 5.5. Reflection from imprints from etched c-Si master with varying ITO thickness, 300 nm Si and Al. The period was 700 nm and the plateau width was 50 nm. Solid lines are simulated results while dashed lines are measured data for comparison.

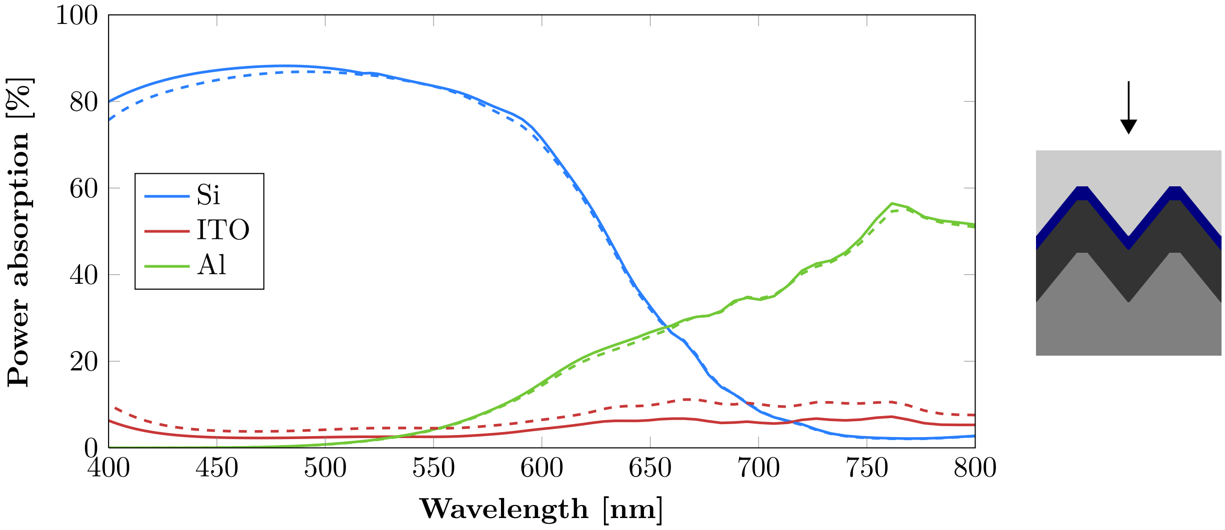

Figure 5.6. Absorption in different layers with respect to wavelength for triangular structures with a period of 700 nm and plateau width set to 50 nm with 300 nm Si and Al. The solid line is with 70 nm ITO and the dashed line is with 100 nm ITO.

The absorption in the ITO, Si, and Al layer, respectively, is shown in Fig. 5.6 for the triangular structure for different ITO thicknesses. It is seen that the thicker ITO layer absorbs more light and that the Al layer starts absorbing light with wavelengths above 500 nm and ends with absorbing over 50% for wavelengths above 750 nm.

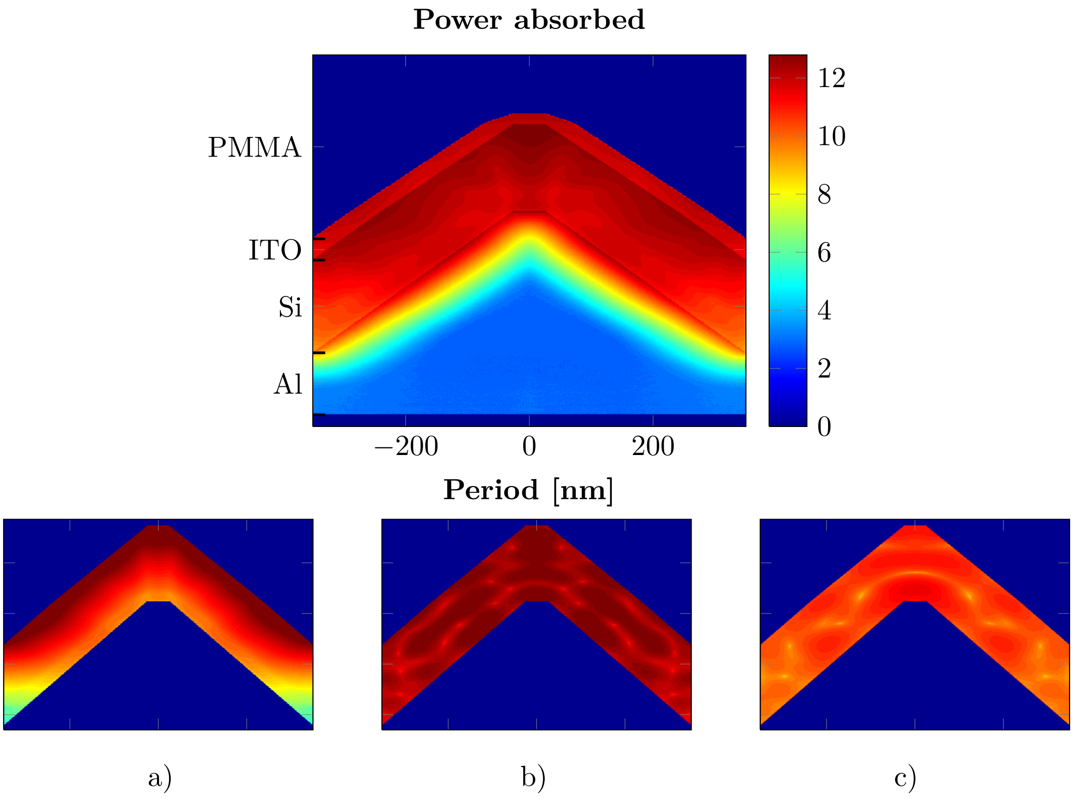

Figure 5.7. Simulated absorption for triangular structure with 70 nm ITO, 300 nm Si, and Al where the period is 700 nm and the plateau width is set to 50 nm. The top image shows the average absorption in the structure for wavelengths from 400–800 nm, while the bottom images show the absorption in the Si layer for different wavelengths. a) 400 nm, b) 600 nm, and c) 800 nm. The scale bar is logarithmic and shows the power per unit area.

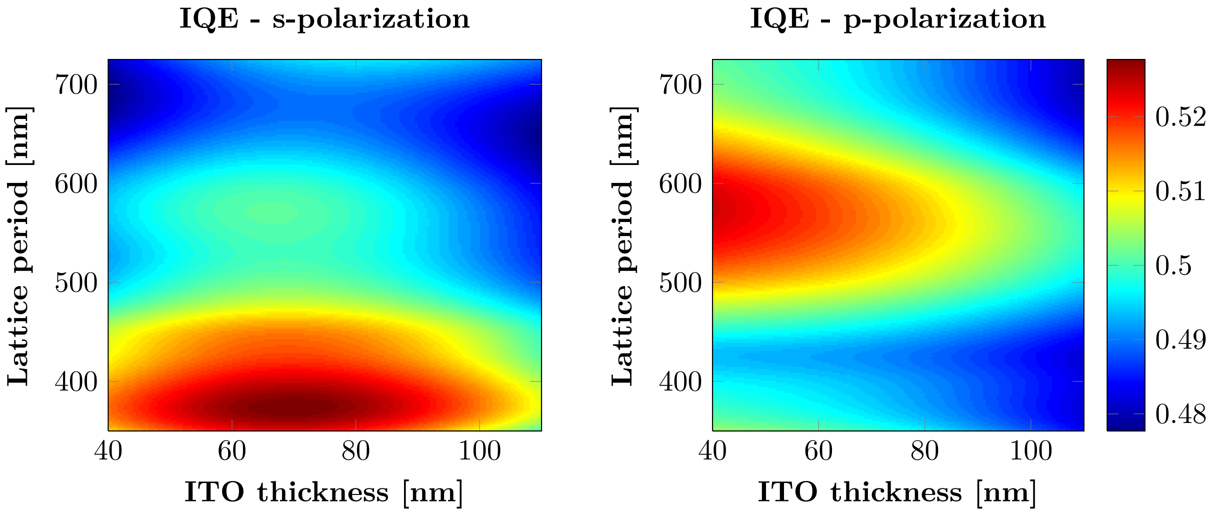

Figure 5.8. IQE for triangular structure with 300 nm Si and a plateau width of 50 nm. The scale bar is the same for both plots.

A 2D view of the simulated absorption is shown in Fig. 5.7. It is seen that the area with the highest absorption is just inside the peak of the Si layer. It also shows that the absorption is almost uniform across the ITO layer, while the intensity of light that enters the Al layer decreases rather quickly. It is further seen that the light with a wavelength of 400 nm is absorbed quickly in the Si layer, while the absorption is high and uniform for a wavelength of 600 nm and is low and uniform for a wavelength of 800 nm.

The simulated absorption in a Si layer with a thickness of 300 nm for the triangular structure was obtained for varying ITO thickness and lattice period. Fig. 5.8 shows the IQE with respect to ITO thickness and lattice period. It is seen that the structures have the highest IQE when the ITO thickness is between 70–80 nm for s-polarized light, while the IQE increases with decreasing ITO thickness for p-polarized light. For the lattice period it is seen that the optimum lattice period is smaller for s-polarized light compared to p-polarization.

5.2 Anodized structures

Simulations were carried out for models of PA and CA1 imprints. The IQE for varying ITO thickness for imprints with 300 nm Si and Al is shown in Fig. 5.9. It is seen that the IQE is generally higher for PA imprints compared to CA1 imprints. The IQE is highest for both PA and CA1 imprints when the ITO thickness is ~55 nm, but there is no big variation in the IQE for the imprints when the ITO layer is less than 80 nm, which indicates that the microstructured surface replaces the effect of the antireflective coating.

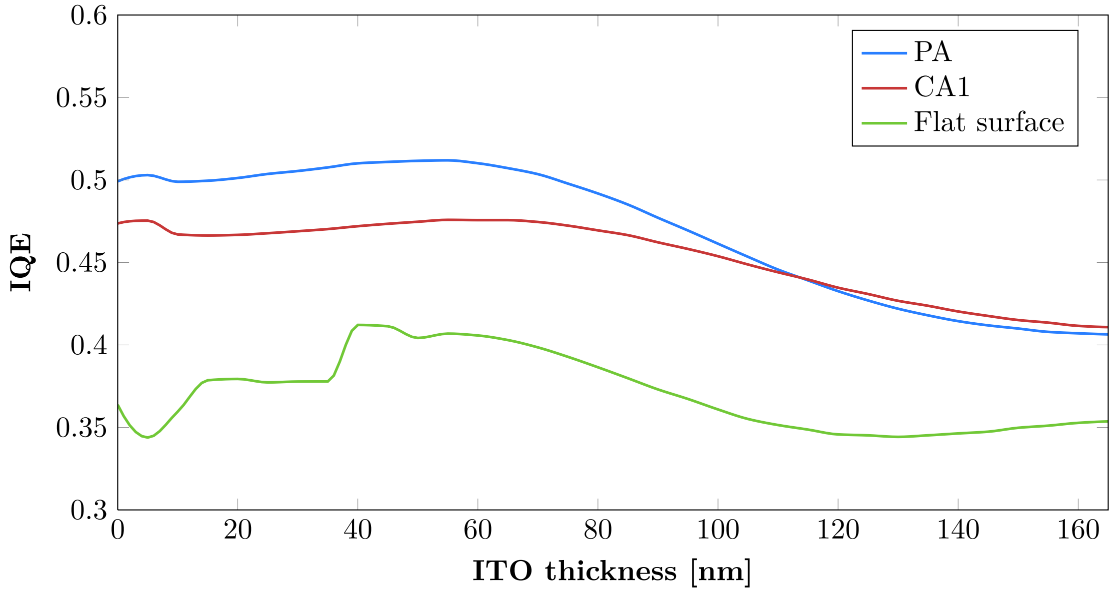

Figure 5.9. IQE for PA and CA1 imprints with varying ITO thickness, 300 nm Si and Al. The IQE for a flat surface with the same layers is shown for comparison.

The simulated reflection from PA and CA1 imprints with 300 nm Si and Al and with perfect hexagonal ordering is shown in Figs. 5.10 and 5.11. The reflection decreases with increasing ITO thickness for both structures and it is seen that there is a large peak in the reflection for both structures at ∼730 nm. The simulations does not fit the measured reflection, which is assumed to be due to the fact that the synthesized imprints are not close to having the perfect hexagonal ordering of the simulation model.

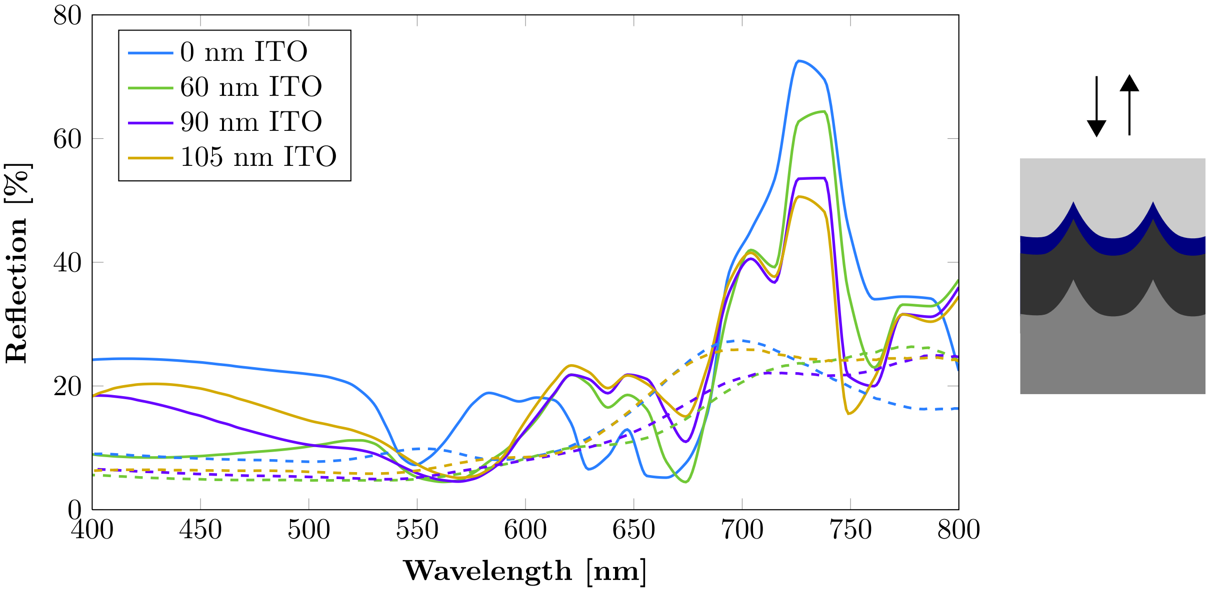

Figure 5.10. Reflection from PA imprints with varying ITO thickness, 300 nm Si and Al. Solid lines are simulated results while dashed lines are measured data for comparison.

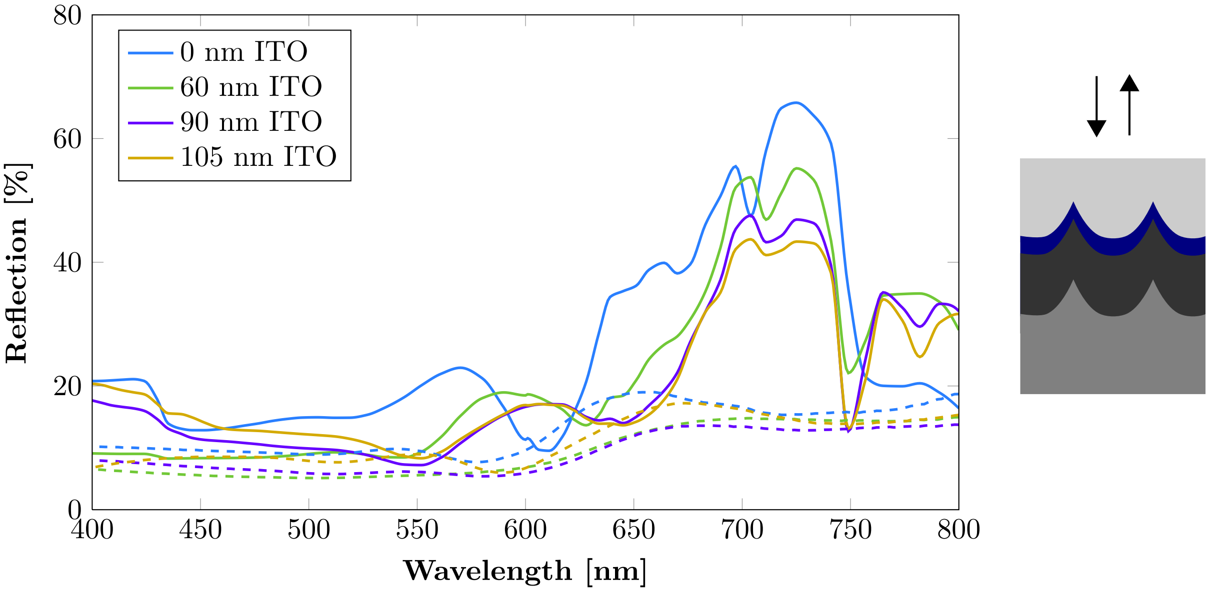

Figure 5.11. Simulated reflection from CA1 imprints with varying ITO thickness and 300 nm Si. Solid lines are simulated results while dashed lines are measured data for comparison.

The simulated absorption in the different layers for PA and CA1 imprints is shown in Figs. 5.12 and 5.13. The tendency is the same as for the triangular structure, where the absorption in Al reaches ∼50% at high wavelengths and the absorption in the ITO layer increases with increasing ITO thickness. It is also seen that the lower IQE for the CA1 samples compared to PA samples is due to lower absorption in the Si layer for light with wavelengths above 550 nm.

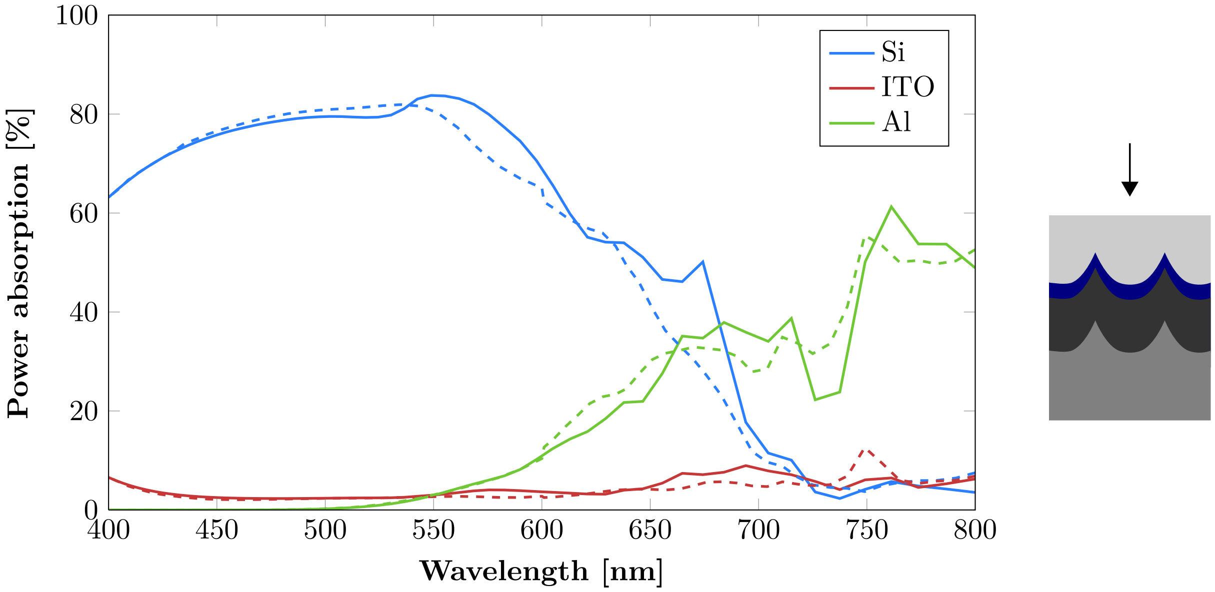

Figure 5.12. Absorption in Si, ITO and Al from imprints with 60 nm ITO, 300 nm Si, and Al. Solid lines show absorption for PA imprints, while dashed lines represent absorption for CA1 imprints.

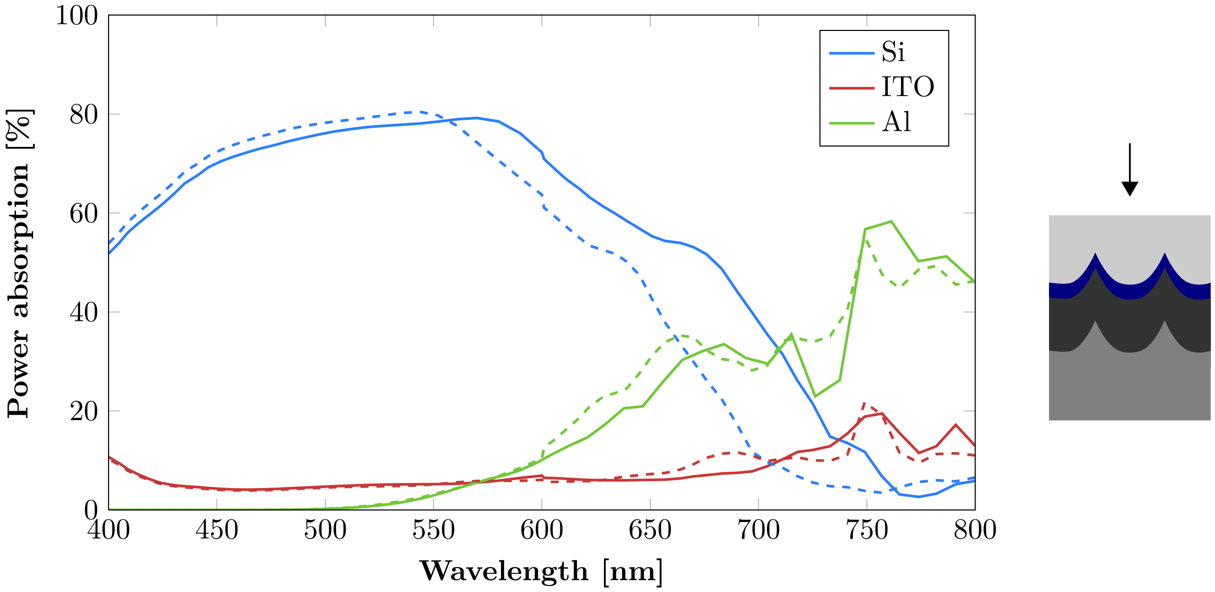

Figure 5.13. Absorption in Si, ITO and Al from imprints with 90 nm ITO, 300 nm Si, and Al. Solid lines show absorption for PA imprints, while dashed lines represent absorption for CA1 imprints.

Fig. 5.14 presents a 2D view of the simulated absorption in a PA imprint with 60 nm ITO, 300 nm Si, and Al. The figure shows a cut down through the structure across the blue line shown in Fig. 5.15. The highest absorption occurs in the first few nanometers of the Si layer, which is a result of the high absorption of light with low wavelengths in Si. It is obvious that the absorption follows the extinction coefficients of the different layers shown in App. E with an almost constant absorption in ITO, an increasing absorption in Al with increasing wavelength and a decreasing absorption in Si with increasing wavelength, where most of the 400 nm light is absorbed immediately in the Si, while the light is absorbed in most of the structure at 600 nm and the absorption is low at 800 nm.

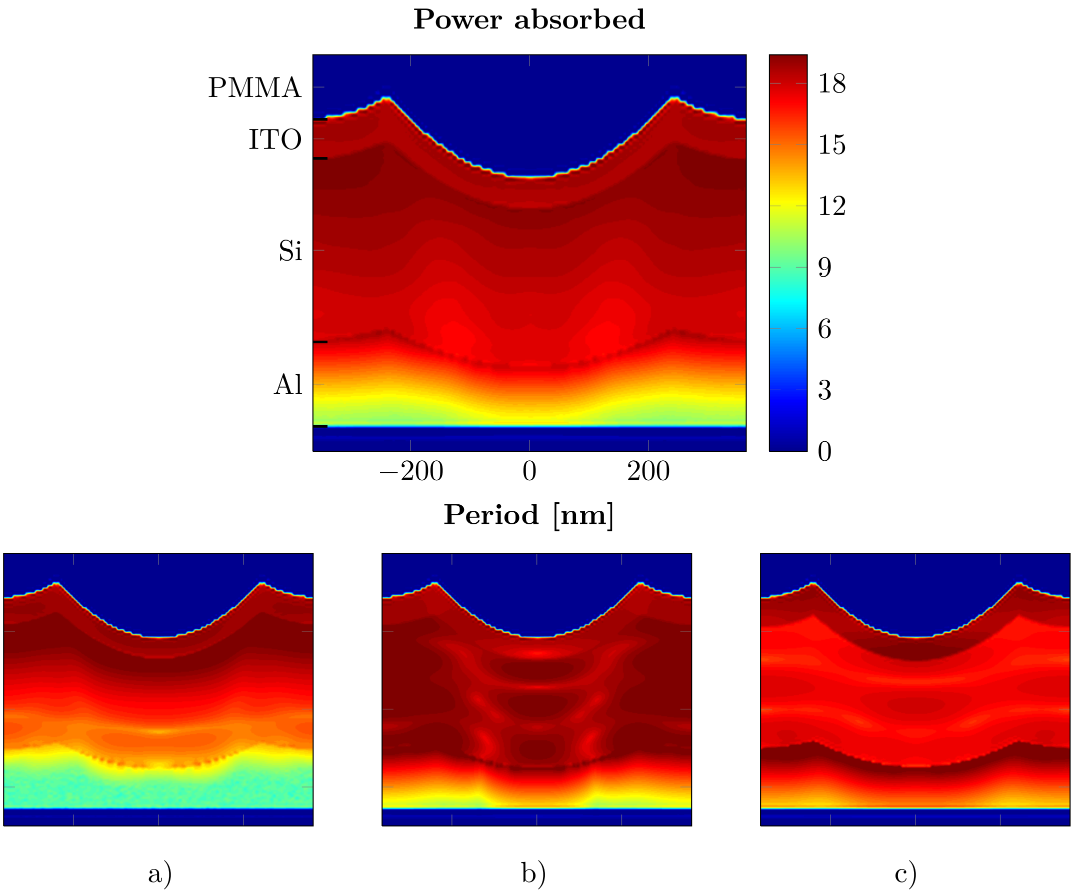

a) b) c)

Figure 5.14. Simulated absorption for PA imprint with 60 nm ITO, 300 nm a-Si, and Al. The top image shows the average absorption in the structure for wavelengths from 400–800 nm, while the bottom images show the absorption for specific wavelengths. a) 400 nm, b) 600 nm, and c) 800 nm. The scale bar is logarithmic and shows the power per unit area.

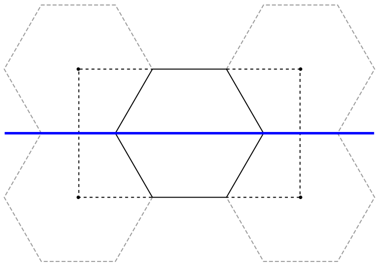

Figure 5.15. The 2D view of the absorption shown in Fig. 5.14 is taken across the axis marked by the blue line.

Chapter 6

Discussion

This chapter will discuss the synthesis and characterization of imprinted structures with ITO, Si, and Al deposited. The reflection and transmission measurements will be discussed and compared for the different structures. Finally, the simulated results will be discussed.

6.1 Synthesis of imprinted substrates

It was seen in Chap. 3 that the imprinting process transferred the microstructure from the master to the PMMA substrates with a good accuracy. The imprinting process had a high reproducibility and only one master of each type was used during the project period. The masters were examined in a SEM before the imprinting process was initiated and again later during the project period. Fig. 6.1 shows a comparison of SEM images of the PA master before imprinting and late in the project period. There is no apparent difference in the appearance of the master before and after imprinting. Due to the reproducibility of the imprints and the low degree of wear of the master, the imprinting of anodized patterns in PMMA could be viable for larger scale roll-to-roll processing. Lee et al.[37] have shown a working setup for a roll-to-roll anodization process, which means that it should be possible to synthesize large-area anodized master for a roll-to-roll imprinting process.

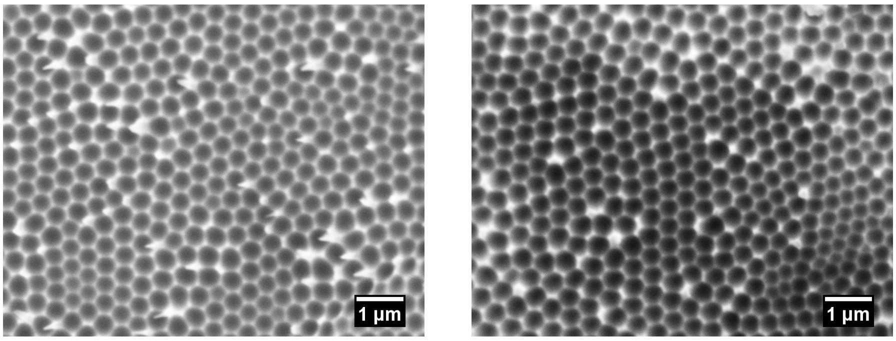

a) b)

Figure 6.1. SEM images of PA master. a) Before imprinting and b) late in the project period.

Solar cell layers were deposited on the imprinted substrates. An ITO layer was deposited as a transparent front contact with antireflective properties. The minimum sheet resistance achieved for a 100 nm ITO layer was ∼60 Ω/□. There were however big fluctuations in the sheet resistance and transparency of the deposited ITO layers, which could be caused by cross-contamination as the Cryofox Explorer coater is a generic unit for e-beam sputtering and DC/RF sputtering. The different targets in the coater are protected by shutters, but the shutters are not tight-fitting.

According to the literature, the transparency and sheet resistance may be improved by adding oxygen during deposition[19,38] or by heating the substrate[19,38,39]. Adding oxygen in the desired quantities during deposition would require changing the master controller for the oxygen flow, while a post-deposition annealing at temperatures of 300–350°C would require a change of substrate material due to the low melting temperature for PMMA. It has been reported that the sheet resistance can be decreases by ∼35 % by heating the substrate to 70°C during deposition[18]. The deposition on a heated substrate was carried out with a high RF power of 340 W, which is significantly above the ∼45 W currently used for ITO deposition, but heating the substrate during deposition could presumably also be beneficial at lower power.

Deposition of Si was done by PECVD. The refractive index of the deposited Si is shown in Fig. E.2 in App. E, where it is seen that the extinction coefficient is lower than for a Si deposition carried out at a higher temperature during an earlier project[14]. Fig. 6.2 shows the amount of photons from the AM1.5 spectrum that are absorbed in Si with respect to the depth the photons travel through the layer. It is seen that photons are able to travel significantly further into a layer with the Si deposited at low temperature when comparing to a similar calculation with the refractive index from Palik[32]. At normal incidence, a Si layer with a thickness of 300 nm and a perfectly reflecting back surface will only absorb ∼70% of the photons with an energy below the bandgap of a-Si. This shows that the deposition of Si must be improved.
Optimizing the low temperature PECVD deposition of Si did however prove troublesome as described in App. A. When adding a hydrogen flow, the showerhead pattern was transferred to the sample or the plasma would not ignite, unless the flow and pressure were very low. The addition of a hydrogen flow is usually part of depositing an a-Si layer of good quality as it reduces the effect of dangling bonds[40,41]. Additionally, a post-deposition annealing should improve the quality of the Si layer and increase the carrier density[42–44], which is not possible due to the low melting temperature of PMMA. Generally, the low temperature deposition of a-Si needs to be improved further and also needs to be able to deposit uniform layers of Si across several samples at the same time.

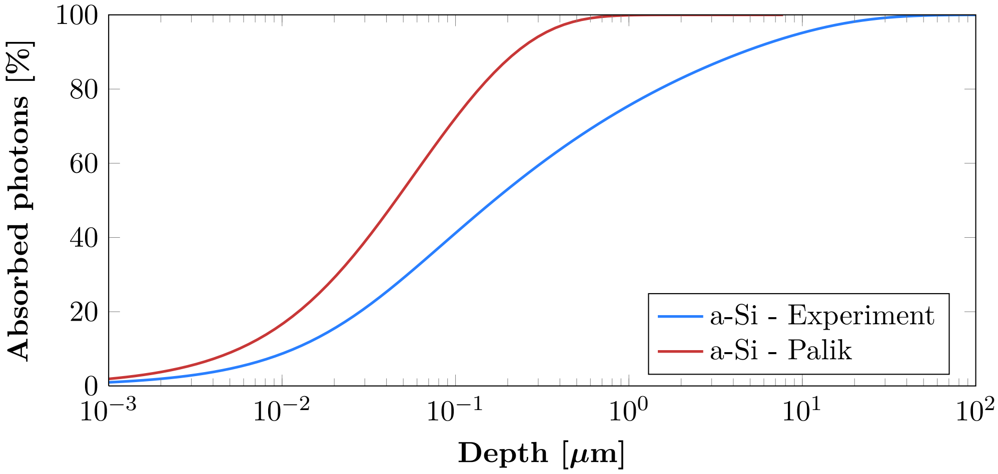

Figure 6.2. Amount of photons from the AM1.5 spectrum with energies above the band gap absorbed with respect to the depth the photons have traveled through Si.

The PMMA substrate is relatively cheap, has a good mechanical strength and is easy to handle. The low glass transition temperature of PMMA means that the process of heating the substrate, imprinting, and cooling can be carried out rather quickly. The low melting point is however also a big drawback when trying to improve the quality of the deposited ITO, Si, and Al layers. All three layers would benefit from annealing processes, which are however not possible due to the low melting temperature of PMMA.

Alternatives such as cyclic olefin copolymer (COC) glass from TOPAS[45] or flourinated ethylene propylene (FEP) glass from DuPont[46] and R J Chase[47] could be tested. The FEP glass can be acquired with a glass transition temperature of ∼200°C, while COC glass with a glass transition temperature of ∼180°C can be found. The FEP glass has optical properties that are similar to PMMA, while the COC glass adds transparency down to ∼300 nm light compared to ∼400 nm for PMMA and FEP glass.

6.2 Reflection and transmission measurements

The transmission measurements for the anodized imprints presented in Fig. 3.27 show that the scattered transmission for CA1 and CA2 imprints is much larger than for OA and PA imprints, which corresponds well with the fact that the CA1 master exhibits a higher diffuse reflection compared to the OA and PA masters[13].

The reflection from the different imprints with 300 nm Si and Al is shown in Fig. 6.3. It is seen that the microstructures decreases the reflection significantly without the use of an antireflective coating. The CA1 imprint has the lowest solar reflectance of 0.131 followed by the PA and c-Si imprints.

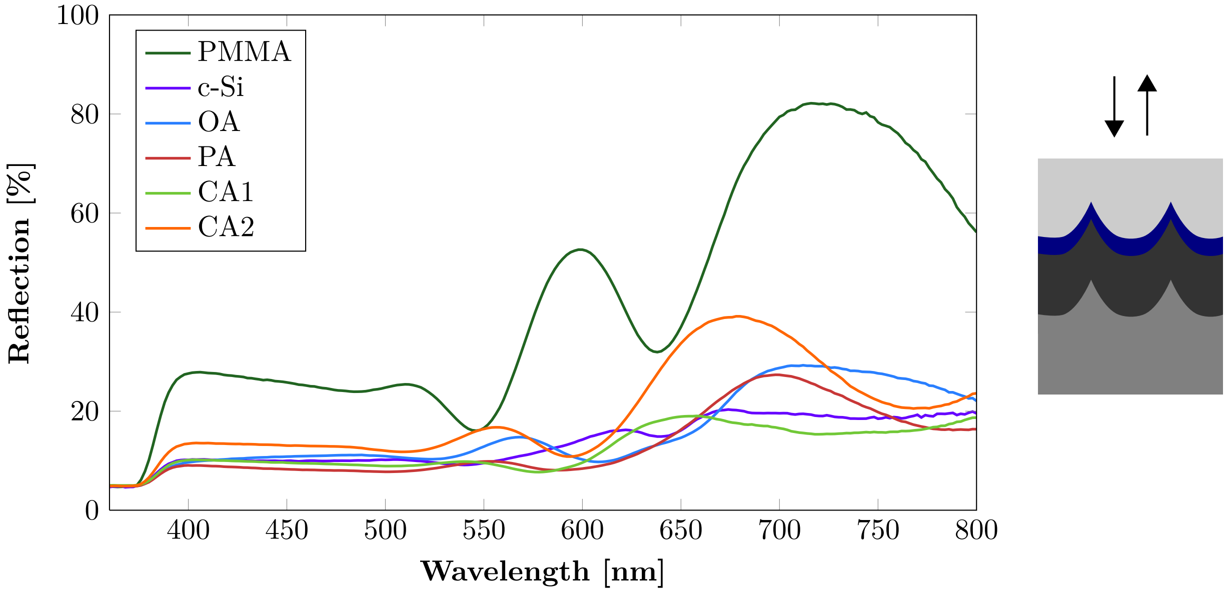

Figure 6.3. Reflection from imprints with 300 nm Si and Al.

The reflection for the imprints based on the etched c-Si master was decreased further by adding an antireflective ITO layer. The lowest solar reflectance of 0.090 was obtained for an imprint with 50 nm ITO, 300 nm Si, and Al.

The reflection from the imprints based on the anodized masters were generally lowest with 60 and 90 nm ITO layers. Fig. 6.4 compares the reflection from imprints with 60 nm ITO, 300 nm Si and Al. It is seen that the CA1 imprints has the lowest reflection followed by the PA imprints, which seemed to be the general case. The CA1 imprint has a solar absorbance of 0.097 with 60 nm ITO. The lowest solar absorbance is obtained for a CA1 imprints with 165 nm ITO, but it is suspected that this could be due to an increased absorption in the ITO layer, which is not beneficial for a solar cell.

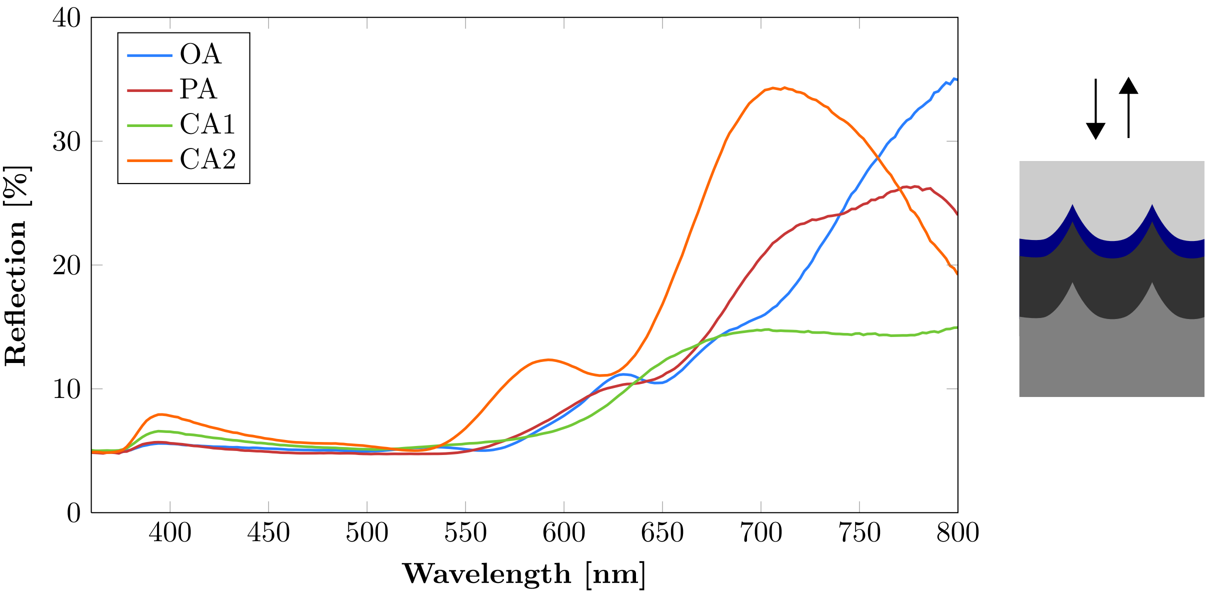

Figure 6.4. Reflection from anodized imprints with 60 nm ITO, 300 nm Si, and Al.

6.3 Simulations

Simulations of the optical properties of imprinted structures were carried out with *Lumerical FDTD Solutions*. Simulations were carried out in the wavelength span from 400–800 nm as the extinction coefficient of a-Si drops to zero around 800 nm, while the PMMA substrates absorb light below 400 nm. The photon flux at wavelengths from 280-400 nm only accounts for 5.17% of the total photon flux for the AM1.5 spectrum for wavelengths from 280–800 nm.

The measured reflection from flat surfaces was used to check the validity of simulated results together with calculations of the reflection from planar interfaces using the stack matrix method. The simulated and calculated reflections had similar shapes, but the simulated reflection was generally a little bit lower than the calculated, especially at minima. The comparisons with measured reflection revealed that there apparently was some issues with the refractive index of ITO and that there were some variations in the thickness of the deposited Si layers.

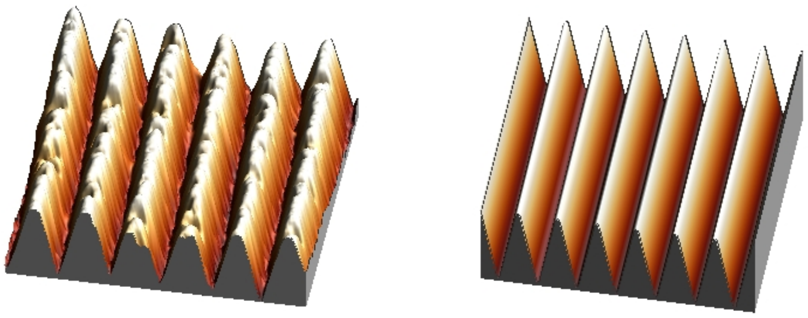

Figure 6.5. Comparison of AFM image and modeled structure for imprint based on the etched c-Si master with no layers deposited.

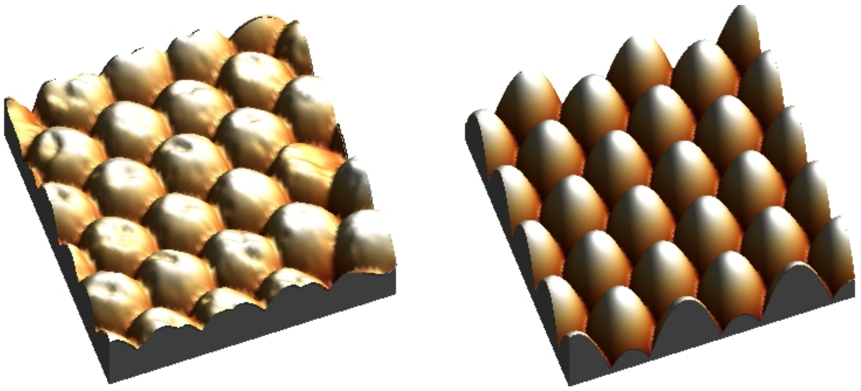

Figure 6.6. Comparison of AFM image and modeled structure for PA imprint with no layers deposited.

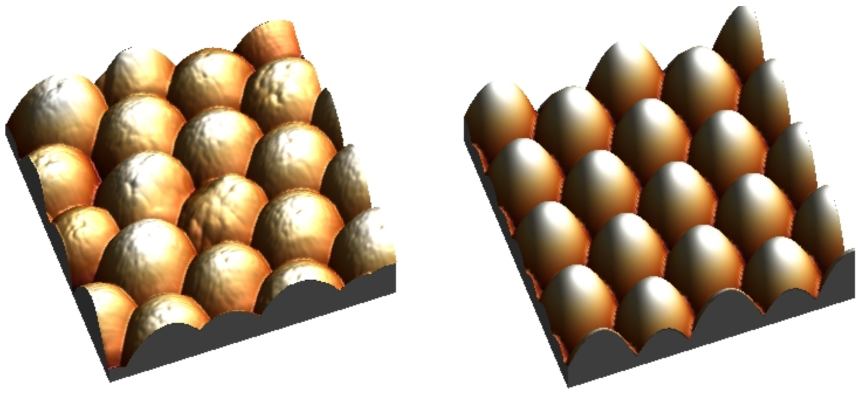

Figure 6.7. Comparison of AFM image and modeled structure for PA imprint with no layers deposited.

A model of an ideal structure was set up for the imprints based on the etched c-Si master, while a surface model was made for the PA and CA1 imprints based on AFM measurements of those surfaces. Figs. 6.5, 6.6, and 6.7 show comparisons of the measured and modeled surfaces. It is seen that the modeled surfaces clearly resemble the measured surfaces. The modeled surfaces are however too ideal compared to the imprinted structures. The peaks of the modeled imprint of the c-Si sample are a lot sharper than the peaks seen on the AFM image and the indentation depth is also deeper for the modeled structure. This could be partly explained by weaknesses of AFM measurements such as reaching the resolution of the AFM tip, but the model is still too ideal.
For the imprints based on the anodized samples it seem like the modeled surfaces are less rounded than the measured surfaces. The AFM images shown are of course not representative for the whole imprinted surface, but it still seems like the surface fitting method must be improved. It will however be a difficult task to obtain models that precisely represents the anodized surfaces due to the lack of long range order. It was also seen that the reflection from the simulations did not really fit with the measurements. For the imprints based on the etched c-Si master there were some similarities between the simulated and measured reflection at low wavelengths. As there was a bigger uniformity in the structure of the imprints based on the etched c-Si master it might be more feasible to obtain a reasonable model for the surface variations with layer thicknesses for that structure.

Chapter 7

Conclusions

Microstructured PMMA substrates based on micro-imprinting of different masters were prepared. Four masters were synthesized by anodic anodization of aluminum in different acids, while the fifth master was prepared by anisotropic etching in crystalline silicon. Indium tin oxide, amorphous silicon and aluminum layers were deposited on the imprinted substrates. The ITO deposition was optimized in order to obtain as low sheet resistance and as high transparency as possible. A low temperature PECVD recipe was used for a-Si deposition.

Reflection and transmission measurements for the imprinted structures with varying layers deposited were obtained with a spectrometer equipped with an integrating sphere. The reflection from the different imprinted structures were compared. After deposition of 300 nm a-Si and 150 nm Al it was shown that the microstructures decrease the reflection significantly compared to a planar surface with the same layers. An imprinted structure based on a master anodized in citric acid reflected 13.1% of the solar spectrum compared to 46.7% for the planar surface.
Adding an ITO layer with antireflective properties further decreased the reflection. An imprint based on the etched c-Si master with 50 nm ITO, 300 nm a-Si and 150 nm Al reflected 9.0% of the incident solar spectrum, while the reflection was 9.4% for a citric acid imprint with 90 nm ITO, 300 nm a-Si and 150 nm Al. It was seen that the imprint based on the master anodized in citric acid generally had the lowest reflection.

Simulations of the optical properties of the imprinted structures were carried out with *Lumerical FDTD Solutions* in order to determine the optimum ITO thickness. AFM measurements were used to obtain the surfaces of imprints based on anodized masters prepared in phosphoric and citric acid. Those measurements were used to make a model of the surfaces for simulations, while the imprinted structures based on the etched c-Si master were set up with a model based on an ideal structure. The simulated reflection was not in good agreement with the measured reflection, which is assumed to be caused by variations between the modeled and the measured surfaces. The simulations did indicate that a substantial fraction of the incident light is absorbed in the Al back contact at wavelengths above 600 nm.

The simulations and measurements both show that the reflection from an a-Si layer deposited on a microstructured PMMA substrate is decreased compared to the reflection from a planar surface and that the reflection may be further decreased by adding an antireflective layer. Additionally, the imprinting process should be viable for implementation at larger scales, for instance by imprinting large areas at the same time with a larger master or in a roll-to-roll production.

Appendices

Chapter A

Optimization of ITO, a-Si and Al

A.1 Optimization of indium tin oxide

The ITO deposition was optimized in order to decrease the sheet resistance and increase the transparency of the deposited layers. The oxygen content in ITO is an important parameter for controlling both the sheet resistance and the transparency[19,38]. Adding oxygen during sputtering of ITO films should therefore be an important parameter to test. Gorjanc et al.[19] did however obtain the best results by adding 0.1 % oxygen compared to argon during deposition. In Fig. A.1 it is seen that the argon flow used here is relatively low. As the master controller for adding oxygen requires a minimum flow of 5 sccm it is impossible to obtain an oxygen content of ∼1 % in the gas mixture. High quality ITO films can be grown without adding oxygen[48,49] but does instead require heating of the substrate in the 150–400°C range, which is above the glass transition temperature of PMMA.

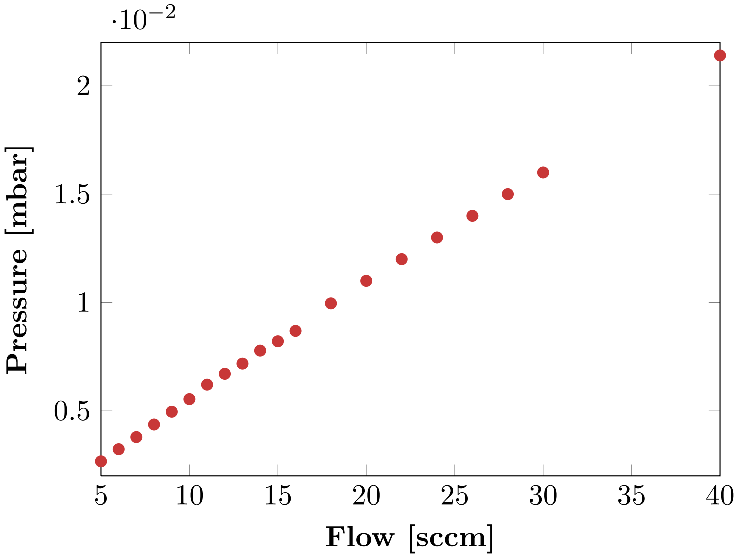

Figure A.1. Chamber pressure with respect to argon flow.

ITO deposition was carried out after pumping the chamber down to a base pressure of $2{\cdot}10^{-6}$ mbar, which is comparable to the base pressure used by Tuna et al.[48] Using a base pressure of $1{\cdot}10^{-5}$ mbar was tested but resulted in a higher sheet resistance, while going to pressures below $2{\cdot}10^{-6}$ mbar did show any significant improvements.

The deposition pressure, power, and rate are linked together as it requires a higher power to maintain a certain deposition rate at increased pressure. The ITO target was bonded to its holder with indium, which had a tendency to start melting above 60 W. The deposition power was therefore kept below 50 W, which corresponds well with the power between 40–50 W used by other authors[19,38,48]. The main parameter being tested is therefore the sputtering pressure with the deposition rate set at 0.3 Å/s. Fig. A.2 shows how the sheet resistance of a 100 nm ITO layer varies with sputtering pressure. It is seen that there is a minimum around $4{\cdot}10^{-3}$ mbar. Higher and lower deposition rates were also tested, but did not improve the results.

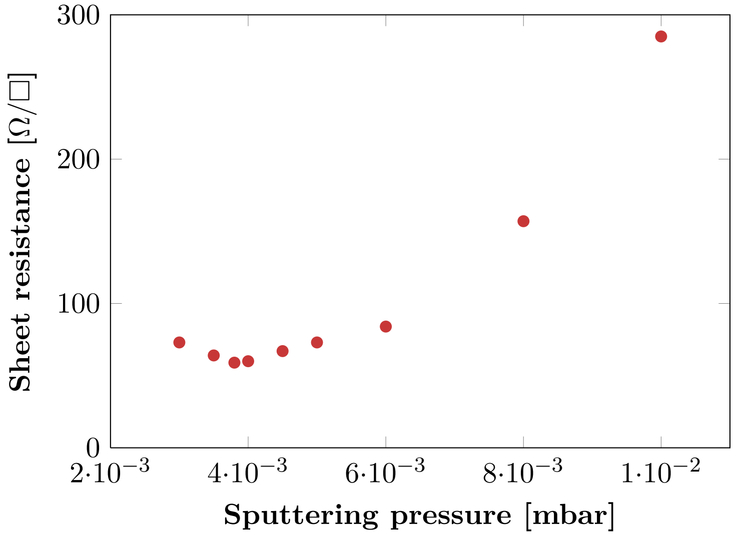

Figure A.2. Sheet resistance of 100 nm ITO with varying sputtering pressure.

The transparency of the ITO was determined by measuring the transmission through an ITO layer deposited on PMMA and then integrating over how much of the AM1.5 spectrum in the wavelength range from 400-800 nm was transitted in order to obtain the solar transmittance of ITO on PMMA. The solar transmittance of the PMMA was 0.8729. It should be noted that the transparency of the PMMA type used for this test was slightly lower than the transparency of the ITO used for making imprints. Fig. A.3 shows the solar transmittance of a 100 nm ITO layer deposited on PMMA with respect to sputtering pressure. It is seen that there are only small variations in the solar transmittance.

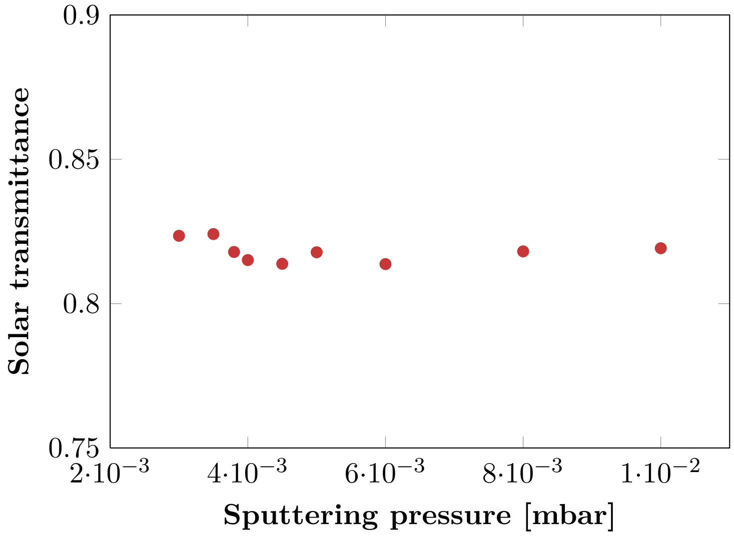

Figure A.3. Transmission of the AM1.5 spectrum for 100 nm ITO on PMMA with varying sputtering pressure.

Adding oxygen to the ITO deposition was tested by running a deposition with the turbopump shutter open, which made is possible to increase the argon flow to 60 sccm for a pressure of $4{\cdot}10^{-3}$ mbar. 5 sccm of oxygen was added during deposition which corresponds to ∼8 %. This was clearly to much oxygen considering the sheet resistance, as the resistivity was to high to measure the sheet resistance. It was however the sample with the highest transparency, showing a solar transmittance of 0.8385 for 110 nm ITO on PMMA. A sample with the same high oxygen flow and no oxygen flow was also made to test whether it was the higher flow that influence the sheet resistance, but this sample had similar sheet resistance compared to the samples in Fig. A.2. Energy-dispersive x-ray spectroscopy measurements did indicate that the oxygen content was higher in the ITO layer where an oxygen flow had been added during deposition compared to sample with no additional oxygen.

Fig. A.4 show the transmission through ITO layers with different thicknesses deposited on the PMMA type used for imprinting. The transmission through ITO layers with different thicknesses deposited on OA, PA, CA1, and CA2 samples is shown in Figs A.5, A.6, A.7, and A.8, respectively.

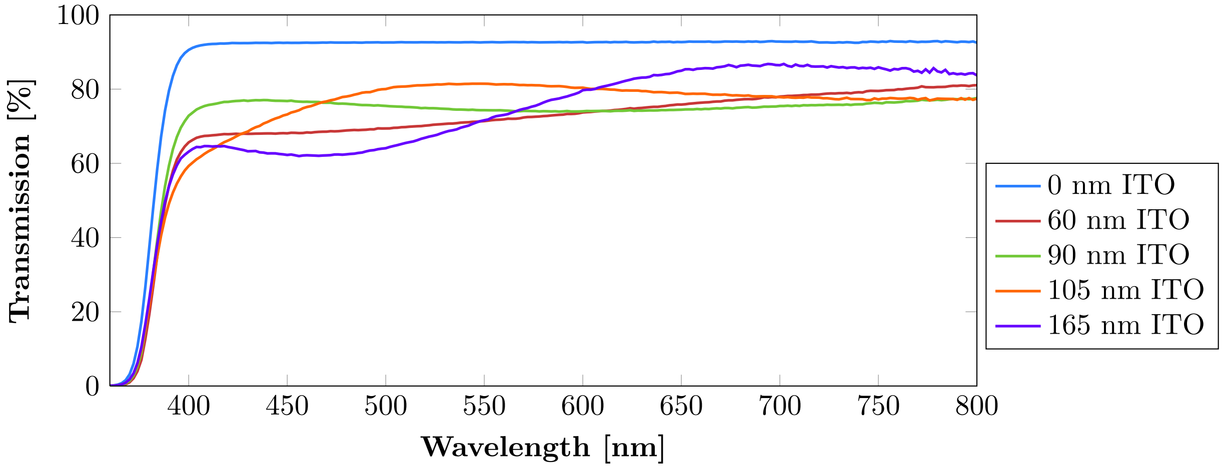

Figure A.4. Transmission for flat PMMA surfaces with varying ITO thickness.

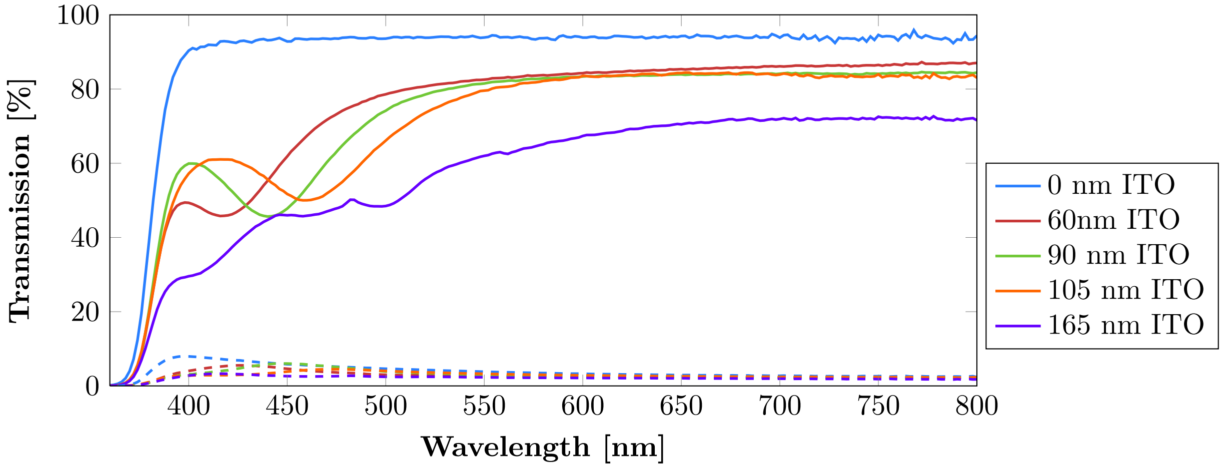

Figure A.5. Transmission for OA samples with ITO. Solid lines show transmission, while the dashed lines represent scattered transmission.

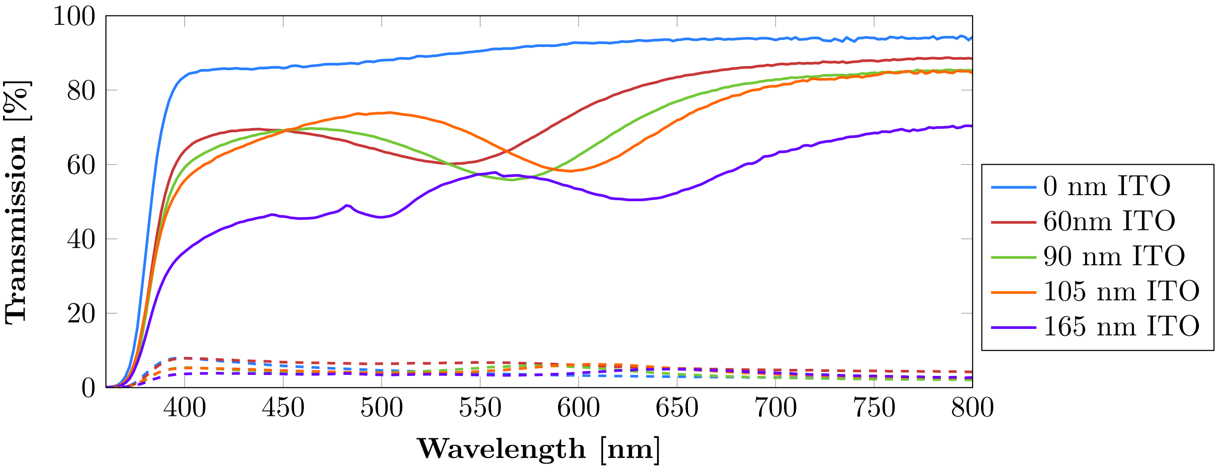

Figure A.6. Transmission for PA samples with ITO. Solid lines show transmission, while the dashed lines represent scattered transmission.

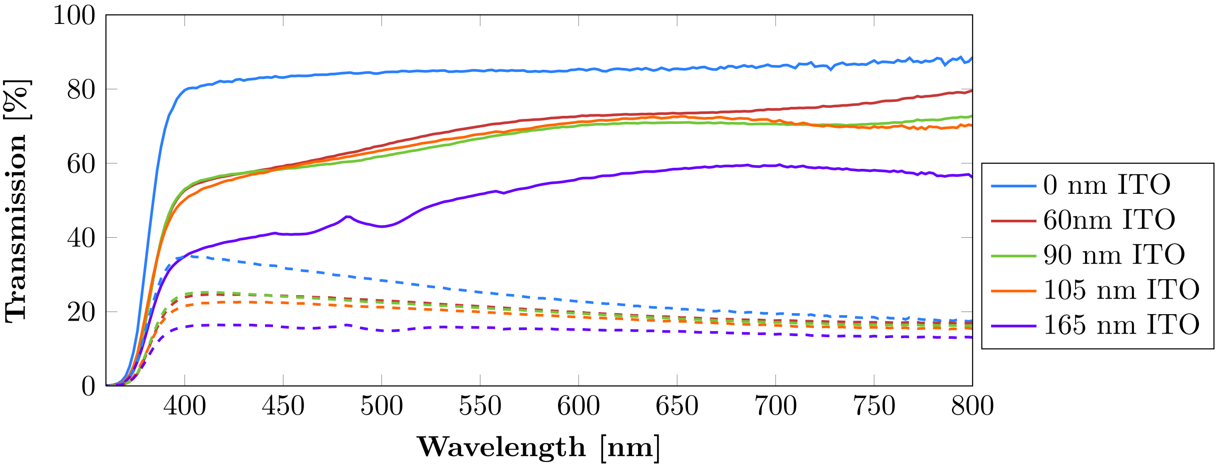

Figure A.7. Transmission for CA1 samples with ITO. Solid lines show transmission, while the dashed lines represent scattered transmission.

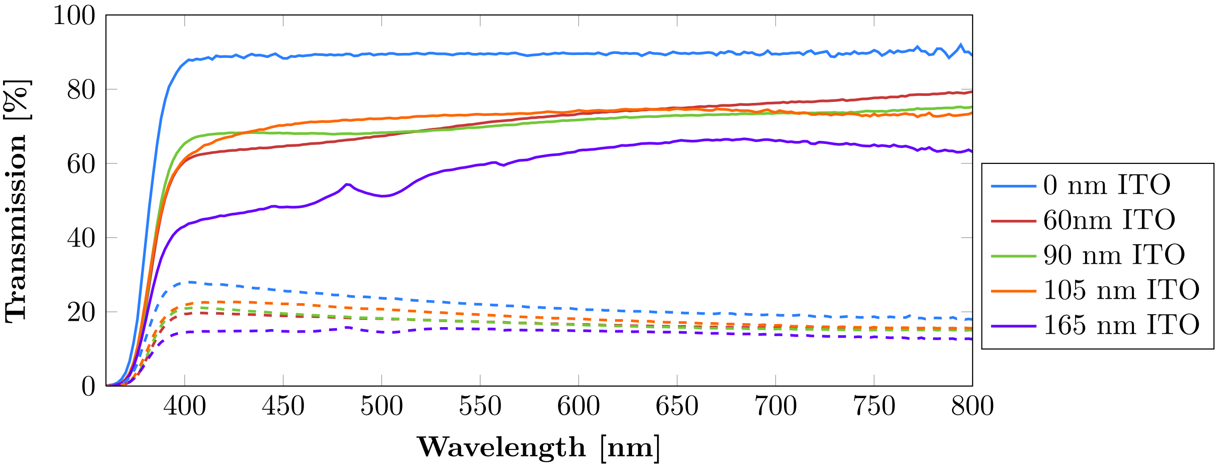

Figure A.8. Transmission for CA2 samples with ITO. Solid lines show transmission, while the dashed lines represent scattered transmission.

A.2 Optimization of silicon

Si had to be deposited at a low temperature due to the properties of PMMA. Silane was used as source gas and the RF power supply was set to frequency of 13.56 MHz. A temperature of ∼300°C is often used for Si deposition in a PECVD system[44], but Si depositions of good quality have been reported at temperatures from 100–250°C[40,41,43]. Using low temperature, low power and low pressure could all lead to Si films with less stress[44].

The first requirement was to obtain some temperature settings that the PMMA could withstand. The substrate and showerhead temperature can be set independently for the PECVD system. The two temperature settings were varied using a preset Si deposition recipe with the silane flow set to 50 sccm, the power set to 50 W and the process pressure set to 100 mtorr. Ten samples were made where the substrate temperature was varied between 50–80°C and the showerhead temperature between 150–200°C. The substrate temperature did not have that big effect as 80°C is already below the glass transition temperature of PMMA, while the PMMA was influenced by high showerhead temperatures. The substrate temperature was set to 50°C, while the showerhead temperature was set to 170°C, as the PMMA did not show any signs of melting at this showerhead temperature and the Si deposition became less uniform below 170°C.

Adding a hydrogen gas flow during deposition should improve the optical properties of the Si layer for solar cells applications by reducing the effects of dangling bonds[40,41]. Adding a H_2 between 50–1500 sccm was tested for process pressures between 100–1000 mtorr. Only depositions with low H_2 flow and low pressure turned out successfully, as there was either marks from the showerhead on the sample or a plasma did not ignite when increasing H_2 flow and/or process pressure.

Tab. A.1 shows how much of the AM1.5 spectrum in the wavelength range from 400–800 nm was transmitted (T_s) through Si deposited on glass for different deposition parameters. The deposition time was kept constant, which means that the thickness of the Si layer was different from sample to sample. Many other configurations were tested, but did either leave marks from the showerhead or did not ignite a plasma. It was suspected that the low temperature could be the reason behind the many unsuccessful attempts.

Sample number	**Power** [W]	**Process pressure** [mtorr]	**H_2 flow** [sccm]	**Si thickness** [nm]	T_s
1	50	100	0	84	0.45
2	50	100	50	72	0.41
3	50	100	100	66	0.39
4	50	60	0	67	0.40
5	50	150	0	112	0.37
6	70	60	0	93	0.46
7	70	100	0	99	0.43

Table A.1. Parameters for 10 min Si deposition with 50 sccm silane flow, where T_s is the corresponding solar transmittance.

From Tab. A.1 it is noted that the deposition rate increases with increasing power and pressure, while it decreases when the H_2 flow increases. It is seen that samples 2, 3, and 4 have a relatively low solar transmittance considering the thickness of the Si layer. The uniformity of the deposited Si layer was rather poor for samples 2, 6, and 7 and they were therefore dismissed.

300 nm Si layers following the recipes of samples 1, 3, 4, and 5 were deposited in order to make measurements of films with the same thickness. The deposition for recipes 3 and 4 did however

turn out to be very unstable for longer deposition times and had to be aborted. The transmission and reflection was measured for the 300 nm layers deposited on glass following recipe 1 and 5. Calculating the solar absorbance for the two layers as $A = 1 - T - R$ showed that the 300 nm Si layer deposited following recipe 1 absorbed 41.67 % of the AM1.5 spectrum in the wavelength range from 400-800 nm, while the corresponding number for recipe 5 was 40.93 %.

There was no significant difference between the solar absorbance for a 300 nm Si layer deposited following recipes 1 and 5. It was chosen to use recipe 1 for deposition on imprinted substrates as it did show the highest solar absorbance. Fig. A.9 shows transmission and reflection data for Si layers with different thicknesses deposited on glass following recipe 1, while Fig. A.10 shows how the Si thickness varies with respect to deposition time t.

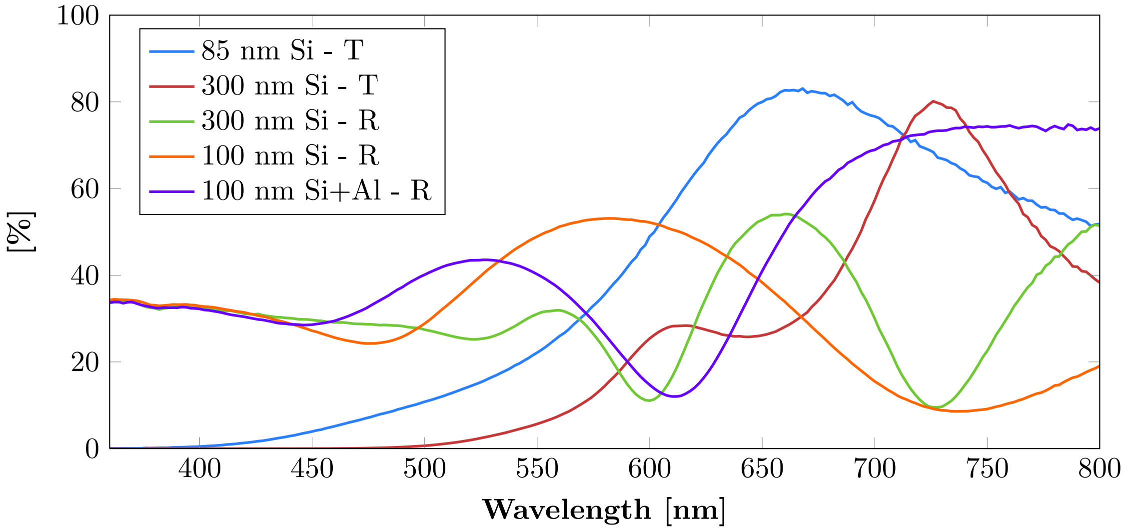

Figure A.9. Transmission and reflection for Si deposited on glass for different Si thicknesses.

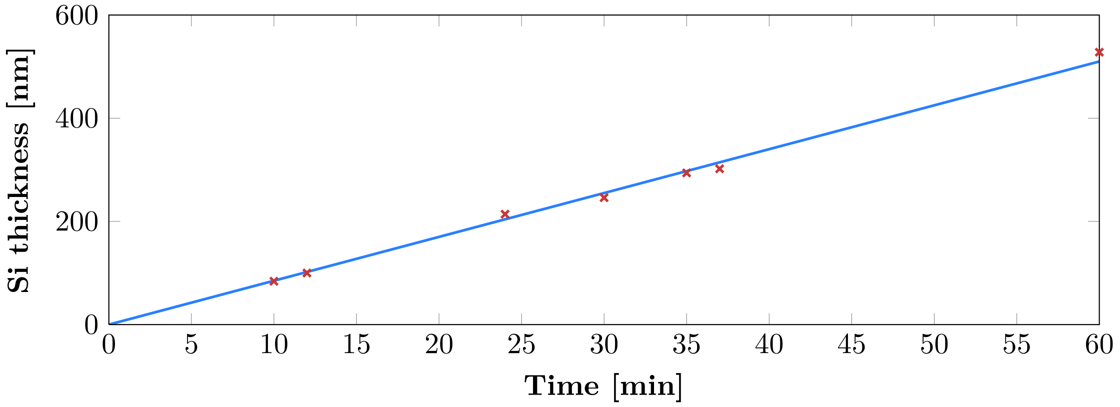

Figure A.10. Si thickness with respect to deposition time. The red marks show the data points, while the solid line is a linear fit where $f(t) = t \cdot 8.50$ nm/min.

The refractive index of the deposited Si layer was determined by ellipsometry following a Tauc-Lorentz model[27,30]. The model uses four fitting parameters E_g, A, E_0, and C to obtain the imaginary and real parts of the dielectric function $\varepsilon = \varepsilon_r + i\varepsilon_i$ by[27,30]

$$\varepsilon_i(E) = \begin{cases} \left[\dfrac{AE_0C(E-E_g)^2}{(E^2-E_0^2)^2+C^2E^2}\cdot\dfrac{1}{E}\right], & E > E_g, \\ 0, & E \leq E_g, \end{cases} \tag{A.1}$$

$$\begin{aligned} \varepsilon_r(E) = {} & \varepsilon_r(\infty) + \frac{A\cdot C}{\pi\zeta^4}\cdot\frac{a_1}{2\alpha E_0}\cdot\ln\left(\frac{E_0^2+E_g^2+\alpha E_g}{E_0^2+E_g^2-\alpha E_g}\right) \\ & -\frac{A}{\pi\zeta^4}\cdot\frac{a_2}{E_0}\cdot\left[\pi - \operatorname{atan}\left(\frac{2E_g+\alpha}{C}\right) + \operatorname{atan}\left(\frac{-2E_g+\alpha}{C}\right)\right] \\ & +\frac{2AE_0E_g}{\pi\zeta^4\alpha}\cdot(E^2-\gamma^2)\cdot\left[\pi + \operatorname{atan}\left(2\frac{\gamma^2-E_g^2}{\alpha C}\right)\right] \\ & -\frac{AE_0C}{\pi\zeta^4}\cdot\frac{E^2+E_g^2}{E}\cdot\ln\left(\frac{|E-E_g|}{E+E_g}\right) \\ & +\frac{2AE_0CE_g}{\pi\zeta^4}\cdot\ln\left[\frac{|E-E_g|\cdot(E+E_g)}{\sqrt{(E_0^2-E_g^2)^2+E_g^2C^2}}\right], \end{aligned} \tag{A.2}$$

where

$$\begin{aligned} a_1 &= (E_g^2-E_0^2)E^2+E_g^2C^2-E_0^2(E_0^2+3E_g^2), \\ a_2 &= (E^2-E_0^2)(E_0^2+E_g^2)+E_g^2C^2, \\ \alpha &= \sqrt{4E_0^2-C^2}, \\ \gamma &= \sqrt{E_0^2-C^2/2}, \\ \zeta^4 &= (E^2-\gamma^2)^2+\alpha^2C^2/4. \end{aligned}$$

The refractive index is determined from Eqs. A.1 and A.2 by[50]

$$n = \sqrt{\frac{\sqrt{\varepsilon_r^2+\varepsilon_i^2}+\varepsilon_r}{2}}, \tag{A.3}$$

$$k = \sqrt{\frac{\sqrt{\varepsilon_r^2+\varepsilon_i^2}-\varepsilon_r}{2}}. \tag{A.4}$$

The refractive index obtained for Si recipe 1 is shown in App. E. The refractive index is obtained by averaging over the refractive indies obtained by ellipsometric measurements of samples with varying Si thicknesses. It is seen that the extinction coefficient is lower compared to a refractive index that was experimentally determined in an earlier project[14] for a PECVD deposition at a higher temperature. This means that the low temperature Si layer should absorb less light.

It is obvious that there is room for further improvement of the recipe for low temperature deposition of Si. This is further confirmed by the fact that an Si layer deposited on flat a flat ITO layer tends to crackle. Fig. A.11 shows an image obtained with a Leica DMI3000 M inverted microscope of the surface of an OA sample with 70 nm ITO and 300 nm Si. It is seen that the Si layer on the flat area is full of cracks, while it is smooth and intact on the microstructured area. This was a general trend seen on all samples. It means that the Si deposited on the imprinted samples is fine for further measurements, but it also shows that there are some unresolved issues with the Si depositions.

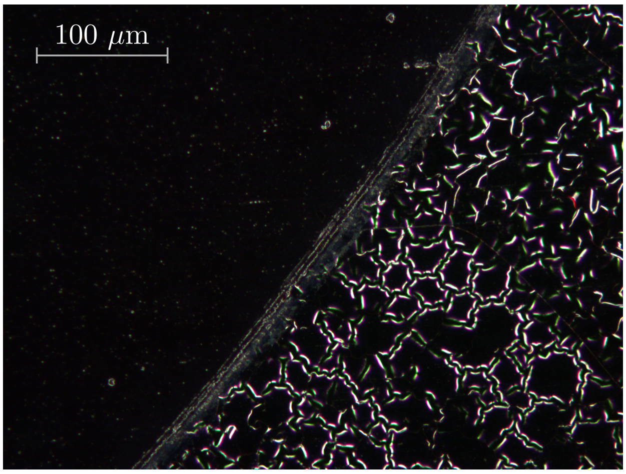

Figure A.11. Microscope image of the interface between a microstructured area to the left and a flat area to the right for an OA sample with 70 nm ITO and 300 nm Si.

A.3 Optimization of aluminum

Transmission measurements were made for Al layers with different thicknesses in order to determine a thickness, where no light was transmitted in the spectrum of interest. An Al thickness of 150 nm on glass does not transmit any light according to Fig. A.12.

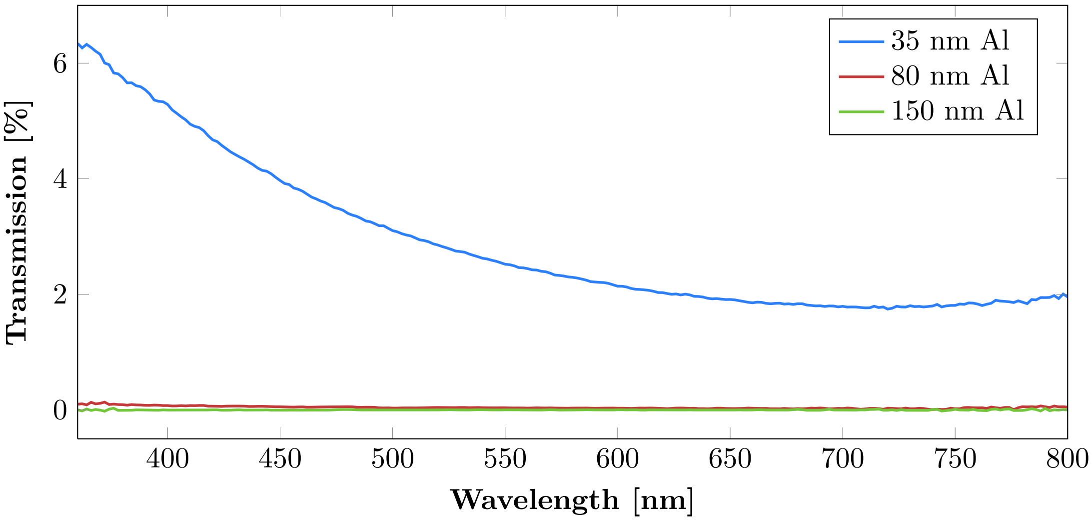

Figure A.12. Transmission for Al deposited on glass for different Al thicknesses.

Chapter B

AFM images of imprints with ITO and a-Si

AFM images were acquired for PA and CA1 imprints with ITO and Si deposited. Figs. B.1 and B.2 show CA1 surfaces with ITO and Si deposited.

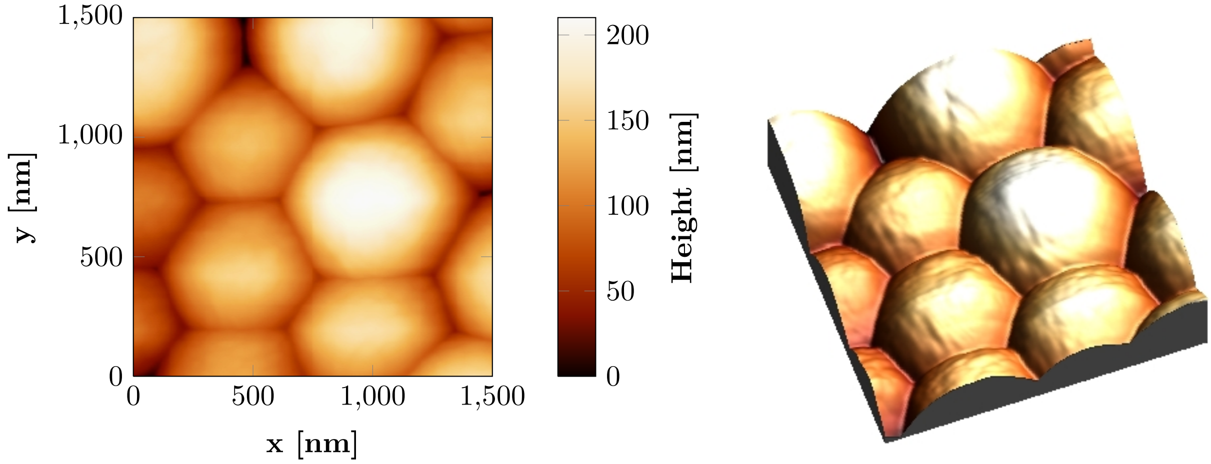

Figure B.1. AFM images of CA1 imprint with 90 nm ITO and 300 nm Si.

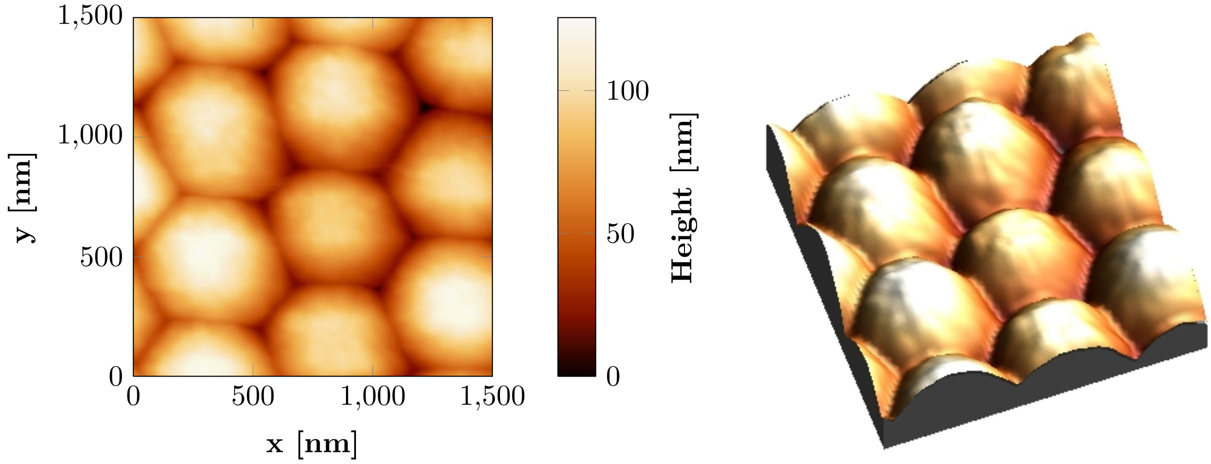

Figure B.2. AFM images of CA1 imprint with 105 nm ITO and 300 nm Si.

Different thicknesses of Si was deposited in order to find out how the surfaces change with Si thickness. Figs. B.3, B.4, and B.5 show how the surface varies for PA samples with 65 nm ITO, while Figs. B.6, B.7, and B.8 show how it varies for PA samples with 95 nm ITO. It is seen that there is no clear correlation between the Si thickness and the imprint depth.

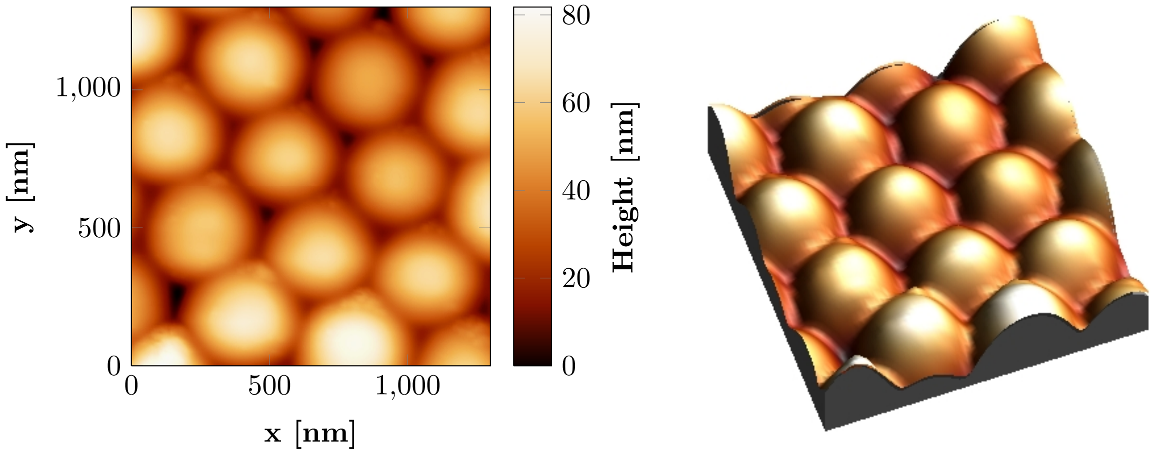

Figure B.3. AFM images of PA imprint with 65 nm ITO and 100 nm Si.

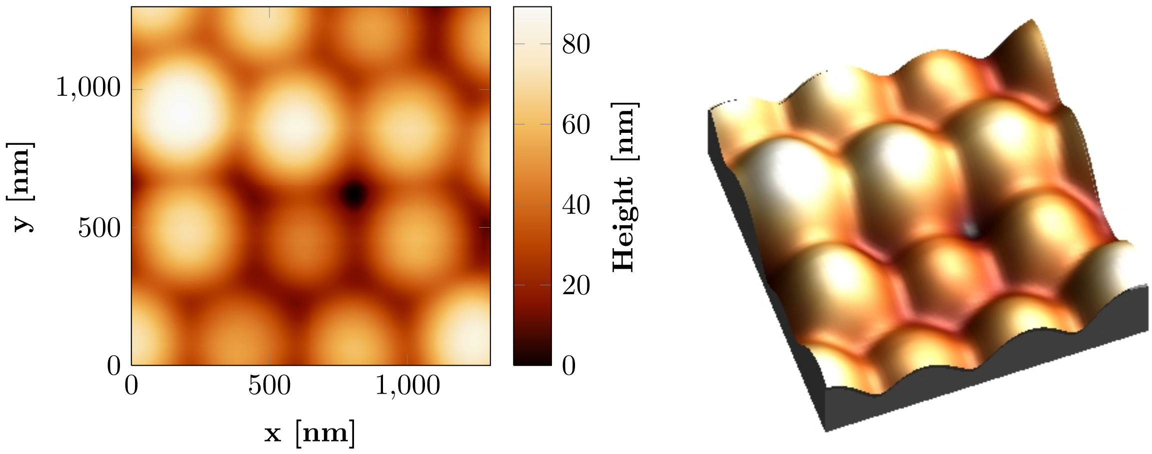

Figure B.4. AFM images of PA imprint with 65 nm ITO and 200 nm Si.

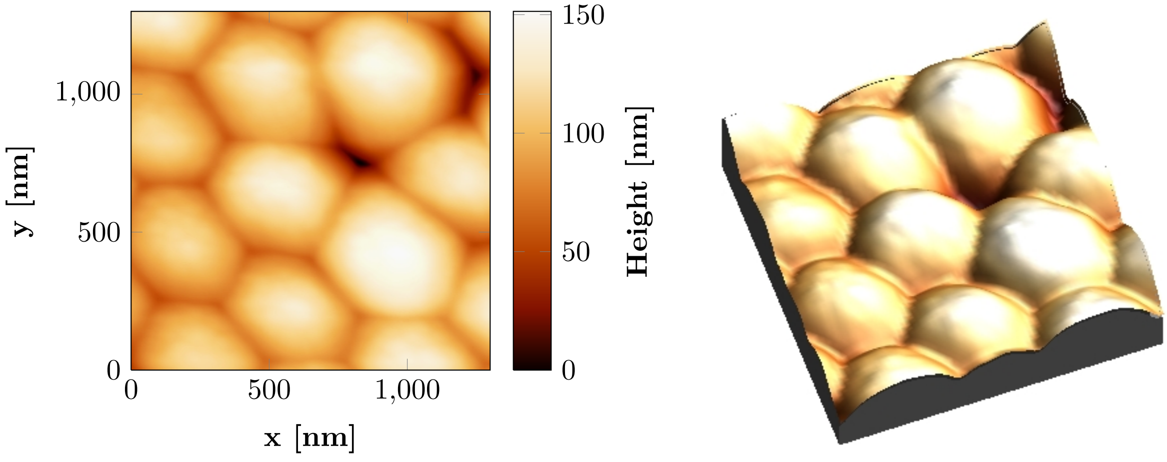

Figure B.5. AFM images of PA imprint with 65 nm ITO and 300 nm Si.

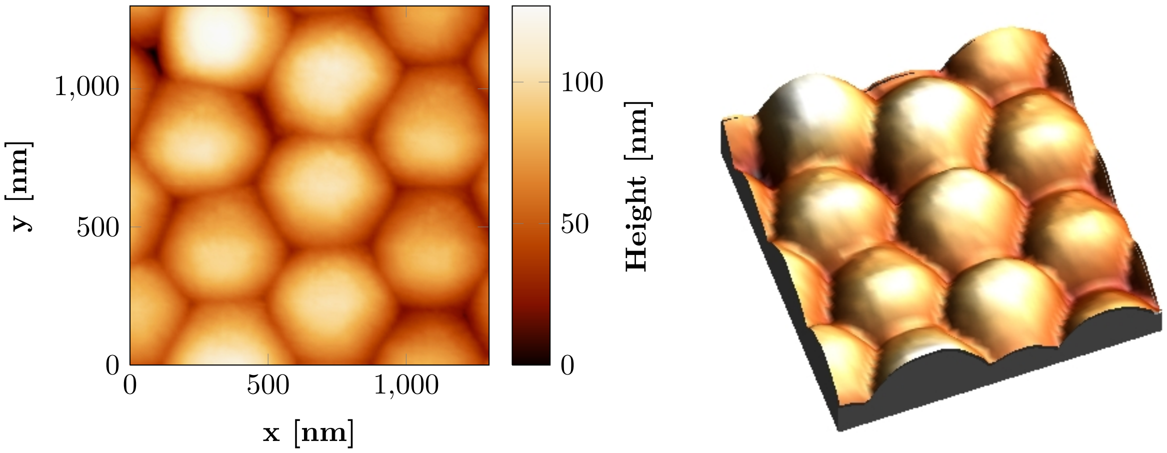

Figure B.6. AFM images of PA imprint with 95 nm ITO and 100 nm Si.

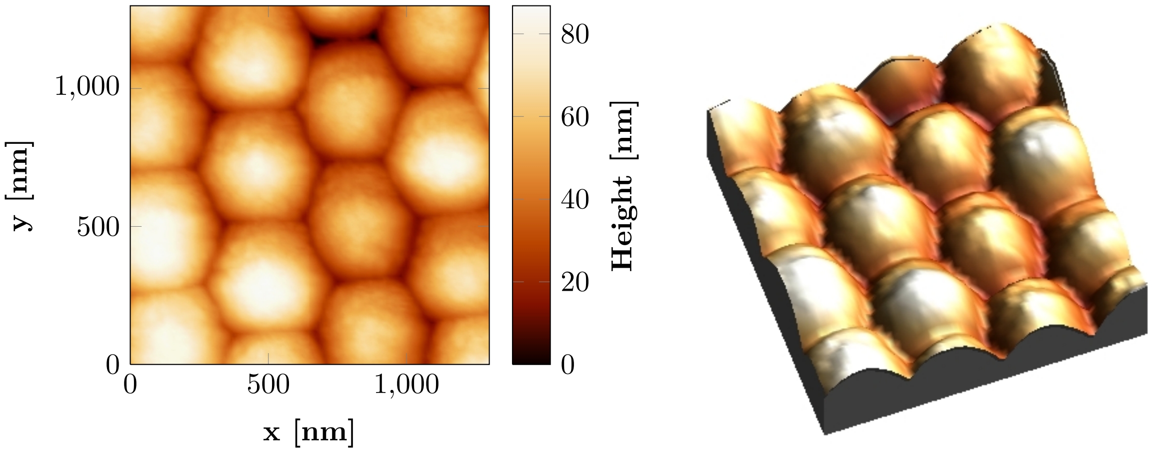

Figure B.7. AFM images of PA imprint with 95 nm ITO and 200 nm Si.

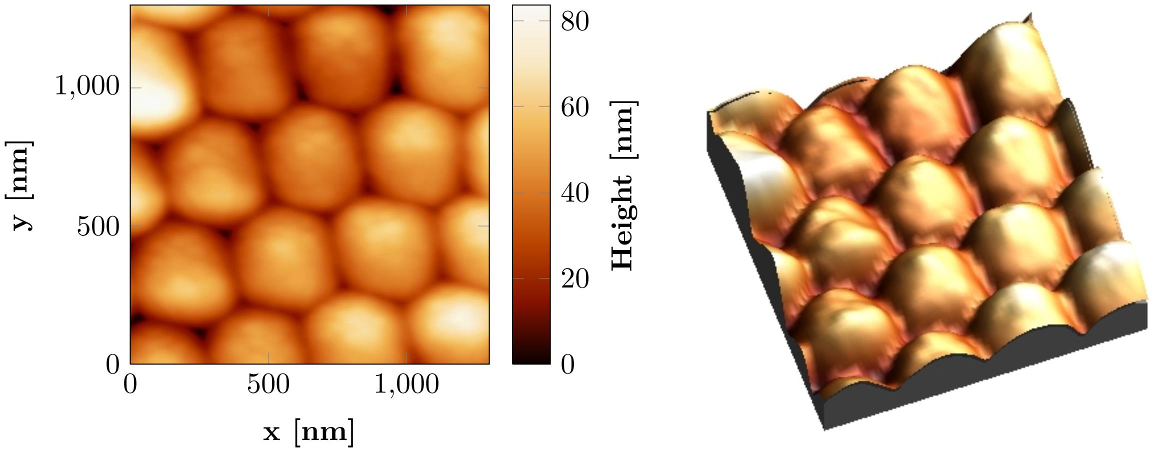

Figure B.8. AFM images of PA imprint with 95 nm ITO and 300 nm Si.

Chapter C

Transmission and reflection measurements

Some additional reflection and transmission measurements are shown here. Fig. C.1 shows the transmission for PA and CA1 imprints after deposition of 150 nm Al, where it is seen that the aluminum layer effectively blocks the light.

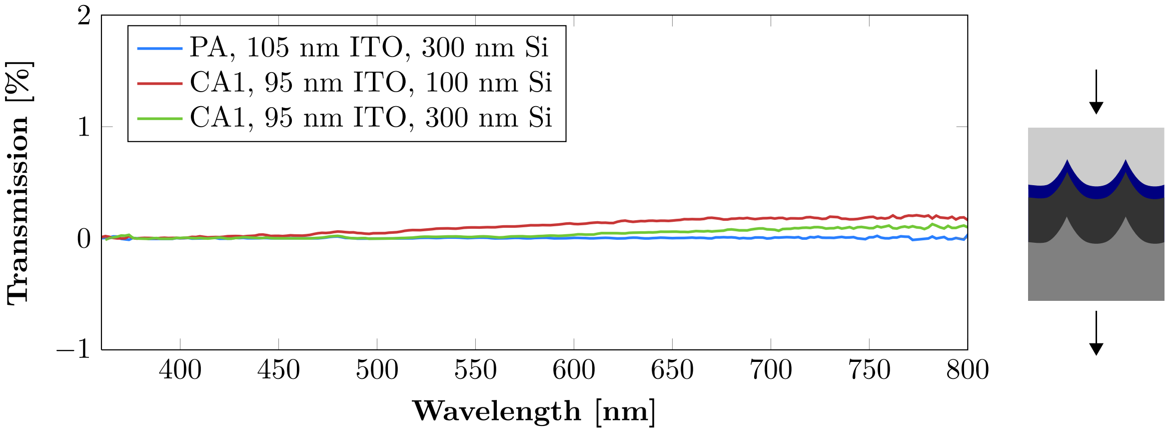

Figure C.1. Transmission for PA and CA1 imprints with varying ITO and Si thickness and Al.

The reflection from imprints from the etched c-Si master with varying ITO and Si thickness is shown Fig. C.2. It is seen that the reflection is lowest for 200 and 300 nm Si when the ITO thickness is 105 nm, while it is lowest for 100 nm Si with an ITO thickness of 25 nm.

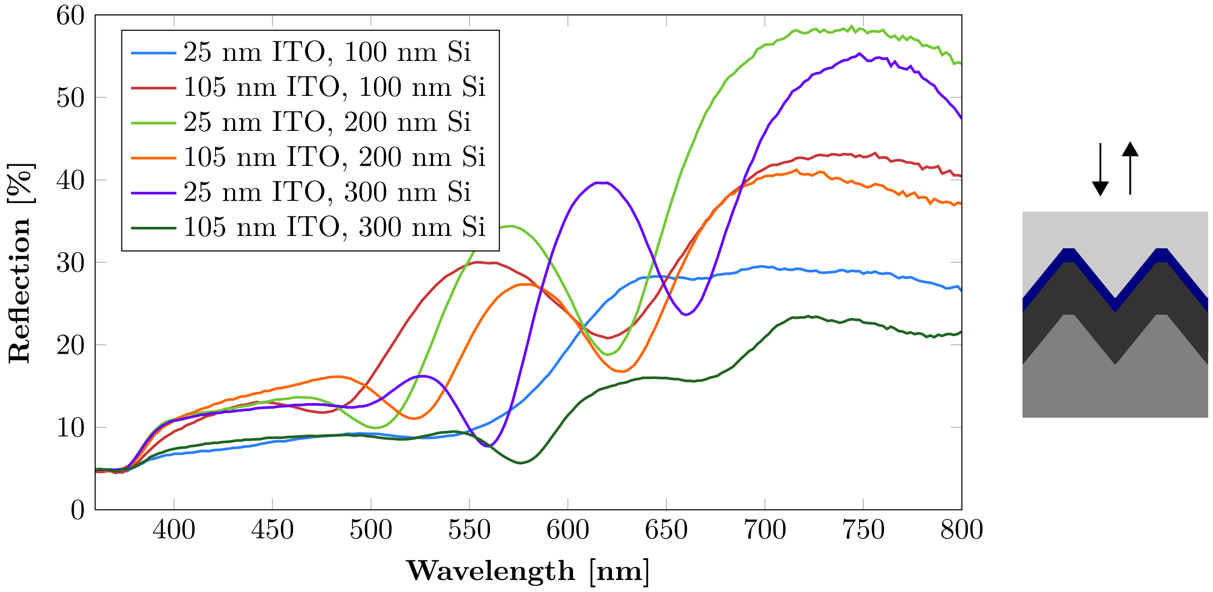

Figure C.2. Reflection from imprints from etched c-Si master with varying ITO and Si thickness and Al.

The transmission and reflection for PA imprints with varying ITO and Si thickness is shown in Figs. C.3 and C.4. The total transmission does not vary much with the ITO thickness, but it is noted that the transmitted light is scattered more for the 65 nm ITO layer compared to the samples with 95 nm ITO. The reflection is seen to decrease after deposition of Al, which follows the trend seen for PA samples in Sec. 3.4.

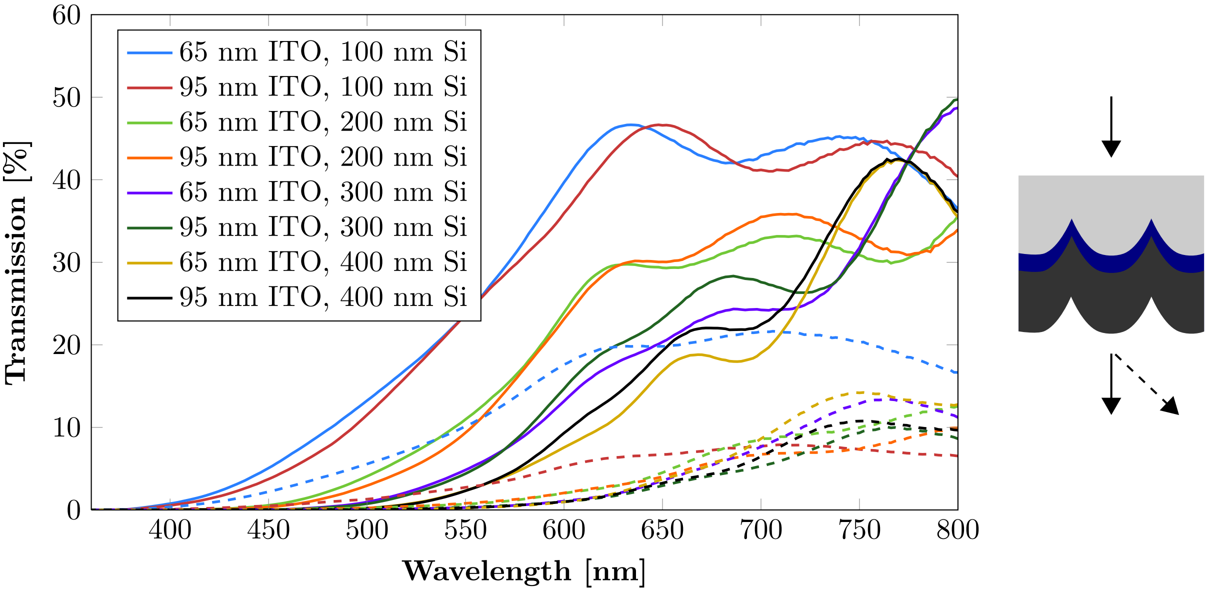

Figure C.3. Transmission for PA imprints with varying ITO and Si thickness. Solid lines show total transmission, while the dashed lines represent scattered transmission.

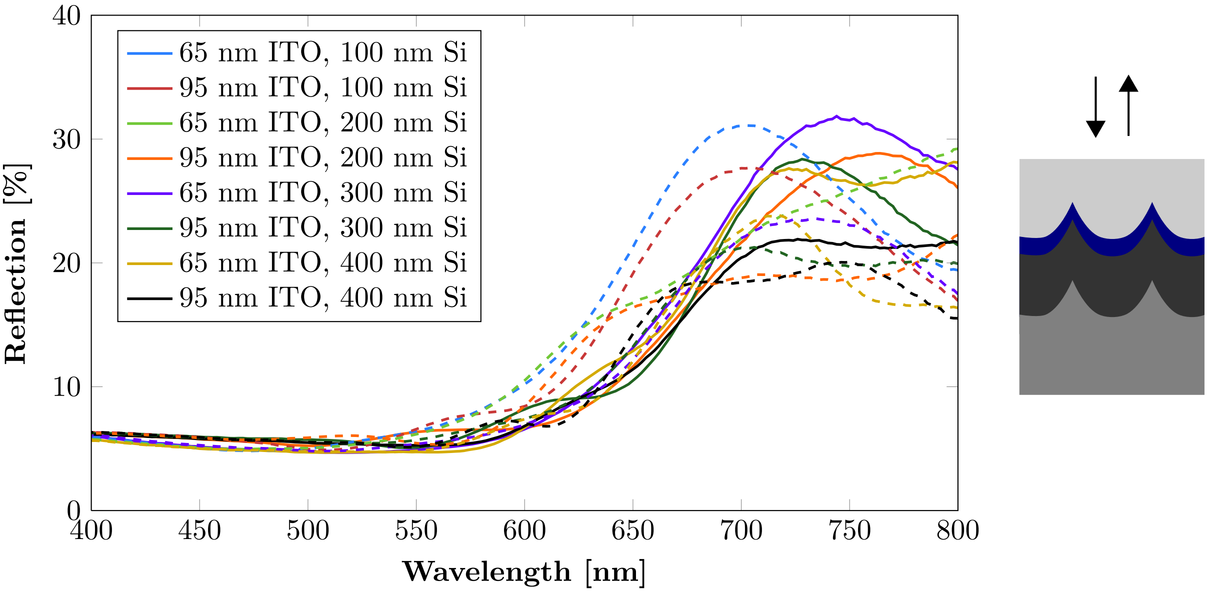

Figure C.4. Reflection from PA imprints with varying ITO and Si thickness. Solid lines show reflection before Al deposition, while dashed lines represent reflection after Al deposition. The reflection from some of the samples was only measured after Al deposition.

Figs. C.5 and C.6 show the transmission and reflection for CA1 imprints with varying ITO and Si thickness. It is seen that the transmission for the CA1 samples is higher for an ITO thickness of 65 nm compared to using 95 nm ITO and that the scattered transmission is not very dependent on the ITO thickness. This is in contrast to the PA samples shown in Fig. C.5, where the total transmission did not depend very much on ITO thickness, while the scattered transmission varied with ITO thickness. The reflection from the CA1 samples shows that the reflection decreases after Al deposition as seen for CA1 samples in Sec. 3.4.

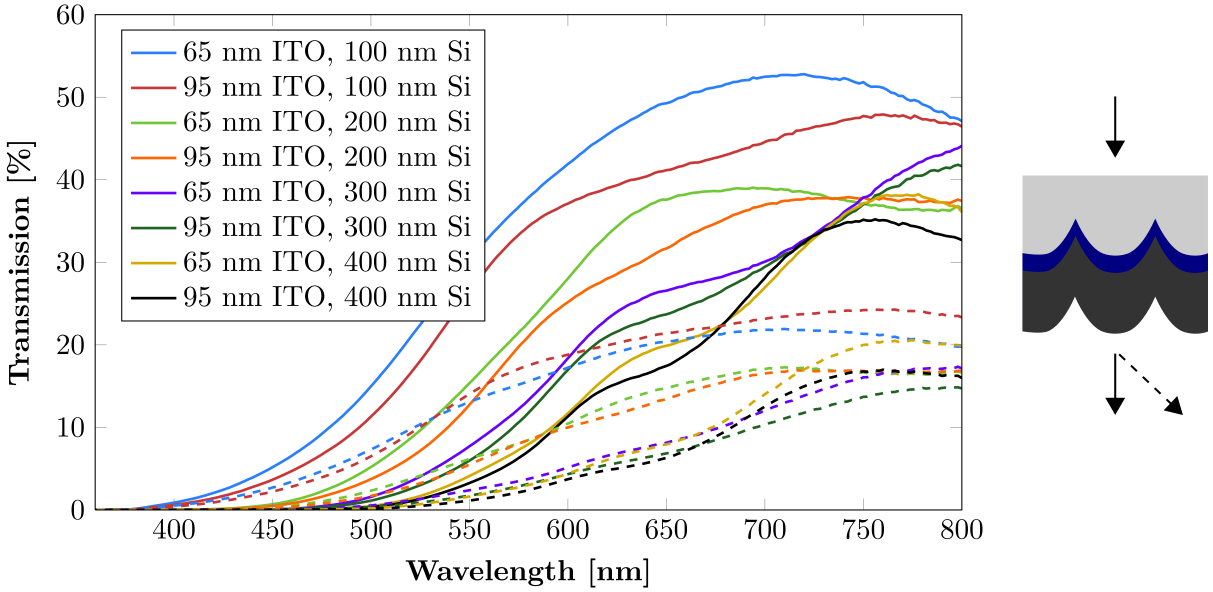

Figure C.5. Transmission for CA1 imprints with varying ITO and Si thickness. Solid lines show total transmission, while the dashed lines represent scattered transmission.

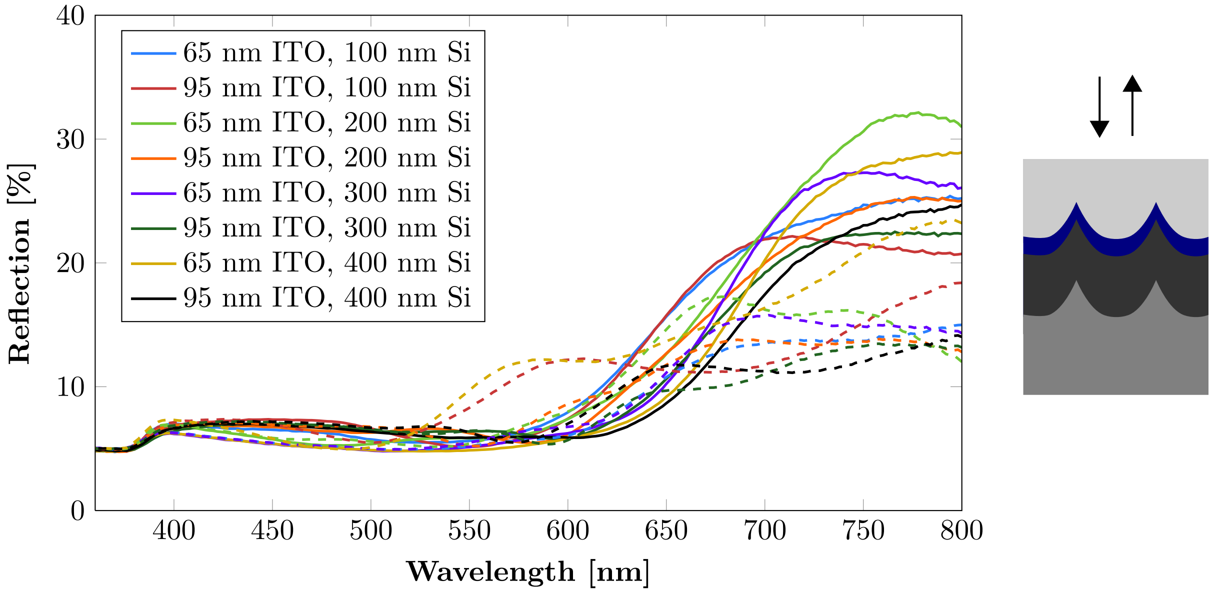

Figure C.6. Reflection from CA1 imprints with varying ITO and Si thickness. Solid lines show reflection before Al deposition, while dashed lines represent reflection after Al deposition.

The solar reflectance for the PA and CA1 imprints with varying ITO and Si thickness is shown in Tab. C.1. It is seen that the solar reflectance tends to decrease with increasing Si thickness and that the 95 nm ITO leads to lower reflection compared to the 65 nm ITO layer. The CA1 imprints have a lower solar reflectance compared to the PA imprints which follows the results shown in Tab. 3.5 in Sec. 3.4.

ITO	**Si**	R_s	R_s
		PA	**CA**
65 nm	100 nm	0.202	0.127
65 nm	200 nm	0.143	0.105
65 nm	300 nm	0.120	0.096
65 nm	400 nm	0.113	0.090
95 nm	100 nm	0.142	0.108
95 nm	200 nm	0.121	0.098
95 nm	300 nm	0.120	0.089
95 nm	400 nm	0.113	0.092

Table C.1. Solar reflectance for PA and CA1 imprints with varying ITO and Si thickness and Al.

Four additional samples were made where the layers were deposited oppositely for comparison with the results presented in Tab. 3.5 in Sec. 3.4. The imprints were used as structured back surfaces and Al, Si and ITO layers were deposited. Fig. C.7 shows the reflection after deposition of each layer. It shows the antireflective properties of the ITO layer as the reflection is reduced after deposition of 70 nm ITO.

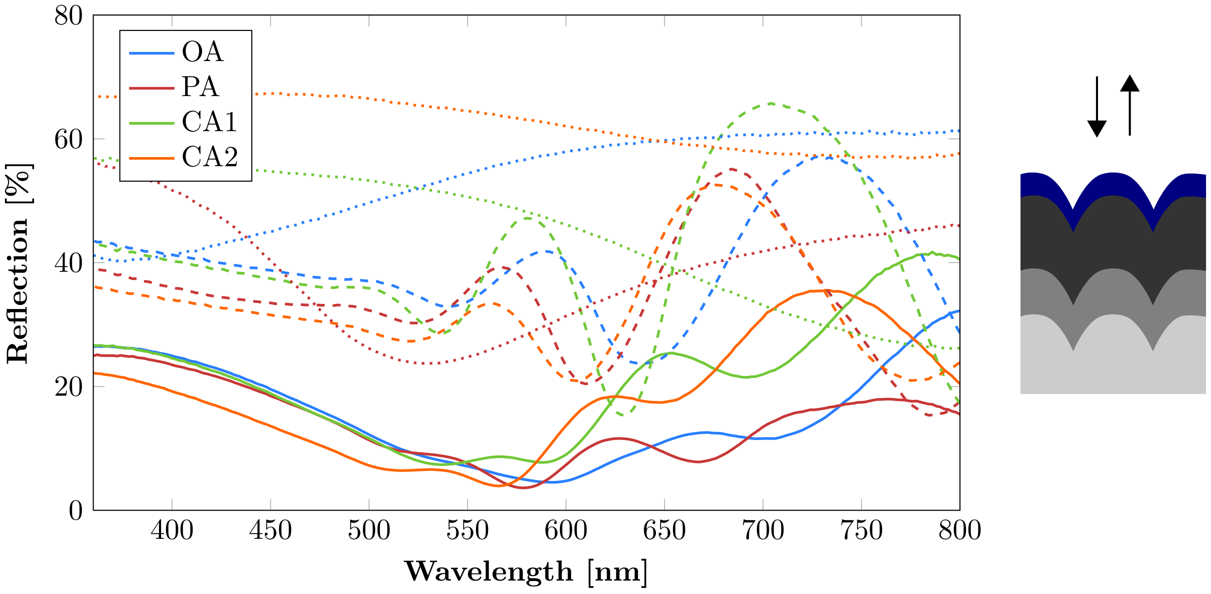

Figure C.7. Reflection from imprints with layers deposited oppositely. Dotted lines show the reflection from microstructured Al surfaces, dashed lines represent reflection after deposition of 300 nm Si, and solid lines show the reflection after deposition of a final ITO layer with a thickness of 70 nm.

The reflection from the imprinted structures with layers deposited in opposite order are compared to imprinted structures with the standard layers. The ITO thickness is not the same, which means that the plots are not directly comparable, but it is seen that the reflection from the imprints with standard layers is lowest for wavelengths below 550 nm and for the CA1 sample it is lowest at all wavelengths for the imprint with normal layers. The solar reflectance for the reflection measurements shown in Fig. C.8 can be seen in Tabs. C.2 and C.3. The solar reflectance is lowest for the imprints with standard layers for all four imprints types. It is also noted that the CA1 imprint is the imprint resulting in the highest solar reflectance for the opposite layers, which is in contrast to the case with standard layers where the CA1 imprint always shows the lowest solar reflectance.

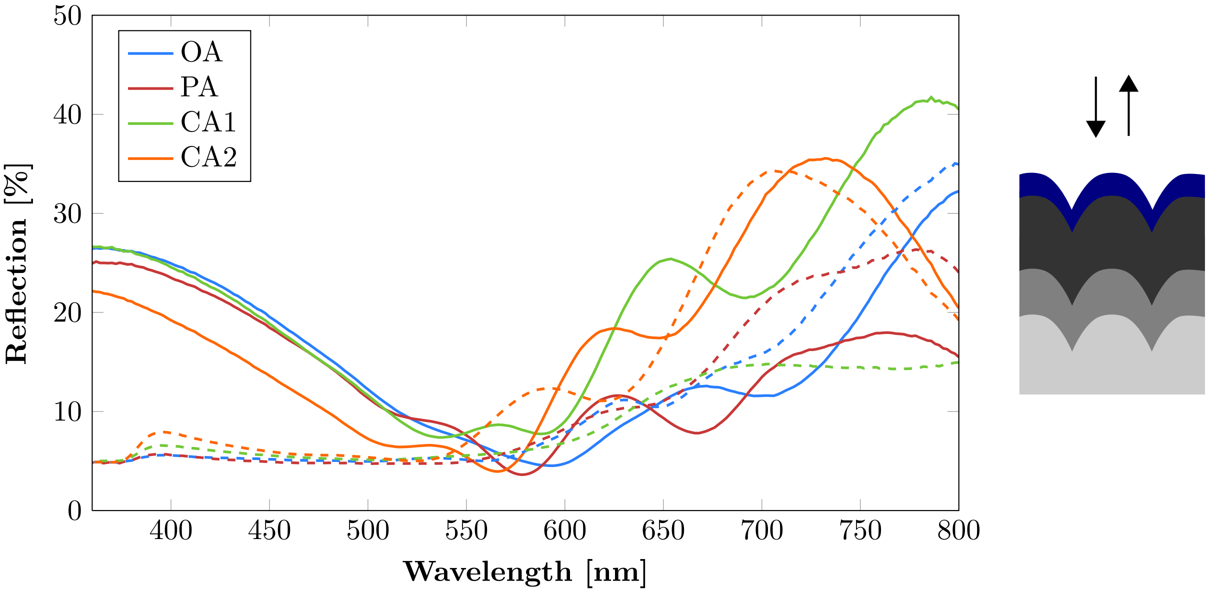

Figure C.8. Reflection from imprinted structures. Solid lines show the reflection from imprints with layers deposited oppositely with Al, 300 nm Si, and 70 nm ITO, while the dashed lines show the reflection from imprints with standard layers with 60 nm ITO, 300 nm Si, and Al.

Sample type	R_s
OA	0.138
PA	0.125
CA1	0.204
CA2	0.181

Table C.2. Solar reflectance for imprints were the layers are deposited in reversed order with Al, 300 nm Si, and 70 nm ITO.

Sample type	R_s
OA	0.126
PA	0.124
CA1	0.097
CA2	0.164

Table C.3. Solar reflectance for imprints from anodized master with 60 nm ITO, 300 nm Si, and Al.

Chapter D

Convergence testing for simulations

The simulated results presented in Chap. 5 were obtained using *Lumerical FDTD Solutions*. In order to obtain reliable results and to decrease simulation time, different parameters and settings were varied and tested for convergence. The convergence testing will be described here. The simulations for the triangular structure shown in Fig. 4.1 were tested first and the settings obtained for that structure were then used as starting points for simulations of the anodized structures. The convergence testing was carried out by looking at the IQE of the Si layer and by comparing plots of the absorption in the Si layer with respect to wavelength. The deposition of Si had not been commenced at the time where the convergence testing was done. A refractive index for a-Si obtained from an earlier project[14] was used for the simulations carried out in this chapter.

D.1 Triangular structure

The convergence testing was carried out for a structure as shown in Fig. 4.1 with the modeling parameters listed in Tab. D.1. The parameters that were tested for convergence were the *mesh accuracy*, *number of frequency points*, *auto shutoff min*, *min mesh step*, *min PML layers*, *source position*, *source width*, *Al thickness*, *bottom boundary type*, and *dt stability factor*. The default settings have been used for all other settings. The power absorption plots and IQEs for the Si layer are shown for the mesh accuracy, number of frequency points, auto shutoff min, min mesh step, and min PML layers.

Parameter	**Setting**
Period L	700 nm
Al thickness $h1$	500 nm
Si thickness $h2$	500 nm
ITO thickness $h3$	100 nm
Width of flat surface d	50 nm

Table D.1. Parameters for the triangular structure used for convergence testing.

Figs. D.1 and D.2 show how the mesh accuracy influences the power absorption and IQE for the Si layer. The mesh accuracy mainly affects the number of mesh points in different materials and can be set as an integer from 1–8, where 8 corresponds to the highest accuracy[51]. It is seen that the power absorption and IQE for both s- and p-polarization get closer to converging with increasing mesh accuracy. At mesh accuracy 8 the results have not fully converged, but the simulations were chosen to be run with mesh accuracy 8.

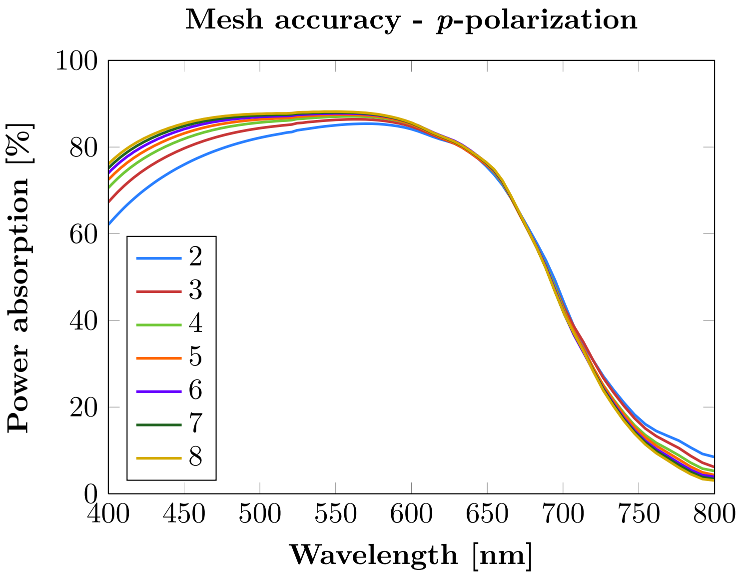

Mesh accuracy	IQE
2	0.6218
3	0.6291
4	0.6317
5	0.6335
6	0.6352
7	0.6360
8	0.6370

Figure D.1. Absorption in Si with respect to wavelength for p-polarized light with varying mesh accuracy and the corresponding IQE.

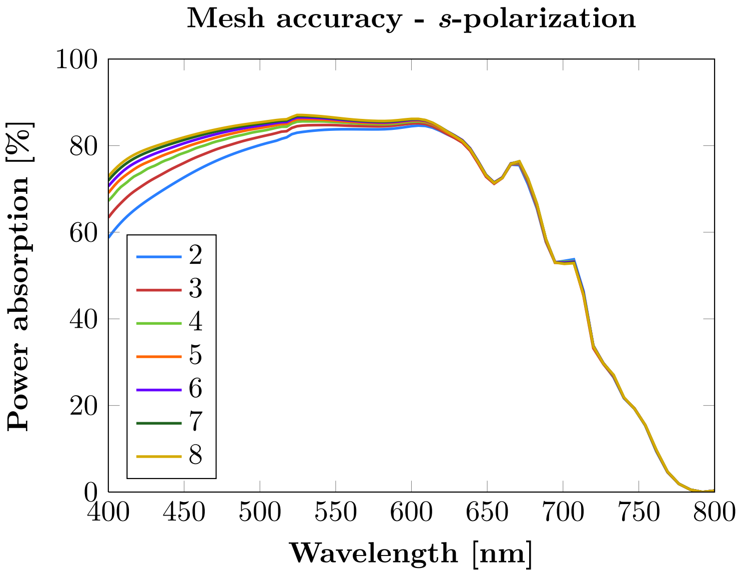

Mesh accuracy	IQE
2	0.6192
3	0.6280
4	0.6356
5	0.6389
6	0.6423
7	0.6444
8	0.6458

Figure D.2. Absorption in Si with respect to wavelength for s-polarized light with varying mesh accuracy and the corresponding IQE.

The number of frequency points parameter determines how many frequency or wavelength steps are used for a simulation. It is expected that increasing the number of frequency points will results in absorption plots that are more smooth. In Fig. D.3 there is no visible difference between the plots, although there are some small differences in the IQEs. In the case of s-polarization as shown in Fig. D.4 there are some small areas above 650 nm where the plot consisting of 60 points differs, while the IQE again varies slightly. The number of frequency points did not end with complete convergence, but it was chosen to run with 100 frequency points as the IQE only varied a little when increasing the number of frequency points.

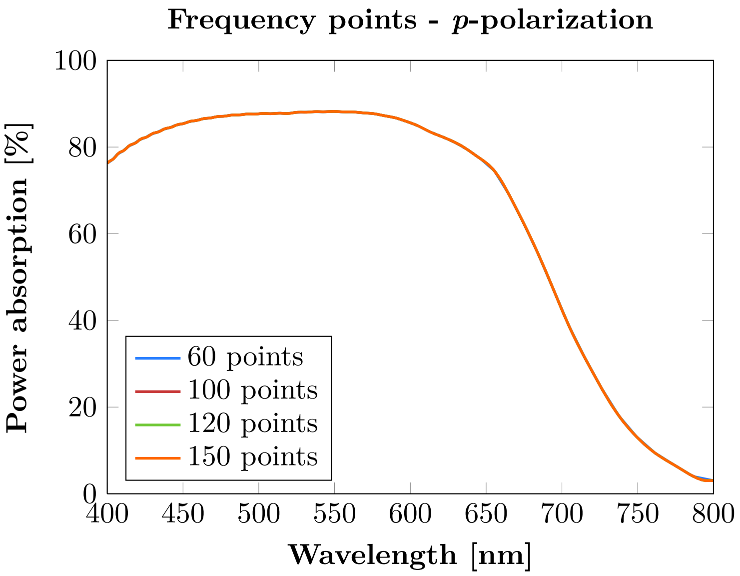

# points	IQE
60	0.6475
100	0.6369
120	0.6353
150	0.6357

Figure D.3. Absorption in Si with respect to wavelength for p-polarized light with varying number of frequency points and the corresponding IQE. The plots are on top of each other.

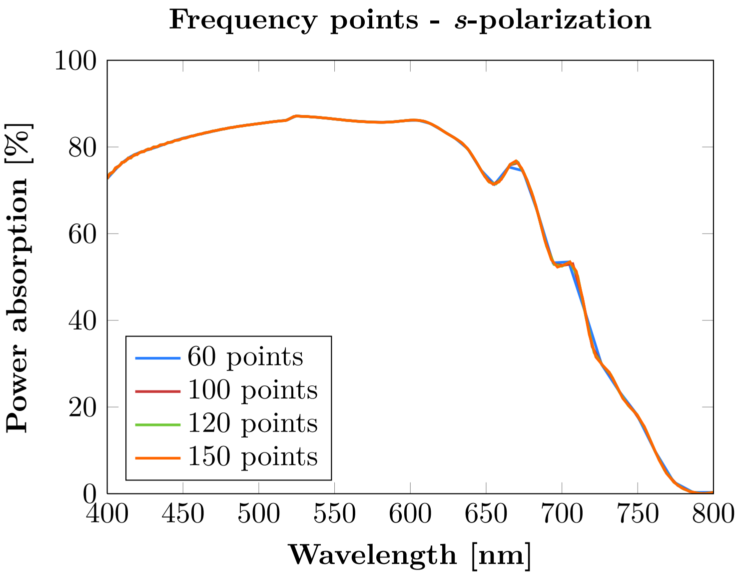

# points	IQE
60	0.6566
100	0.6459
120	0.6444
150	0.6447

Figure D.4. Absorption in Si with respect to wavelength for s-polarized light with varying number of frequency points and the corresponding IQE.

Figs D.5 and D.6 show the effect of changing the auto shutoff min. The auto shutoff min describes a fraction of the initial energy emitted by the source[51]. The simulation ends when the energy remaining in the simulation cell drops below this fraction. It is seen that the simulations converge when the auto shutoff min decreases. The simulations where set to run with the auto shutoff min set to $1 \cdot 10^{-5}$.

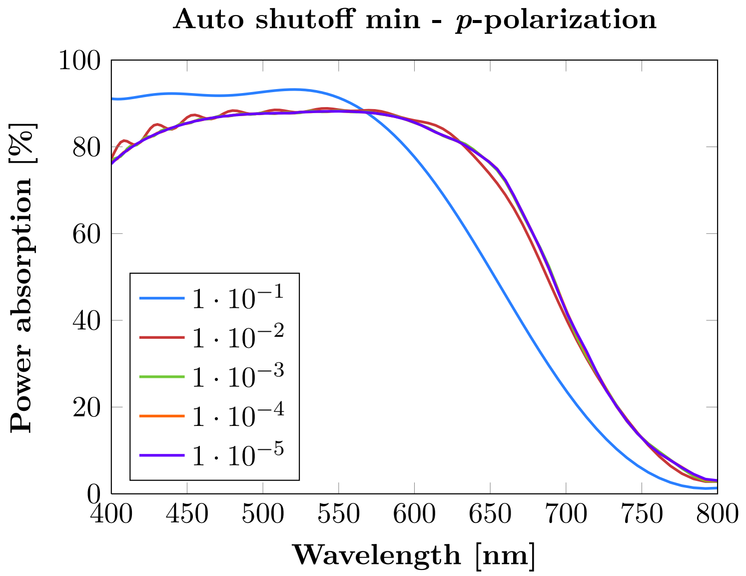

Auto shutoff min	**IQE**
$1 \cdot 10^{-1}$	0.5761
$1 \cdot 10^{-2}$	0.6339
$1 \cdot 10^{-3}$	0.6367
$1 \cdot 10^{-4}$	0.6369
$1 \cdot 10^{-5}$	0.6370

Figure D.5. Absorption in Si with respect to wavelength for *p*-polarized light with varying auto shutoff min and the corresponding IQE.

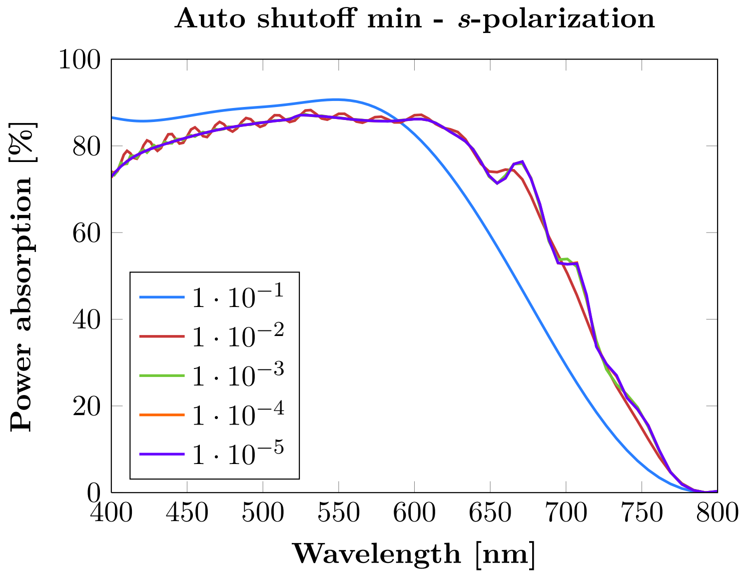

Auto shutoff min	**IQE**
$1 \cdot 10^{-1}$	0.5890
$1 \cdot 10^{-2}$	0.6418
$1 \cdot 10^{-3}$	0.6457
$1 \cdot 10^{-4}$	0.6459
$1 \cdot 10^{-5}$	0.6459

Figure D.6. Absorption in Si with respect to wavelength for *s*-polarized light with varying auto shutoff min and the corresponding IQE.

The influence of the min mesh step is shown in Figs. D.7 and D.8. The min mesh size controls the minimum mesh size for the mesh in the simulation region[51]. Increasing the min mesh step to 5 nm is seen to influence the results, while the result has converged for a min mesh step of 2 nm or below. The min mesh step was set to 2 nm.

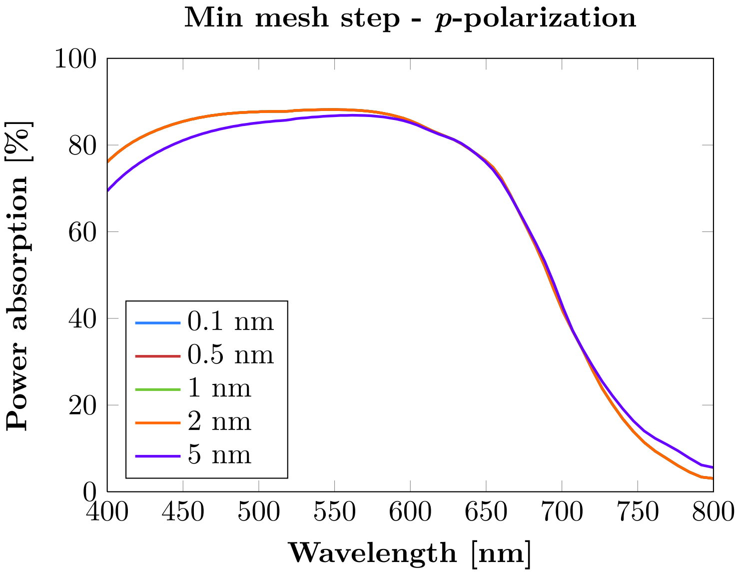

Min mesh step	IQE
0.1 nm	0.6370
0.5 nm	0.6370
1 nm	0.6370
2 nm	0.6370
5 nm	0.6310

Figure D.7. Absorption in Si with respect to wavelength for *p*-polarized light with varying min mesh step and the corresponding IQE. The plots for 0.1, 0.5, 1, and 2 nm are on top of each other.

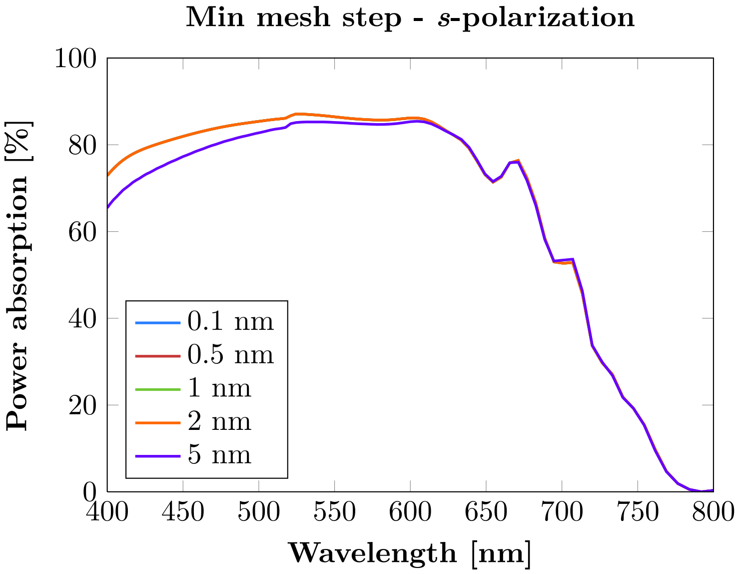

Min mesh step	IQE
0.1 nm	0.6459
0.5 nm	0.6459
1 nm	0.6459
2 nm	0.6459
5 nm	0.6330

Figure D.8. Absorption in Si with respect to wavelength for *s*-polarized light with varying min mesh step and the corresponding IQE. The plots for 0.1, 0.5, 1, and 2 nm are on top of each other.

Figs D.9 and D.10 show how the power absorption and IQE for Si varies with the number of PML layers. The number of PML layers determines how many cells are used for PML boundary conditions and influences how much light is reflected back into the simulation region at PML boundaries. It is seen that the results do not change when increasing the number of PML layers and the number of PML layers was thus set to 12.

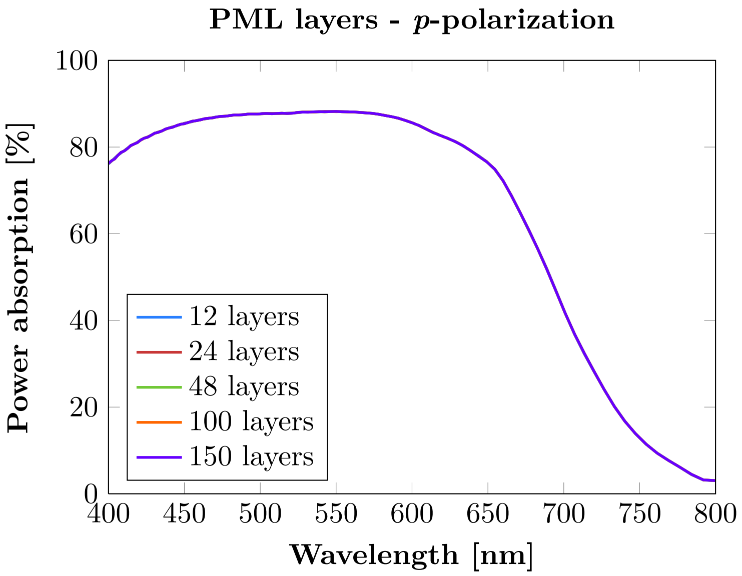
PML layers - *p*-polarization

# PML layers	IQE
12	0.6369
24	0.6369
48	0.6369
100	0.6369
150	0.6369

Figure D.9. Absorption in Si with respect to wavelength for *p*-polarized light with varying number of PML layers and the corresponding IQE. The plots are all on top of each other.

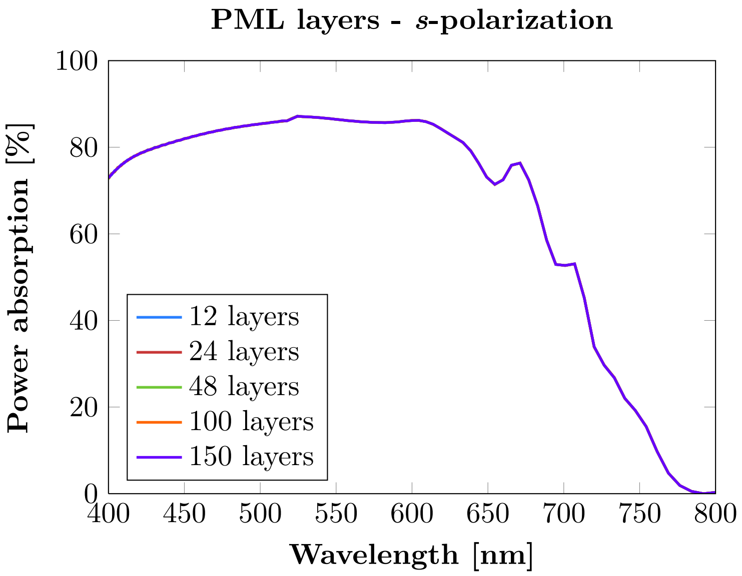
PML layers - *s*-polarization

# PML layers	IQE
12	0.6459
24	0.6459
48	0.6459
100	0.6459
150	0.6459

Figure D.10. Absorption in Si with respect to wavelength for *s*-polarized light with varying number of PML layers and the corresponding IQE. The plots are all on top of each other.

The source position and source width describes how close the source can be positioned to the structure surface and how wide the source must be. The source width must be at least the same width as the period of the structure L, while it makes no difference whether the source is positioned 100 nm or 10 μm away from the surface. The simulations were carried out with the source 500 nm away from the surface and with a source width corresponding to $2L$. The Al thickness corresponds to $h1$ in Fig. 4.1. Changing the Al thickness from 50–1000 nm did not change the results. The simulations were carried out with an Al thickness of 100 nm.

It was tested whether it made any difference to exchange the bottom PML boundary with a reflecting metal boundary, as there is only a neglible transmission through the aluminum back

surface. There was no difference in the results when exchanging the PML boundary for a metal boundary, but as there was neither any change in the simulation time, the simulations were carried out with a PML boundary as the bottom boundary.
The dt stability factor affects the size of the time step that is used for the simulation. It is a number between zero and one, where the simulation time decreases with a larger dt stability factor[51]. Changing the dt stability factor between 0.8 and 1 does not affect the results. The dt stability factor was set at 0.99 initially and was kept at this value. The different parameters for the convergence testing and the chosen settings are summarized in Tab. D.2.

Parameter	**Setting**
Mesh accuracy	8
Frequency points	100
Auto shutoff min	$1{\cdot}10^{-5}$
Min mesh step	2 nm
PML layers	12
Source position	500 nm
Source width	$2L$
Al thickness	100 nm
Bottom boundary	PML
dt stability factor	0.99

Table D.2. Settings used for simulations of triangular structures after convergence testing.

D.2 Anodized structures

The simulations for the anodized structures were supposed to be started with the same parameters as shown in Tab. D.2. Simulating the optical properties of the anodized structures compared to the triangular structures does however cause a change from a 2D simulation cell to a 3D simulation cell. This change means that the size of the simulation cell increases significantly, which means that much more memory is required to run the simulations. Due to the amount of memory available for running the simulations and in order to decrease simulation time, the simulations for the anodized structures had to be carried out with a lower mesh accuracy compared to the triangular structures.

Fig. D.11 shows how the power absorption and the IQE varies for different mesh accuracies for a PA surface with 60 nm ITO, 300 nm Si and 100 nm Al. It is seen that the changes follow what was seen in Figs. D.1 and D.2 for the triangular structure. Even though the results did not converge, it was chosen to run simulations with mesh accuracy 3. This means that the simulated IQE for the anodized will be lower if directly compared to the IQE of the triangular structures, as there is less light absorbed at the lower wavelengths were the solar intensity is highest. The results should however still be valid for indicating which ITO thickness is optimum for the anodized structures. Changing the number of frequency points from 100 to 60 points induces small changes in the power absorption above 650 nm as shown in Fig. D.12. It was chosen to run simulations with 60 frequency points as it greatly reduced the memory requirements for running the simulations.

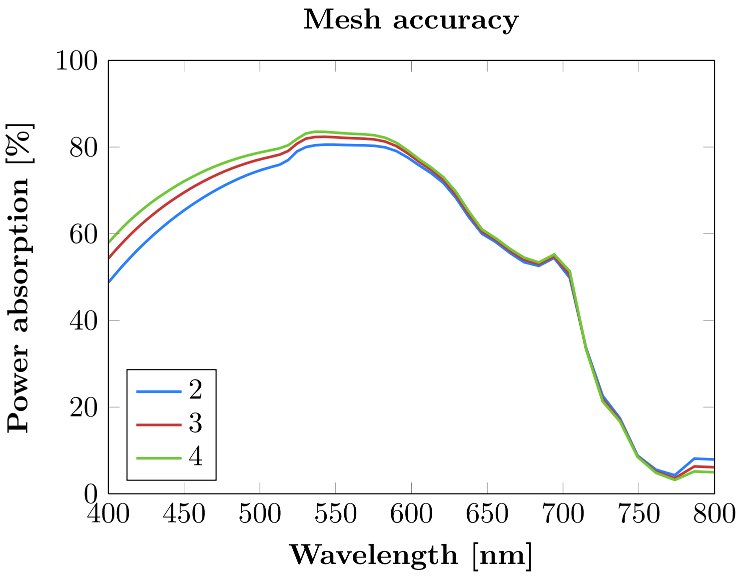

Mesh accuracy	IQE
2	0.5618
3	0.5744
4	0.5827

Figure D.11. Absorption in Si with respect to wavelength for varying mesh accuracy and the corresponding IQE.

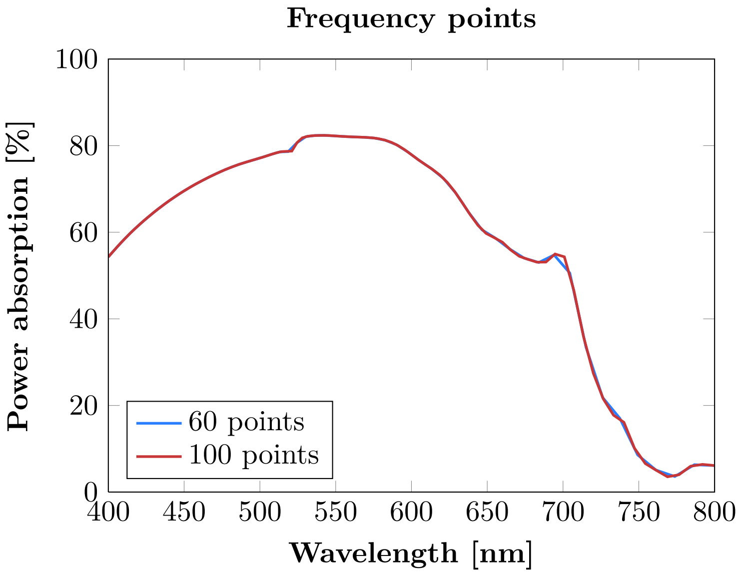

# points	IQE
60	0.5744
100	0.5640

Figure D.12. Absorption in Si with respect to wavelength for varying number of frequency points and the corresponding IQE.

Other parameters as the source position, min mesh step, Al thickness, and bottom boundary were also tested. The simulations of the triangular structures were rather quick and the simulation time did not change significantly when varying parameters such as Al thickness and the bottom boundary. As the simulations of the anodized structures are more time consuming, some of these parameters have been changed in order to save time as they now do have a notable influence on the simulation time. The parameters used for running the simulations of the anodized structures are summarized in Tab. D.3.

Parameter	**Setting**
Mesh accuracy	3
Frequency points	60
Auto shutoff min	$1\cdot 10^{-5}$
Min mesh step	2 nm
PML layers	12
Source position	100 nm
Source width	$2L$
Al thickness	100 nm
Bottom boundary	Metal
dt stability factor	1

Table D.3. Settings used for simulations of anodized structures after convergence testing.

The effect of using mesh accuracy 3 instead of mesh accuracy 8 is shown in Figs. D.13 and D.14. In Fig. D.13 it is seen that the IQE for PA imprints with varying ITO thickness, 300 nm Si and Al is lower when using mesh accuracy 2 compared to using mesh accuracy 3. The curvature of the plots is however the same, which indicates that decreasing the mesh accuracy mainly leads to a decrease in IQE while still showing the correct tendencies for the IQE. Fig. D.14 shows the IQE for triangular structures with varying ITO thickness and lattice period for two different mesh settings. It is again seen that the IQE decreases when using a lower mesh accuracy, but it still shows the same results considering how the IQE depends on ITO thickness and lattice period.

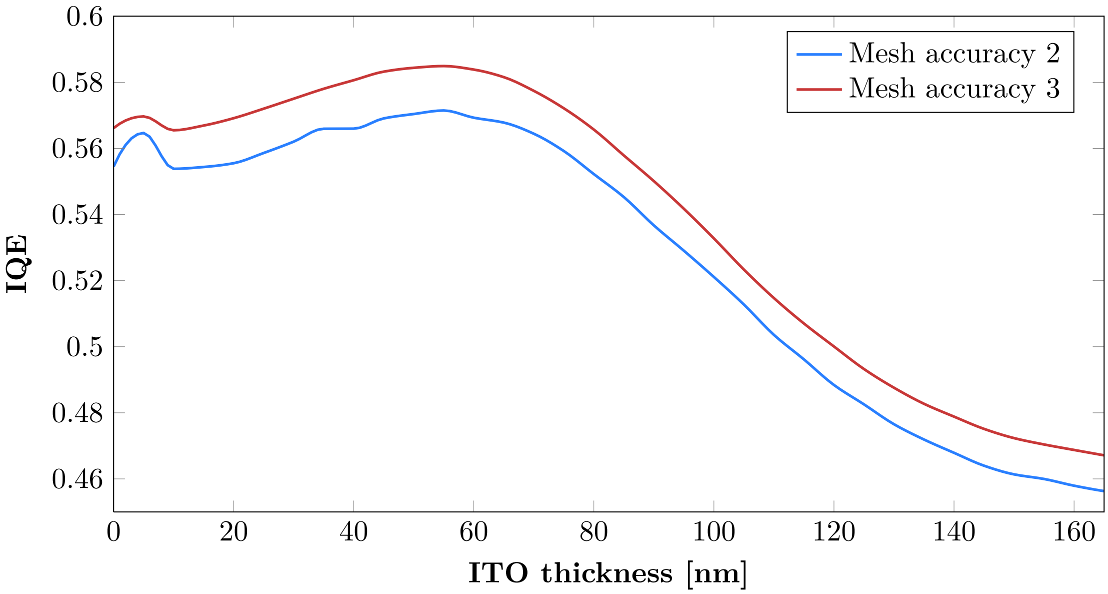

Figure D.13. IQE for PA imprints with varying ITO thickness, 300 nm Si and Al when using different mesh accuracy settings.

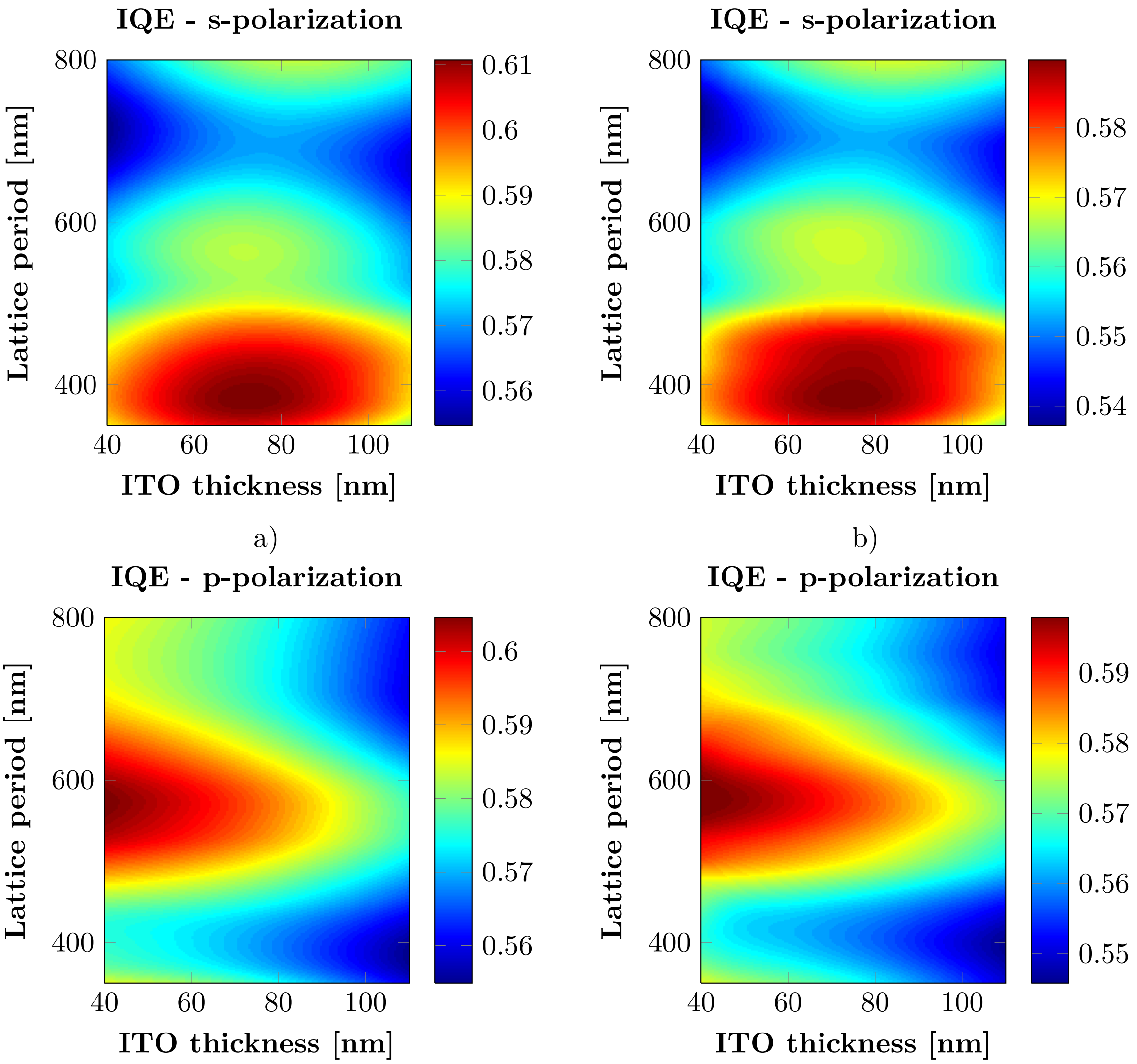

a) b)

c) d)

Figure D.14. IQE for triangular structure with 300 nm period and a plateau width of 50 nm. Simulations were carried out with mesh accuracy a+c) 8 and b+d) 3.

Chapter E

Refractive indices

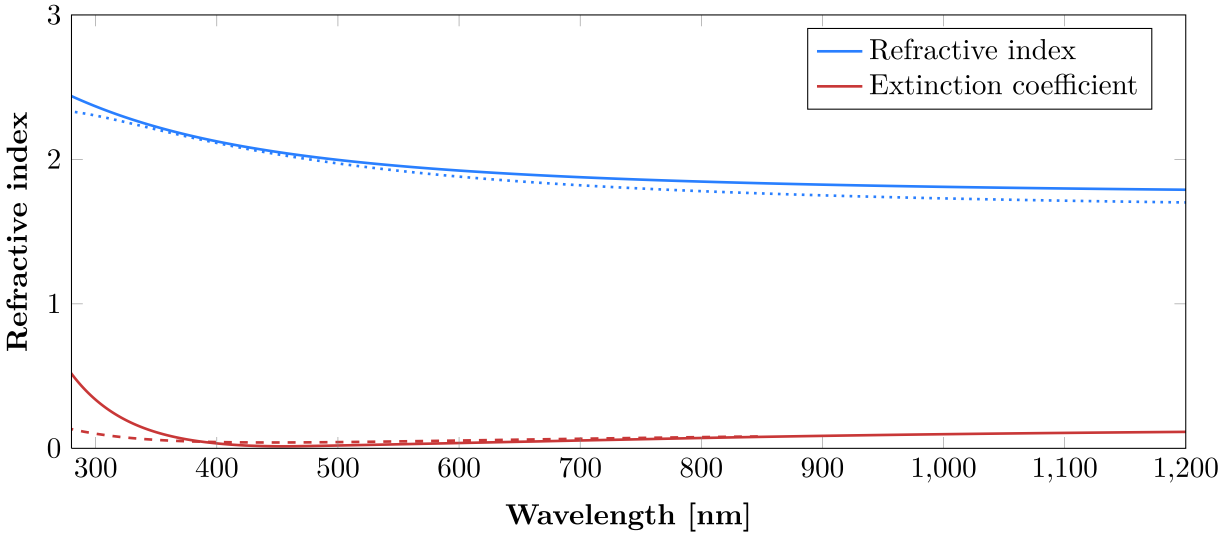

Figure E.1. Refractive index of ITO. Solid lines represent the experimentally determined refractive index that was used for simulations, while the dashed lines are data taken from Sopra[20] for comparison. The data from Sopra only covers wavelengths up to 850 nm.

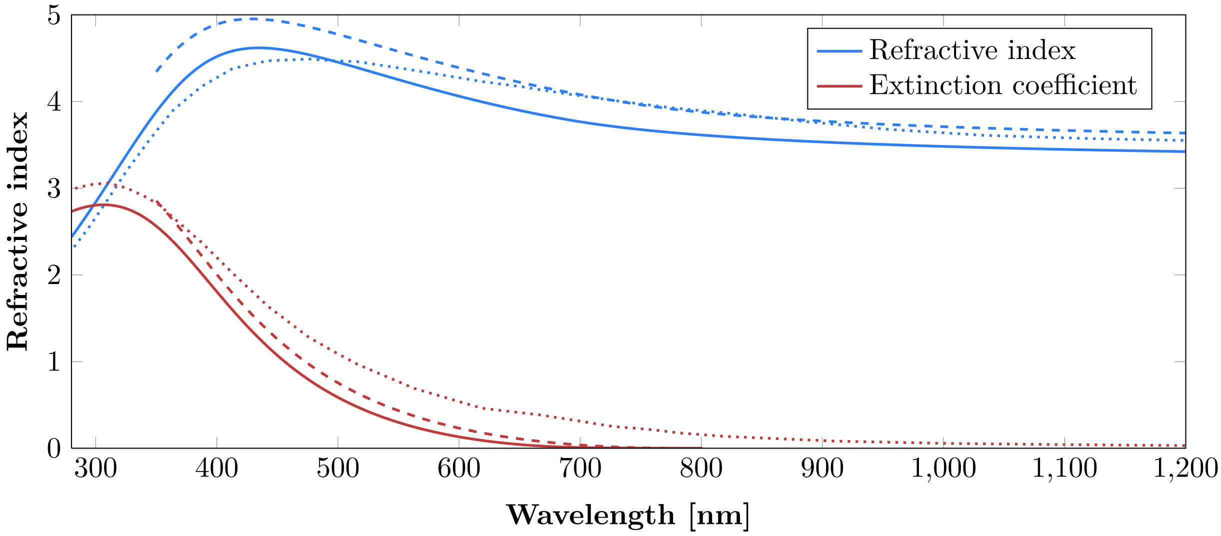

Figure E.2. Refractive index of a-Si. Solid lines represent the experimentally determined refractive index. The dashed lines show the refractive index used for convergence testing, which was experimentally determined in an earlier project[14]. The dotted lines are data taken from Palik[32] for comparison.

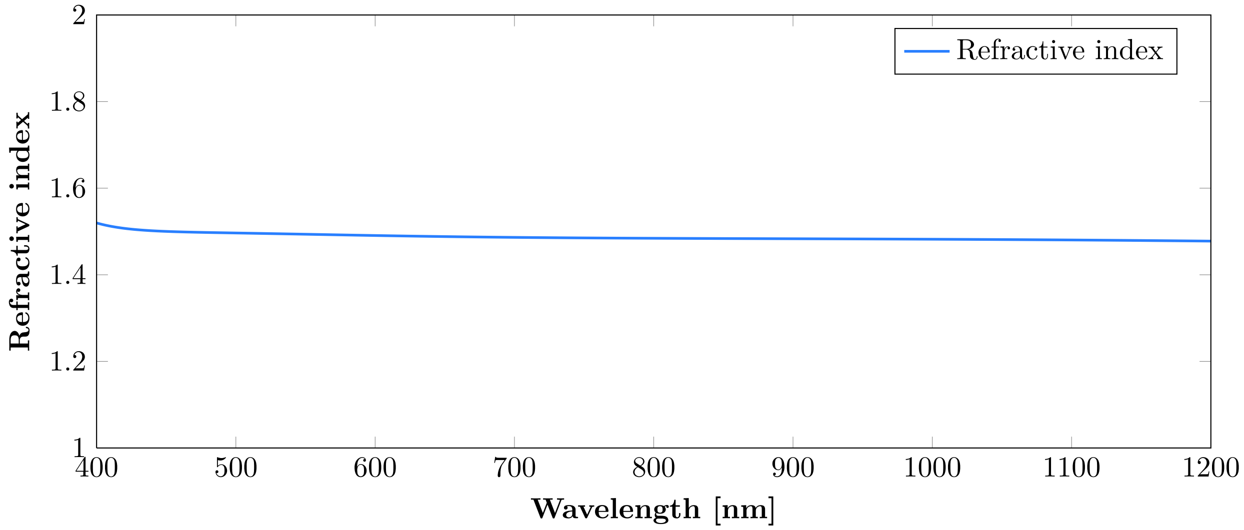

Figure E.3. Refractive index of PMMA taken from Kasarova et al.[31]

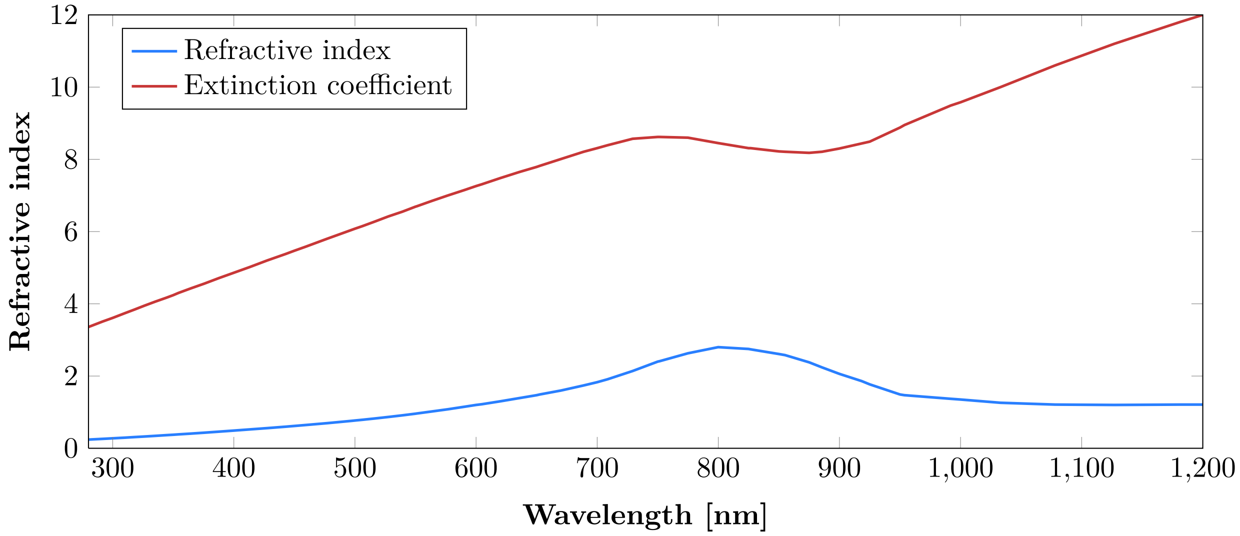

Figure E.4. Refractive index of Al taken from Palik[32].

References

[1] A. Jäger-Waldau (2012), *PV status report 2012*, Publications Office of the European Union, ISBN: 9789279260735.

[2] BP p.l.c. (2012), *BP statistical review of world energy June 2012*, `http://bp.com/statisticalreview`, downloaded: 11/23-2012.

[3] M. A. Green, K. Emery, Y. Hishikawa, W. Warta and E. D. Dunlop (2012), *Solar cell efficiency tables (version 40)*, Prog. Photovolt: Res. Appl. **20** (5), 606–614.

[4] J. Zhu, Z. Yu, S. Fan and Y. Cui (2010), *Nanostructured photon management for high performance solar cells*, Mater. Sci. Eng. R, **70** (3-6), 330–40.

[5] P. Spinelli, V. E. Ferry, J. van de Groep, M. van Lare, M. A. Verschuuren, R. E. I. Schropp, H. A. Atwater and A. Polman (2012), *Plasmonic light trapping in thin-film Si solar cells*, J. Opt. **12** (2), 024002.

[6] S. J. Brun, M. R. Thomsen and P. R. Whelan (2011), *Microstructured surfaces as an alternative to antireflective coatings for photovoltaic applications*, Bachelor thesis, Department of Physics and Nanotechnology, Aalborg University,

[7] A. V. Shah, H. Schade, M. Vanecek, J. Meier, E. Vallat-Sauvain, N. Wyrsch, U. Kroll, C. Droz and J. Bailat (2004), *Thin-film silicon solar cell technology*, Prog. Photovolt: Res. Appl. **12**, 113–42.

[8] K. L. Chopra, P. D. Paulson and V. Dutta (2004), *Thin-film solar cells: An overview*, Prog. Photovolt: Res. Appl, **12** (2-3), 69–92.

[9] American Society for Testing and Materials (2002), *Reference solar spectral irradiance: air mass 1.5*, `http://rredc.nrel.gov/solar/spectra/am1.5`, downloaded: 05/02-2011.

[10] H. L. Chen, S. Y. Chuang, C. H. Lin and Y. H. Lin (2007), *Using colloidal lithography to fabricate and optimize sub-wavelength pyramidal and honeycomb structures in solar cells*, Optics Express, **15** (22), 14793–803.

[11] H. A. Atwater and A. Polman (2010), *Plasmonics for improved photovoltaic devices*, Nature Materials, **9** (3), 205–13.

[12] V. E. Ferry, M. A. Verschuuren, H. B. T. Li, E. Verhagen, R. J. Walters, R. E. I. Schropp, H. A. Atwater and A. Polman (2010), *Light trapping in ultrathin plasmonic solar cells*, Optics Express, **18** (S2), A237–45.

[13] Y.-C. Tsao, T. Søndergaard, E. Skovsen, L. Gurevich, K. Pedersen and T. G. Pedersen (2013), *Pore size dependence of diffuse light scattering from anodized aluminum solar cell backside reflectors*, Optics Express, **21** (S1), A84–95.

[14] S. J. Brun, M. Gastaldo, M. R. Thomsen and P. R. Whelan (2011), *Microstructured solar cell substrates*, Semester project, Department of Physics and Nanotechnology, Aalborg University,

[15] C. Battaglia, J. Escarré, K. Söderström, M. Boccard and C. Ballif (2012), *Experimental evaluation of the light trapping potential of optical nanostructures for thin-film silicon solar cells*, Energy Procedia, **15**, 206–11.

[16] J. Escarré, K. Söderström, M. Despeisse, S. Nicolay, C. Battaglia, G. Bugnon, L. Ding, F. Meillaud, F.-J. Haug and C. Ballif (2012), *Geometric light trapping for high efficiency thin film silicon solar cells*, Solar Energy Materials & Solar Cells, **98**, 185–90.

[17] C. A. Mills, J. G. Fernandez, A. Errachid and J. Samitier (2008), *The use of high glass temperature polymers in the production of transparent, structured surfaces using nanoimprint lithography*, Microelectronic engineering, **85** (9), 1897–1901.

[18] D.-H. Kim, M.-R. Park and G.-H. Lee (2006), *Preparation of high quality ITO films on a plastic substrate using RF magnetron sputtering*, Surface & Coatings Technology, **201** (3), 927–31.

[19] T. Gorjanc, D. Leong, C. Py and D. Roth (2002), *Room temperature deposition of ITO using r.f. magnetron sputtering*, Thin Solid Films, **413** (1), 181–5.

[20] Sopra SA (2013), *Sopra n and k database - ITO*, `http://refractiveindex.info/`, downloaded: 04/02-2013.

[21] G. C. Schwartz and V. Platter (1975), *An anodic process for forming planar interconnection metallization for multilevel LSI*, J. Electrochem. Soc. **122** (11), 1508–16.

[22] Z. He, M. Zheng, M. Hao, T. Zhou, L. Ma and W. Shen (2011), *Evolution process of orderly nanoporous alumina by constant high field anodization in oxalic acid electrolyte*, Applied Physics A, **104** (1), 89–94.

[23] A. P. Li, F. Müller, A. Birner, K. Nielsch and U. Gösele (1998), *Hexagonal pore arrays with a 50-420 nm interpore distance formed by self-organization in anodic alumina*, Journal of Applied Physics, **84** (11), 6023–6.

[24] S. A. Campbell (2008), *Fabrication engineering at the micro- and nanoscale*, 3rd ed., Oxford University Press, ISBN: 9780195320176.

[25] F. A. Jenkins and H. E. White, eds. (1976), *Fundamentals of Optics*, 4th ed., Mcgraw-Hill College, ISBN: 9780070323308.

[26] J. Bartella, J. Schroeder and K. Witting (2001), *Characterization of ITO- and TiO_xN_y films by spectroscopic ellipsometry, spectraphotometry and XPS*, Applied Surface Science, **179** (1-4), 181–90.

[27] G. E. Jellison, Jr. and F. A. Modine (1996), *Parameterization of the optical functions of amorphous materials in the interband region*, Appl. Phys. Lett. **69** (3), 371–3.

[28] L. J. van der Pauw (1958), *A method of measuring specific resistivity and Hall effect of discs of arbitrary shape*, Philips Res. Repts. **13** (1), 1–9.

[29] T. J. Ypma (1995), *Historical development of the Newton-Raphson method*, SIAM, **37** (4), 531–51.

[30] G. E. Jellison, Jr. and F. A. Modine (1996), *Erratum: "Parameterization of the optical functions of amorphous materials in the interband region"*, Appl. Phys. Lett. **69** (14), 2137.

[31] S. N. Kasarova, N. G. Sultanova, C. D. Ivanov and I. D. Nikolov (2007), *Analysis of the dispersion of optical plastic materials*, Optical materials, **29** (11), 1481–90.

[32] E. D. Palik, ed. (1998), *Handbook of optical constants of solids*, vol. 1, Academic Press, ISBN: 9780125444200.

[33] C. Fisker and T. G. Pedersen (2013), *Opimization of imprintable nanostructured a-Si solar cells: FDTD study*, Optics express, **21** (102), A208–20.

[34] Lumerical Solutions, Inc. (2013), *FDTD Solutions Knowledge Base*, `http://docs.lumerical.com/en/fdtd/user_guide_absorption_2.html`, downloaded: 31/05-2013.

[35] I. Horcas, R. Fernandez, J. Gomez-Rodriguez, J. Colchero, J. Gomez-Herrero and A. M. Baro (2007), *WSXM: A software for scanning probe microscopy and a tool for nanotechnology*, Rev. Sci. Instrum. **78** (1), 013705.

[36] M. V. Klein and T. E. Furtak, eds. (1986), *Optics*, 2nd ed., Wiley, ISBN: 9780471872979.

[37] M. H. Lee, N. Lim, D. J. Ruebusch, A. Jamshidi, R. Kapadia, R. Lee, T. J. Seok, K. Takei, K. Y. Cho, Z. Fan et al. (2011), *Roll-to-roll anodization and etching of aluminum foils for high-throughput surface nanotexturing*, Nano Letters, **11** (8), 3425–30.

[38] S. Li, X. Qiao and J. Chen (2006), *Effects of oxygen flow on the properties of indium tin oxide films*, Materials Chemistry and Physics, **98** (1), 144–7.

[39] S. D’Elia, N. Scaramuzza, F. Ciuchi, C. Versace, G. Strangi and R. Bartolino (2009), *Ellipsometry investigation of the effects of annealing temperature on the optical properties of indium tin oxide thin films studied by Drude–Lorentz model*, Applied Surface Science, **255** (16), 7203–11.

[40] B. Rech, T. Roschek, J. Müller, S. Wieder and H. Wagner (2001), *Amorphous and microcrystalline silicon solar cells prepared at high deposition rates using RF (13.56MHz) plasma excitation frequencies*, Solar Energy Materials & Solar Cells, **66** (1), 267–73.

[41] A. S. Ferlauto, R. J. Koval, C. R. Wronski and R. W. Collins (2002), *Extended phase diagrams for guiding plasma-enhanced chemical vapor deposition of silicon thin films for photovoltaics applications*, Applied Physics Letters, **80** (15), 2666–8.

[42] G. Liu and S. J. Fonash (1989), *Selective area crystallization of amorphous silicon films by low-temperature rapid thermal annealing*, Applied Physics Letters, **55** (7), 660–2.

[43] Y. Nasuno, M. Kondo and A. Matsuda (2002), *Microcrystalline silicon thin-film solar cells prepared at low temperature using PECVD*, Solar Energy Materials & Solar Cells, **74** (1), 497–503.

[44] Y. Y. Ong, B. T. Chen, F. E. Tay and C. Iliescu (2006), *Process analysis and optimization on PECVD amorphous silicon on glass substrate*, Journal of Physics: Conference Series, **34** (1), 812–7.

[45] TOPAS Advanced Polymers (2013), *TOPAS product brochure*, `http://www.topas.com/sites/default/files/files/topas_product-brochure_english.pdf`, downloaded: 06/06-2013.

[46] DuPont (2013), *DuPont Teflon films for photovoltaic modules*, `http://www2.dupont.com/Teflon_Industrial/en_US/assets/downloads/k15778.pdf`, downloaded: 06/06-2013.

[47] R J Chase Company, Inc. (2013), *FEP handbook*, `http://www.rjchase.com/fep_handbook.pdf`, downloaded: 06/06-2013.

[48] O. Tuna, Y. Selamet, G. Aygun and L. Ozyuzer (2010), *High quality ITO thin films grown by dc and RF sputtering without oxygen*, J. Phys. D: Appl. Phys. **43** (5), 055402.

[49] M. Bender, J. Trube and J. Stollenwerk (1999), *Deposition of transparent and conducting indium-tin-oxide films by the r.f.-superimposed DC sputtering technology*, Thin Solid Films, **354** (1), 100–5.

[50] F. Wooten, ed. (1972), *Optical properties of solids*, Academic Press, ISBN: 9780127634500.

[51] Lumerical Solutions, Inc. (2013), *FDTD Solutions Knowledge Base – Absorption per unit volume*, `http://docs.lumerical.com/en/fdtd/knowledge_base.html`, downloaded: 12/05-2013.